Modelling of wall-bounded flows near a cylinder-bed junction in turbulent flow conditions using an IDDES turbulence model to asses initial particle entrainment

L. J. Bierhuizen

Delft University of Technology

In consultation with

Deltares

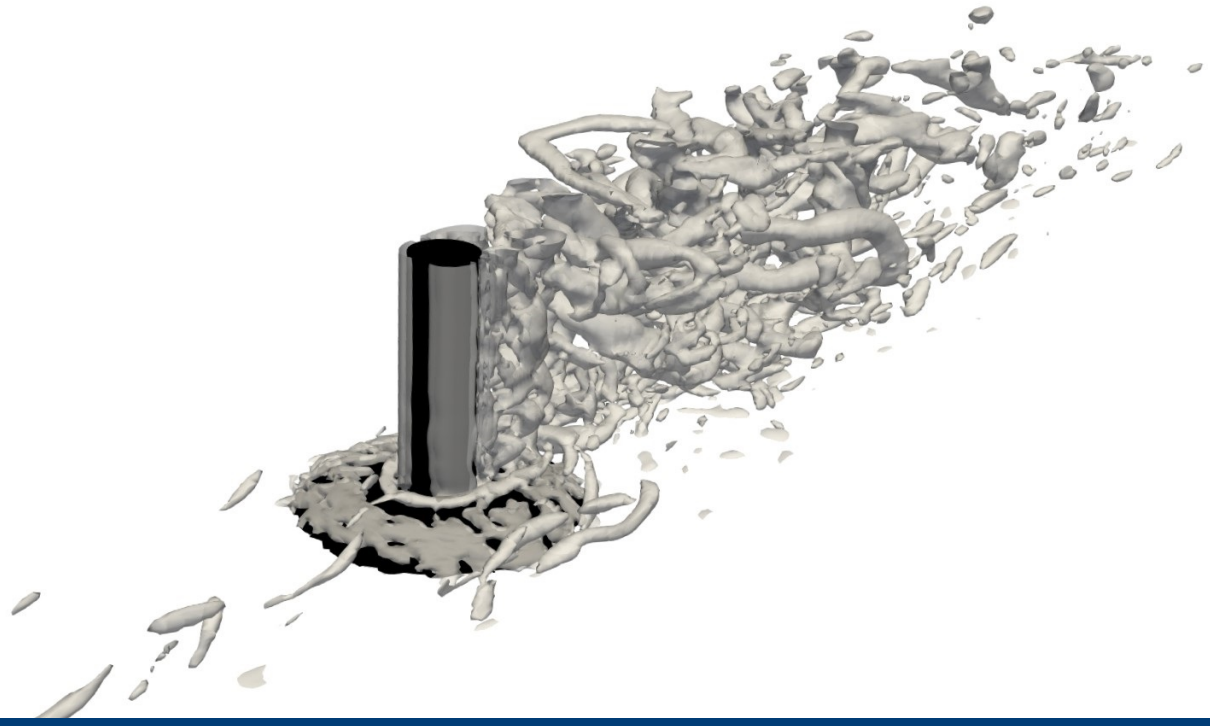

TU Delft

Modelling of wall-bounded flows near a cylinder-bed junction in turbulent flow conditions using an IDDES turbulence model to asses initial particle entrainment

by

L. J. Bierhuizen

in partial fulfilment of the requirements for the degree of

Master of Science
in Offshore & Dredging Engineering,

at the Delft University of Technology,
to be defended publicly on Friday 24 April 2020 at 11:00.

Student number:	4388623	
Project duration:	February 4, 2019 – April 24, 2020	
Thesis committee:	Prof. dr. ir. A. V. Metrikine,	TU Delft
	Ir. T. C. Raaijmakers,	TU Delft
	Dr. Ir. T. O'Mahoney,	Deltares
	Ir. N. Bruinsma	Deltares

An electronic version of this thesis is available at `http://repository.tudelft.nl/`.

TU Delft

Deltares
Enabling Delta Life

Preface

The presented work concludes the master program of Offshore & Dredging Engineering at the Technical University of Delft. The study had been performed in collaboration with the research institute Deltares at the Harbour, Coastal and Offshore Engineering department.

At the start of my internship at Deltares, I was offered to accompany numerous experiments at the Easter Scheldt Flume in the Hydro Hall of Deltares. I would like to take this opportunity to thank Gosse Oldenziel, with whom I had a great pleasure working with, for his supervision during this period. Additionally, I would like to thank each of the committee members for their guidance during the project. I would like to express my gratitude towards Niek Bruinsma, Tom O'Mahoney and Tim Raaijmakers for sharing their knowledge and for continuously providing relevant input for this work. I have found the in-depth discussions throughout the study immensely interesting and helpful. Without doubt, the standard of this thesis has substantially risen due to the contributions of the committee members.

L. J. Bierhuizen
Delft, April 2020

Abstract

Due to the presence of a monopile in a turbulent flow a negative pressure gradient can form upstream of the cylinder that redirects the flow downwards towards the cylinder-bed junction. At the bottom of the cylinder the boundary layers separates from the bed so that a swirling vortex, known as a horseshoe vortex (HSV), forms which then travels downstream of the cylinder as it is being dragged along with the current. The horseshoe vortices can scoop up bed material surrounding the cylinder, weakening the foundation of the structure by reducing the embedded length of the pile. This phenomenon is known as scour. Different scour protection methods have been suggested to prevent the occurrence of scour or significantly reduce its effects. A common protection method is the dumping of stones in the vicinity of the cylinder-bed junction so that the flow dynamics near the bed are altered in such a way that the underlying sediment is mostly unaffected. However, the protection material itself is also subject to hydrodynamic forcing and can therefore be entrained as well. This would be described as damage to the protection layer as its effectiveness reduces due to re-exposure of the underlying sediment. It is for this reason that protection layers have to be carefully designed depending on their use. The mechanism of the horseshoe vortex system and its damaging aspects are not completely understood yet, making engineering of specific protection layers challenging.

To better understand the flow behaviour upstream of a cylinder-bed junction, where the formation of the horseshoe vortices takes place, several tests have been performed at the Eastern Scheldt Flume in the Hydro Hall of Deltares. Here different cylinder and bed protection configurations were subjected to turbulent current and wave conditions and the upstream flow fields were measured with a particle image velocimetry (PIV) measurement system. Since the obtained information of the tests is limited to a specific area, there was an interest in modelling the test cases by means computation fluid dynamics (CFD), while using the test results as validation.

In this thesis several of the test cases have been modelled in OpenFOAM with the Improved Delayed Detached Eddy Simulation (IDDES) hybrid turbulence model, based on the Spalart-Allmaras formulation, which include the following:

a) An open channel with a smooth bed and no monopile

b) An open channel with a rough bed and no monopile

c) An open channel with a smooth bed and a smooth monopile

d) An open channel with a rough bed and a smooth monopile

The modelling strategy used starts off with a basic simulation case (a) which is compared to the test results for validation of the simulated flow characteristics. This model is then elaborated on by inclusion of either a rough protection model (b) or a smooth cylinder (c). Both models are again validated with the test results so that the ability of the IDDES model to simulate the fluid-structure interaction is investigated. Finally, a simulation that includes both a rough bed and a smooth cylinder (d) is performed. For simulation cases b), c) and d) an assessment is made for potential initial particle entrainment by means of hydrodynamic forcing indicators. Based on the stability criteria of Hofland [18] and Shields [45] a new formulation is presented that attempts to accounts for the limited grid resolution of IDDES-based simulations that make use of wall functions. In this study the indicator fields are analysed and, when possible, compared to test cases. No fitting of the stability formula has been performed in this study due to absence of concrete particle entrainment values and is suggested for future work.

The thesis also includes an investigation towards the use of wall functions for modelling the mentioned test cases and the ability of the model to predict comparable flow behaviour. It was found that the use of of wall functions is accommodated with an inherent roughness, which is referred to as numerical roughness during the thesis. The issue is claimed to originate in an inaccurate wall shear stress estimation, which then affects the simulated boundary layer of the flow near the bed. Knowledge of the occurrence of numerical roughness is deemed important when modelling near-bed flow phenomena using wall functions.

Contents

Nomenclature

Symbol		
a	acceleration	$[\mathrm{m\,s^{-2}}]$
A	projection area	$[\mathrm{m^2}]$
C	Courant number	
C_s	roughness constant	
C_D	drag coefficient	
C_L	lift coefficient	
C_p	pressure coefficient	
d_w	wall distance	[m]
d_s	grain diameter	[m]
D	characteristic length scale	[m]
D	derivative	
f	vortex shedding frequency	[Hz]
F	force	$[\mathrm{kg\,m\,s^{-2}}]$
g	gravitational acceleration	$[\mathrm{m\,s^{-2}}]$
k	turbulent kinematic energy	$[\mathrm{m^2\,s^{-2}}]$
K_s	roughness height	[m]
K_s+	dimensionless roughness height	
p	pressure	$[\mathrm{kg\,m^{-1}\,s^{-2}}]$
Re	Reynolds number	
S_{ij}	strain rate	$[\mathrm{s^{-1}}]$
S_r	Strouhal number	
t	time	[s]
u	velocity	$[\mathrm{m\,s^{-1}}]$
u_τ	friction velocity	$[\mathrm{m\,s^{-1}}]$
$U+$	dimensionless velocity	
$y+$	dimensionless wall-normal distance	
δ	Kronecker delta	
δ	boundary layer thickness	
Δ	grid spacing	[m]
κ	von Kármán constant	
μ	dynamic viscosity	$[\mathrm{kg\,m^{-1}\,s^{-1}}]$
ν	kinematic viscosity	$[\mathrm{m^2\,s^{-1}}]$
$\tilde{\nu}$	modified turbulent eddy viscosity	$[\mathrm{m^2\,s^{-1}}]$
ν_t	turbulent kinematic viscosity	$[\mathrm{m^2\,s^{-1}}]$
ρ	density	$[\mathrm{kg\,m^{-1}}]$
τ_w	wall shear stress	$[\mathrm{kg\,m^{-1}\,s^{-2}}]$
Ψ	stability criterion	
ω	rotation rate	$[\mathrm{rad\,s^{-1}}]$

Math symbol	
μ / $\overline{\ }$	mean
σ	standard deviation
$'$	fluctuation
∇	Laplacian
δ	partial derivative
$\tilde{\ }$	projection onto bed via Pythagorean equation

Abbreviations	
CFD	Computational fluid dynamics
CFL	Courant-Friedrichs-Lewy condition
DES	Detached eddy simulation
DDES	Delayed detached eddy simulation
DNS	Direct numerical simulation
GIS	Grid induced separation
HSV	Horseshoe vortex
IDDES	Improved delayed detached eddy simulation
LES	Large edd simulation
LLM	Log-layer mismatch
MSD	Modelled stress depletion
PIV	Particle image velocimetry
RANS	Reynolds averaged Navier-Stokes
S-A	Spalart Allmaras
TKE	Turbulent kinetic energy
WMLES	Wall-modelled largy eddy simulation

1 Introduction

1.1. Background

An interesting fluid-structure mechanism can occur due to the interaction between waves and currents and a seabed-monopile junction. This mechanism is the formation of a *horseshoe vortex* structure (HSV) upstream of a monopile, but it can also be observed around other structures such as bridge-piers or the legs of an offshore platforms. The HSV is formed by a difference in stagnation pressures in front of the monopile, which is the result of a depth-dependent velocity profile of an incoming boundary flow. The downward pressure gradient causes a rotation of the incoming flow due to separation of the boundary layer and forms a swirling vortex around the monopile as is travels downstream, see Figure 1.1. In case of an erodible bed, the horseshoe vortices can scoop out material at the foundation of the monopile, a phenomenon known as scour, which weakens the stability of the foundation. Scour introduces a long term risk to structures as the effective embedded length will decrease over time to a certain extend. For this reason numerous efforts have been made to better understand the mechanism behind scour and HSV systems.

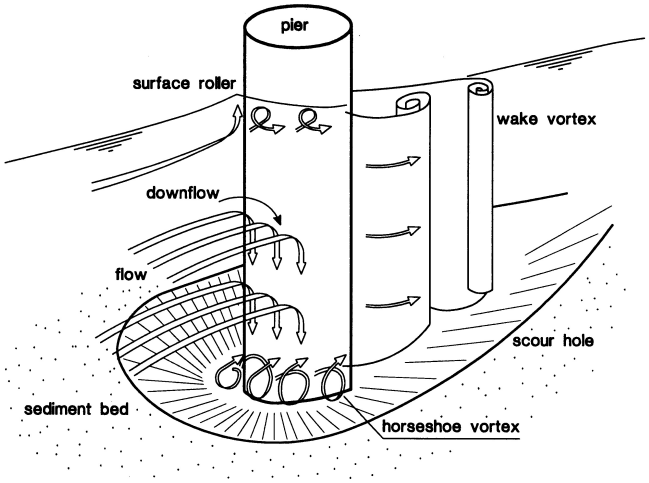

Figure 1.1: Flow mechanism and scour around a pier, adopted from Zhou [56]

For example, the numerical results found in Roulund et al. [42] show that the size of the HSV and the corresponding bed shear stress increase with increasing boundary-layers-thickness-to-pile-diameter, δ/D, until a certain maximum value. For very small values of δ/D no HSV exist at all. Also the influence of the Reynolds number Re_d based on the cylinder diameter (see Equation 2.1) is discussed. It is stated that the size of the HSV and the corresponding bed shear stress increase with increasing Re_d in the laminar regime, but the opposite is true in the turbulent regime. The influence of the bed roughness on the horseshoe vortex was found to be insignificant.

Ozturk et al. [33] conducted Particle Image Velocimetry (PIV) measurements of a flow past a circular cylinder on a flat plane for different intervals of $Re_d = 750$ to $Re_d = 9600$. The results show that for increasing

Reynolds number, the domain of the HSV decreases, that its center shifts towards the junction region and that the strength increases due to an increase in momentum of the incoming turbulent flow.

Both the results of Praisner and Smith [37] and Ozturk et al. [33] as well as those of Sahin et al. [44] show that multiple horseshoe vortices can form upstream of the monopile as well as stagnation points, otherwise called saddle points. In those papers the largest vortex is called the primary vortex, but is not necessarily the closest vortex to the monopile. For example, Praisner and Smith [37] show the presence a small corner vortex near the bed-monopile junction. It is possible for a counter-rotational vortex to exist in between two co-rotational vortices. Ozturk et al. [33] mention that since these counter-rotational vortices are not continuously fed by the surface fluid, they expand in size and loose strength until they are swept away by the surrounding flow.

The presence of a HSV was found beneficial or some applications as it is shown to increase the local heat transfer rates by up to 300% [37], a concept which for example is used in fin-and-tube heat exchangers [47].

The bimodal behaviour of HSV is discussed in Paik et al. [34] and D. Anderson and Lynch [10]. Here a concept is investigated which suggests that the mean velocity beneath the primary HSV has two quasi-stabe modes; the zero-flow and back-flow modes. This can be analyzed in a distribution histogram of the streamwise velocity component, which shows two distinct peaks. The first peak is associated with a strong jet-like stream that travels upstream and corresponds to a negative velocity, i.e. the back-flow mode. The second peak is associated with the break down of the jet, after which the recirculating fluid contributes to the primary HSV.

1.2. Problem definition

In practise the occurrence of a horseshoe vortex system around obstacles in waters can result in scour that weakens the stability of the structure foundation. The HSV is formed upstream of these obstacles and is of interest for further investigation. Experiments were performed in the Hydro Hall of Deltares to gain more insight in the flow patterns upstream of a cylinder and to check the influence of the pile roughness and bed protection foundations on the upstream flow patterns. The experiments guided the formulation of this research project as numerical studies can provide additional information of the flow field surrounding the cylinder-bed junction.

Over the last decade the computational power of computers have risen to such extends that they can sufficiently be used for numerical approaches to solving fluid flows, a study called *Computational Fluid Dynamics* (CFD). Numerical methods can provide a cost effective approach to investigating fluid flows at full scale as the real world physics are being simulated. However, there is a lack of standardization in the field of CFD which is expressed in Georgiadis et al. [15]. In this article the proper usage of one of the numerical models, the Large-Eddy Simulation (LES), is questioned and it states that there is probably a misuse of the method in a large number of simulation found in papers. This emphasizes the relevance of convergence studies of the numerical simulations and their validation procedure to ensure the reliability of the results. This leads to the question whether it is possible to accurately simulate the complex flow patterns upstream of an obstacle and the corresponding turbulent features for reasonable computational costs. These aspects are relevant because it allows for a better understanding of the failure mechanisms of the scour protection layers themselves.

1.3. Objective and research questions

This proposal is aimed at contributing to the existing studies by assessing the ability of the Improved Delayed Detached Eddy Simulation (IDDES) modelling technique to accurately capture the upstream flow behaviour of a cylinder-bed junction. This will be attempted by means of a numerical study that analyses the near-bed flow characteristics and the effects of bed surface roughness. The numerical results are validated by means of experiment measurements and literature results. Ultimately, the capabilities of the IDDES model to predict hydrodynamic force indicators on the bed are reviewed in relation to the prediction of particles entrainment. Based on this description the following objective is formulated:

The objective of this research is to evaluate the applicability of the IDDES hybrid modelling technique for simulating a cylinder-bed junction in an open channel so to asses its ability to predict particle entrainment due to turbulent flow conditions.

To accomplish this objective several research questions are formulated to help guide the process. The accommodating research questions are as follows:

- Which numerical modelling approach is most appropriate in simulating turbulent flows near a cylinder-bed junction region related to the entrainment of sediment?
- How to properly account for the surface roughness in the numerical model and how well is the assumed near wall boundary profile approximated?
- What is the accuracy of the numerically obtained flow patterns and associated statistics of entrainment-indicating parameters on the bed?
- How does the inclusion of a bed protection layer alter the hydrodynamic load conditions on the bed and to what extend is the numerical model able to predict its inclusion regarding the hydrodynamic forcing on the bed?

1.4. Methodology

The general approach that will be followed comprises of four parts that are interconnected:

- **Experiment phase**

  To start off, assistance was provided during tests in the Hydro Hall of Deltares. This would prove beneficial as it presented a visual interpretation of the experiments and its procedure so that a better understanding is obtained of the flow mechanics and test difficulties.

- **Literature study**

  During the research the literature study acts as a theoretical basis and a reference framework throughout the graduation project. At the start the basics of turbulence are reviewed so that the essence of turbulence modelling is better understood. After consideration of different turbulent modelling approaches a final turbulence model is chosen based on the time frame of the graduation project. The application of this model is further investigated with the use of literature study. Additionally, research towards particle displacement is vital for assessment of the numerical results.

- **Numerical simulation strategy**

  Prior to the main numerical study a preliminary study is performed with different RANS models to evaluate the general applicability of wall function. Then the most interesting experiment cases will be chosen for the objective of the thesis and a numerical strategy is formed to asses the numerical models. A numerical basis will be formed by only considering a open channel case. This model is then built upon by inclusion of different model extensions. This part consists of elaborate numerical studies that requires a solid theoretical/practical foundation, resulting from the previous two parts, to perform. The following numerical models are considered:

  – An open channel
  – An open channel including a smooth cylinder
  – An open channel including a rough protection bed
  – An open channel including both a smooth cylinder and a rough protection bed

- **Results validation and interpretation**

  The results of each of numerical will be compared to the results of the practical study. Additionally, an attempt will be made to validate the study by comparison with results from literature studies as well. A new stability formula is presented for simulation cases with limited grid resolution that makes use of load indicator parameter. Each of the bed load parameters is individually investigated and, if possible, compared to test entrainment patterns. In the end an assessment is made of the IDDES model regarding the performed simulations and its ability to predict particle entrainment region.

1.5. Outline Thesis

First, a literature study is presented in Chapter 2 that discusses the fundamentals of turbulence and numerical approaches. Additionally, a study of sediment entrainment is presented and at the end the performed experiments are reviewed. In Chapter 3, a description of the numerical strategy is given and an overview of

the numerical models are provided. The obtained results are presented in Chapter 4. A number of considerations are discussed in Chapter 5. Then a concluding overview is given in Chapter 6 in which the research questions and overall objective are reviewed. And finally, a segment dedicated to recommendations for future studies is given in Chapter 7.

2

Literature study

In 1883, Osborne Reynolds [39] performed an experimental investigation where he injected highly coloured water into a tube that contained propagating clear water to visualize the flow patterns. At low flow velocities the coloured water propagated along in a straight line, indicating steady behaviour of the flow which is known as a *laminar* flow. Throughout the experiments the velocity of the clear water was increased by small increments and this eventually caused the flow patterns to show intermittent bursts of chaotic flow, indicative of a transition regime of the water flow. By further increasing the flow velocity a continuous chaotic behaviour was observed, which is defined as a fully *turbulent* flow. Reynolds [40] later showed that these different flow regimes could be characterized by a dimensionless quantity, known as the Reynolds number:

$$Re = \frac{uD}{\nu} \tag{2.1}$$

Here u is the fluid velocity [$\mathrm{m\,s^{-1}}$], D is the characteristic length scale [m] and ν is the kinematic viscosity [$\mathrm{m^2\,s^{-1}}$].

The Reynolds number represents the ratio of the inertial forces to the viscous forces, which in practise is an important design parameter. For example, turbulent shedding on a golf ball is purposely induced to reduce its drag coefficient. Of these regimes, it is the turbulent flow that occurs dominantly in nature. This is also the regime that was observed during the performed experiments in which the flow field upstream of numerous configurations was visualized (Section 2.6.1). It is for this reason that the turbulent regime is elaborated on in this thesis.

In the sections to come the phenomenon of turbulence is first further discussed to establish a basic understanding of turbulence. Following up, the numerical modelling technique for turbulent flows is reviewed as well as additional numerical aspects that are relevant for the simulation of channel flow. Then information about the entrainment of sediment is provided. This is used to interpret the obtained numerical results and to asses the accuracy of the numerical model regarding entrainment. In the final section an overview is given of the experiments, of which the results are used for validation of the numerical cases.

2.1. Turbulence

Turbulence is a phenomenon that can be observed on a daily basis, such as the smoke rising from a sigaret, unsteady water flow from a tap or the sudden movements of objects that are being carried by the wind. From these examples it is clear that some disordered movement of a given medium is involved in turbulence. The exact details of turbulence are not yet well understood and an exact definition of turbulent is not established. There are, however, a number of characteristic features that are generally agreed upon, such as [11, 43]:

- **High Reynolds numbers**. This feature specifies that the flow is inertia dominated, resulting in instabilities within the flow field.
- **Irregularity**. The flow variables in turbulence are random and chaotic, resulting in a very disordered motion of the flow.
- **Three-dimensionality**. There is interaction of the vorticity fluctuations in all three space dimensions, which explains that turbulent phenomena are strictly three-dimensional.

- **Diffusivity**. This feature describes the spreading of the velocity fluctuations of the turbulent flow, which grows over time after separation has occurred. This enhances the rate of exchange of momentum and so induces stronger mixing of the flow.
- **Dissipation**. Turbulent flow is subject to continuous energy dissipation as a result of viscous damping at the smallest vortex structures.
- **Broad length and time spectrum**. Turbulence is associated with a large range of length and time scales that are excited in the form of vortex structures. The size as well as the turn-over time of the vortex can differ significantly between different vortices in turbulent flow.

As listed, turbulent phenomena are associated with high Reynolds numbers. There is no specific Reynolds number at which a flow becomes fully turbulent as this is case specific. For instance, the critical Reynolds number at which a flow starts transitioning from laminar to turbulent behaviour is different for pipe flow than it is for flow around geometries, such as plates and cylinders [54]. A high Reynolds number specifies, according to the definition of the Reynolds number, that inertial forces are dominant over the viscous forces. Viscosity can be interpreted as a damping mechanism that causes perturbations in the flow to subside. When this mechanism is overshadowed by inertial effects, the perturbations tend to grow instead in a random manner. This explains why turbulent phenomena are characteristically chaotic over time and inherently unsteady. Turbulent behaviour is also defined as non-deterministic due to the randomness that is involved in the realization of the turbulent phenomena. This characteristic makes it difficult to predict the flow in advance as in practise the deterministic Navier-Stokes equations are used to solve for the flow field. [30, 32, 36, 43]

2.1.1. Deterministic chaos

In this section it is illustrated that chaotic behaviour can be generated from a deterministic model, like the Navier-Stokes equations. The term *chaos* indicates that the behaviour of a system is aperiodic, very sensitive to initial conditions and independent of other processes both in space and time. Most systems in nature contain chaotic behaviour, implying that certain individual processes of these systems show random behaviour. But as a whole the they are in fact bound by orderly laws and thus not entirely chaotic. The term that is used to describe the behaviour of these phenomena is *deterministic chaos*. This concept was discovered in 1963 by Edward lorenz [26] who had simplified the development of convection flow of the atmosphere to only three differential equations, now known as the Lorenz equations:

$$\begin{aligned} \frac{dx}{dt} &= \sigma(y-x) \\ \frac{dy}{dt} &= x(\rho-z)-y \\ \frac{dz}{dt} &= xy-\beta z \end{aligned} \tag{2.2}$$

Here σ, ρ and β are system parameters and x, y and z are state variables. Such a system of equations is known as a toy model due to the simplification of very complex system that aims to investigate basic properties of that system. In this case the equations capture the evolution of a convective atmosphere that is heated from the bottom and cooled from the top. For a specific set of system parameters of $\sigma = 10$, $\rho = 28$ and $\beta = 8/3$ that are representative of atmospheric conditions, an arbitrary duration of the solution to the Lorenz system is shown in Figure 2.1. The curves do not converge to a final state condition, known as a limit state, nor to a periodic condition, known as a limit cycle. The resulting curve is actually non-converging and changes its rotation randomly around so-called *strange attractors* after a limited amount of time. This concept shows how seemingly random behaviour is obtained from a deterministic model. If stable, two very important observations can be made regarding this system:

- The resulting curve is limited in terms of its state variables. When initial conditions outside this variable space region are chosen the curve will converge to the limited variable space region. Its behaviour within this region is, as discussed, non-converging.
- Extremely small differences in initial conditions will lead to vastly different results over a sufficiently long time, which is one of the characteristics of chaos. Due to the visual representation of the solution to the Lorenz system looking like butterfly wings, this effect was called the *butterfly effect*. It is this effect that makes it very difficult to make any long-term predictions of natural phenomenon, and other processes with chaotic behaviour.

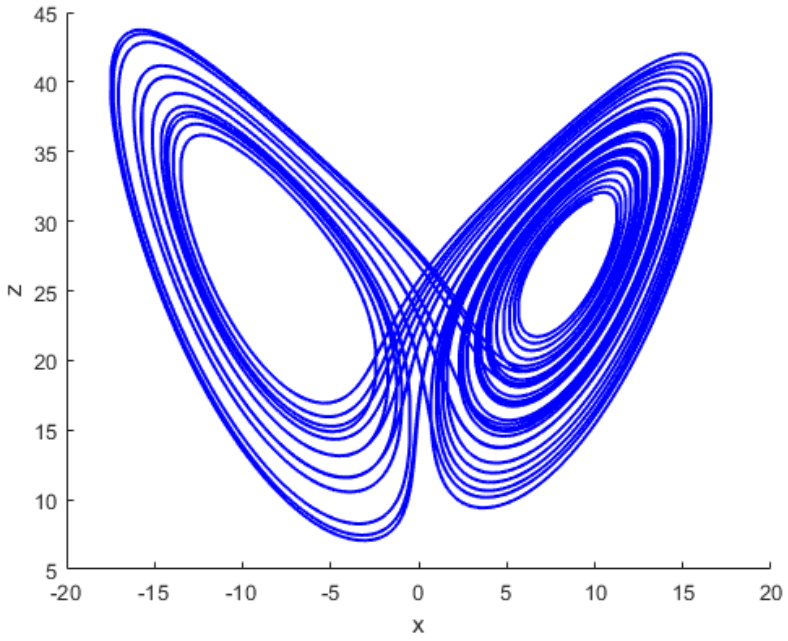

Figure 2.1: Sample solution to the Lorenz system of equations

2.1.2. Self-similarity of turbulence

To better understand how a deterministic model is used to describe chaotic flows, a fundamental principles of turbulence is discussed next that shows a degree of order in phenomena that are seemingly random. The mentioned fundamental principle is known as *self-similarity*, meaning that there is recurrence of a certain part of the geometry at different scales. It illustrates how complex, disordered geometries can be reconstructed by repeating only a certain simple, ordered part of the geometry. Its occurrence was discovered in 1975 by Mandelbrot [20] who published a book describing his observations of self-similarity in nature itself. In here numerous examples are provided, such as the branching of trees, arteries and rivers. The main structure of the geometry is replicated up to the smallest scales by continuous sub-branching. Geometries or phenomena that display self-similarity are referred to as *fractals*. Fractals defy the basic understanding of spatial dimensions of a given geometry as they are found to have dimensions with non-inter values. The self-similarity characteristic of turbulence is observed in the mechanism by which energy is transferred in turbulent flows. This mechanism is discussed in the next section.

2.1.3. Energy cascade

Even though turbulent phenomena are characterized by chaotic behaviour, it also exhibits more organized behaviour such as coherent vortex structures. This is also illustrated in Figure 2.2 where coherent eddy structures of different sizes can be seen. These structures contain a wide range of excited length and time scales, which all contribute to the principal concept of *energy cascade*. It tells us that the large scale eddies draw kinetic energy from velocity gradients in the mean flow. This energy is then transferred to smaller eddies by means of vortex stretching. Vortex stretching implies elongation of the eddy, so that its diameter reduces. Here the volume of the eddy remains constant due to incompressibility of the fluid. Now due to the conservation of angular momentum the angular velocity of the eddy will increase. As a result the kinetic energy of the large eddy has been transferred to a smaller one since now the radius of the eddy has decreased. This process continuous in a cascading manner to the small scale eddies where finally the energy is dissipated by viscosity. This turbulent energy dissipation is denoted as ϵ [$m^2\,s^{-3}$].

2.1.4. Kolmogorov Hypotheses

The Kolmogorov hypotheses [14, 21] consists of three hypothesis that helps us better understand the nature of the different turbulent scales and to perform a dimensionless analysis for the different time and length scales that contribute to a coherent turbulent structure.

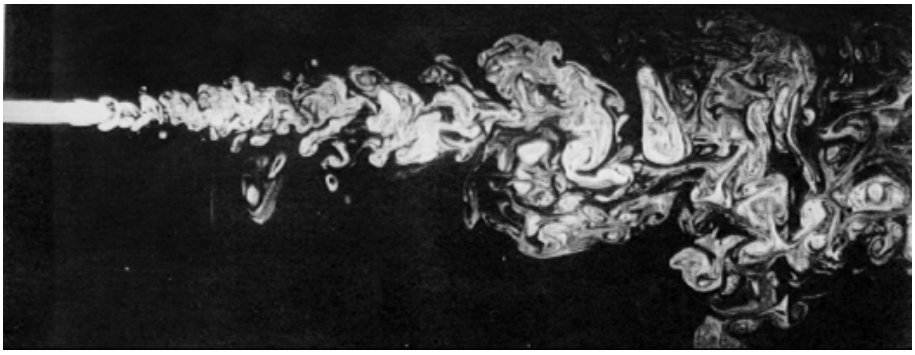

Figure 2.2: Flow transitioning from the laminar to the turbulent regime, adopted from [53]

The first one, *Kolomgorov's hypothesis of local isotropy*, states that at sufficiently high Reynolds number, the small-scale turbulent motions are statistically isotropic. This implies that directional information of the large scale eddies is lost during the energy cascade process, resulting in the small scale motions having a universal character. Therefore the small scales can be modelled in a more simple manner than the larger scales.

The second one, *Kolomgorov's first similarity hypothesis*, assumes that in every turbulent flow at sufficiently high Reynolds number, the statistics of the small-scale motions have a universal form that is uniquely determined by ν and the ϵ. Using this assumption the length, velocity and time scale parameters can be formed for the small scale motions by means of dimension analysis. These are also known as the Kolmogorov scales:

$$\eta = (\frac{\nu^3}{\epsilon})^{1/4} \tag{2.3}$$

$$u_\eta = (\nu\epsilon)^{1/4} \tag{2.4}$$

$$\tau_\eta = (\frac{\nu^3}{\epsilon})^{1/4} \tag{2.5}$$

It is important to note that these quantities have been formulated using $Re_\eta = \nu\eta/\nu \approx O(1)$. This is in agreement with the proposed principle of energy cascade where at small scales, corresponding to small Reynolds numbers, the kinetic energy is dissipated by viscous effects. Now from the above equations an expression for ϵ can be formed that depends only on small scale parameters. For large scales it can be shown the rate of energy production (per unit mass) scales as the following:

$$\Pi \approx \frac{u_0^2}{l_0/u_0} = \frac{u_0^3}{l_0} \tag{2.6}$$

The produced energy at the large scales is dissipated at the small scales in a dynamic balance, so that:

$$\Pi \approx \epsilon \tag{2.7}$$

And thus ϵ can be related to large scale parameters by eqs. (2.6) and (2.7) and small scale parameters by eqs. (2.3) to (2.5). By equating the expressions of epsilon for the small scales to the large scales the following dimensionless quantities are obtained as the ratio of smallest to largest scales of the length, velocity and time scale parameters:

$$\frac{\eta}{l_0} \propto Re^{-3/4} \tag{2.8}$$

$$\frac{u_\eta}{u_0} \propto Re^{-1/4} \tag{2.9}$$

$$\frac{\tau_\eta}{\tau_0} \propto Re^{-1/2} \tag{2.10}$$

This dependency on the Reynolds number shows that the expected range of scales excited in case of laminar and turbulent flows are different; The ratios decrease with increasing Reynolds number so that a greater range of turbulent scales will be contained in the flow.

The final hypothesis, *Kolmogorov's second similarity hypothesis*, assumes that in every turbulent flow at sufficiently high Reynolds number, the statistics of the motions of intermediate scales l ($l_0 \gg l \gg \eta$) have a universal form that is uniquely determined by ϵ, independent of ν. Here an intermediate range of scales is specified at which viscous effects are negligible and the energy cascade process is dominated by inertial forces. This intermediate range of scale is called the inertial subrange and will be elaborated on in the next section.

2.1.5. Energy spectrum

As of now the nature of small, intermediate and large scales have been discussed and the mechanism by which the energy is transferred. These ranges of turbulent scales are also associated with a certain energy distribution. This energy function $E(k)$ is given as a function of the wave number $k = 2\pi/l$ and can be seen in Figure 2.3. It should be noted that the value k is inversely proportional to the length scale l so that the large length-scale structures are depicted on the left side of the function. The figure shows that most energy is contained in the large structures and for this reason it is called the *Energy-containing range*. As discussed before, in this range turbulent kinetic energy is produced from gradients in the mean flow. At the right end of the spectrum the smallest eddies are depicted, which the least amount of energy. In this range the energy is dissipated due to viscosity and thus it is named the *dissipation range*. The final region, located in the middle of the spectrum, is called the *inertial subrange*. This range only exists for high Reynolds numbers and is not present for low Reynolds numbers as then the energy-containing range and dissipation range simply overlap. The inertial subrange can be considered the 'energy transport' region in the cascade process that transfers energy from large to successively smaller length scales as the motions in this subrange are determined by internal effects. An important feature of this subrange is that the slope corresponds to a decay proportional to $k^{-5/3}$, which is called the *Kolmogorov spectrum law*. This characteristic can be used in experiments or simulations to verify that the flow is indeed fully turbulent.

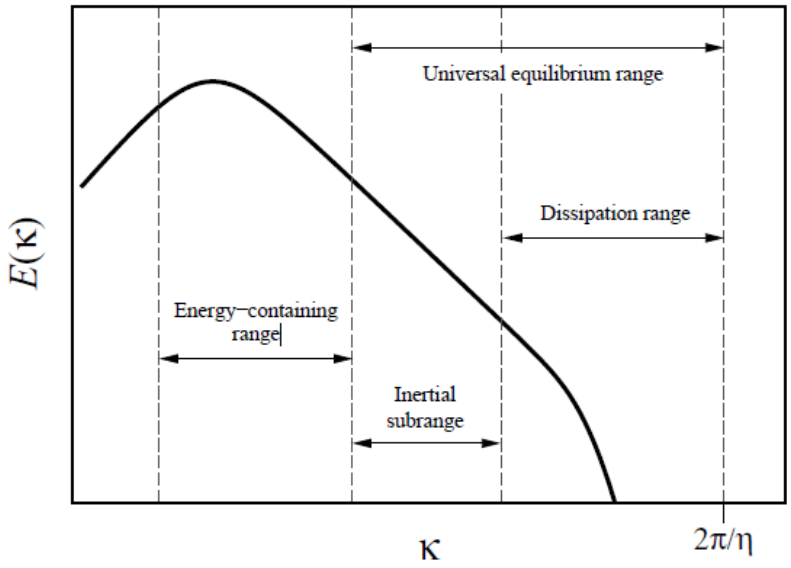

Figure 2.3: Model turbulent energy spectrum $E(\kappa)$, adopted from [30]

2.2. Turbulence modeling

Now that the basic properties of turbulence are discussed the method of modelling the fluid flow is presented. The next sections will provide a number of numerical methods that are formulated to numerically simulate fluid flow in both laminar and turbulent regimes. The governing equations for the motions of an incompress-

ible viscous fluid as a continuum are described by the Navier-Stokes equations and the continuity equation:

$$\frac{\delta \mathbf{u}}{\delta t} + \mathbf{u} \cdot \nabla \mathbf{u} = -\nabla p + \nu \nabla^2 \mathbf{u} \tag{2.11}$$

$$\nabla \cdot \mathbf{u} = 0 \tag{2.12}$$

Here ρ is the fluid density [kg m^{-3}], $\mathbf{u}$ is the fluid velocity [m s^{-1}] and p is the pressure [kg m^{-1} s^{-2}]. As of yet, analytical solutions can only be found for very simple problems with very simple boundary conditions (such as straight pipe flow) [54], but due to the complexity of turbulent flows numerical methods are used to solve the Navier-stokes equations. This study in general is called Computational Fluid Dynamics (CFD) and uses discretization methods to approximate the differential equations as a system of algebraic equations, which are solved numerically. The numerical tool used for this research is the open-source software OpenFOAM. This software makes used of finite volume discretization, based on conservation principles over small control volumes. A number of simulation approaches have been suggested, that will be considered next in terms of their applicability for the numerical simulations of the test cases.

2.2.1. Direct Numerical Simulation

The Direct Numerical Simulation (DNS) approach attempts to resolve every length and time scale in the flow by direct resolution of the numerical problem. This means that even the smallest scales have to be resolved and thus a sufficiently fine mesh by which the fluid domain is discretized has to be generated. Using the Kolomgorov scales it was shown that $\eta / l_0 \propto Re^{-3/4}$. Since in DNS all the scales are resolved, the smallest cell size Δx of the mesh should approximate the value of η. Therefore the number of grid points in each direction will be $N_x \approx l_0/\Delta x \propto Re^{3/4}$. Recalling that turbulence is a three-dimensional phenomenon, the required number of grid points can be approximated by $N_x^3 \approx (l_0/\Delta x)^3 \propto (Re^{3/4})^3$ [8]. For the number of time steps required, the mesh stability is considered by assuming a CFL number of 1 (see Section 2.4.1);

$$\frac{u_0 \Delta t}{\Delta x} = 1 \tag{2.13}$$

From this equation an expression for Δt can be formulated. This is then used to approximate the number of time iterations by $N_t \approx \tau_0/\Delta t \approx l_0/\Delta x \propto Re^{3/4}$, by considering that $\tau_0 \approx l_0/u_0$ as it represents the large scale turn-over time in the flow. The total cost is proportional to the number of grid points in the mesh and the number of time iterations due to mesh stability:

$$Cost \sim N_x^3 N_t \propto Re^3 \tag{2.14}$$

This shows that the numerical cost of DNS simulations grows strongly for increasing Reynolds numbers and is therefore only applicable to problems with low-to-moderate Reynolds numbers. If used correctly, DNS contains no empiricism and will generate accurate solutions for a given problem.

2.2.2. Reynolds averaging

The next family of models makes use of averaging of the Navier-stokes equations as was suggested by Osborne Reynolds. Hence it is assumed that the unsteady turbulent field can be split into a mean steady flow field and an unsteady turbulent field that is not resolved but modelled instead by steady-state correlations. In this model the statistical quantities themselves are decomposed into a mean component and a fluctuating component, which is referred to as the *Reynolds decomposition*.

$$U(x,t) = \overline{U}(x) + u'(x,t) \tag{2.15}$$

Averaging of this quantity will eliminate the fluctuating part and thus only the mean contribution will remain. When applying this decomposition to the fundamental Navier-Stokes equation, the *Reynolds Averaged Navier-Stokes* (RANS) equations are formed.

$$\begin{aligned} \frac{\delta \overline{\mathbf{u}}}{\delta t} + \overline{\mathbf{u}} \cdot \nabla \overline{\mathbf{u}} &= -\nabla p + \nu \nabla^2 \overline{\mathbf{u}} - \nabla \tau_{RANS}, \\ \nabla \cdot \overline{\mathbf{u}} &= 0 \end{aligned} \tag{2.16}$$

The RANS equation is identical to the original equation formulation, however now only the mean quantities are considered and an additional tensor τ_{RANS} is introduced. This term represents the transport of

momentum that affect the mean flow due to the fluctuations in the flow. It is also called the Reynolds stress tensor and, as it is symmetric and of second order, presents six additional unknowns to the set of equations. In total ten unknowns (three velocity components, the pressure and six stress components) are to be solved with four sets of equations (Navier-Stokes equations and continuity equation). This is known as the *closure problem*. To introduce closure additional mathematical models are to be formulated that inherently include approximations and empiricism. This results in the turbulent flow being modelled over the computational domain, in contrast to the DNS approach where it was resolved instead. In literature many sources have states that applicability of the RANS approach is limited in separated unsteady flows [3, 13, 41].

2.2.3. Large eddy simulation

Instead of time averaging, the Large Eddy Simulation (LES) method makes use of spatial averaging to separate the small scales from the large scales. This is achieved by a filtering operation by which the small scales are filtered out, remaining only with the large scales. These large scale structures will be resolved knowing that these scales contain most of the turbulent kinetic energy. As described before, Kolomgorov's hypothesis of local isotropy assumes that small-scale turbulent motions are statistically isotropic and therefore the filtered small scales will be modelled instead with universal behaviour. The spatial filtering operation is given by [43]:

$$\overline{f}(x,t) = G * f(x,t) = \int_0^\infty \int_\Omega G(\overline{\Delta}(x,t),x) - \zeta, t - t') f(\zeta, t') d\zeta dt' \tag{2.17}$$

Here $f(x,t)$ is any quantity of the flow in the flow domain, $\overline{f}(x,t)$ is the filtered variable output, Ω is the computational domain and G is a low-pass filter function in wave number space, which itself is a function of the filter width $\overline{\Delta}$. Different definitions exist for $\overline{\Delta}$, of which the most commonly one used in CDF packages is the cube-root of the cell volume [5]:

$$\overline{\Delta} = \sqrt[3]{\Delta_x \Delta_y \Delta_z} \tag{2.18}$$

Where Δ_x, Δ_y and Δ_z are the local grid step sizes in x, y and z directions [m], respectively. Application of the filtering operator G to the Navier-Stokes equations results in the *filtered Navier-stokes equations*:

$$\begin{aligned} \frac{\delta \overline{\mathbf{u}}}{\delta t} + \overline{\mathbf{u}} \cdot \nabla \overline{\mathbf{u}} &= -\nabla p + \nu \nabla^2 \overline{\mathbf{u}} - \nabla \tau_{SGS}, \\ \nabla \cdot \overline{\mathbf{u}} &= 0 \end{aligned} \tag{2.19}$$

This time the overbar represents a filtered quantity of the flow. Again a system that requires closure is obtained which contains unknown stress terms, collectively referred to as the sub-grid stress tensor τ_{SGS}:

$$\tau_{SGS} = \overline{\mathbf{u} \otimes \mathbf{u}} - \mathbf{u} \otimes \mathbf{u} \tag{2.20}$$

The term depicts the interaction between resolved and unresolved scales. To achieve closure multiple models have been formulated that use different empirical schemes to approximate the sub-grid stress tensor. One of the models was introduced in 1877 by Boussinesq which is based the turbulent viscosity hypothesis:

$$\tau_{SGS} = 2\nu_t S_{ij} - \frac{2}{3} k \delta_{ij}, \tag{2.21}$$

with

$$S_{ij} = \frac{1}{2}\left(\frac{\partial \overline{u_i}}{\partial x_j} + \frac{\partial \overline{u_j}}{\partial x_i}\right), \tag{2.22}$$

$$k = \frac{1}{2}\overline{u_i' u_i'}, \tag{2.23}$$

$$\delta_{ij} = \begin{cases} 1, & \text{if } i = j \\ 0, & \text{if } i \neq j \end{cases} \tag{2.24}$$

With S_{ij} being the mean strain rate [s^{-1}], ν_t the turbulent eddy viscosity [$m^2\,s^{-1}$], k the turbulent kinetic energy [$m^2\,s^{-2}$] and δ the Kronecker delta. The definition of ν_t to close to model is provided in the next section.

Rodi [41] mentions that ideally the *no-slip boundary condition* (see section 2.3.1) is used at the walls, which requires a very high resolution near the wall for high Reynolds number, to resolve the turbulent scales in the viscous sublayer. This is supported by others, such as Menter et al. [29] and Kumar et al. [22], of which the latter reports that LES computations near a wall is 1000 to 100000 times more costly than RANS computations. Piomelli [35] shows that the total cost of wall resolved LES is still considerable as it scales with $Re^{13/7}$. Because of the high cost of DNS and LES simulations a new type of model was proposed that significantly reduces the computational power required when simulating flows, while still being relatively accurate in modelling unsteady features of the flow. This type of model is known as a hybrid turbulence model, which is further discussed next.

2.2.4. Hybrid RANS-LES models

Hybrid models make use of both LES and RANS techniques and try to combine the advantages of both approaches. These models are designed as an alternative to the LES technique for massively separated flows with the desire to reduce the required simulation time. A number of different models have been formulated but in this thesis the IDDES (Improved Delayed Detached Eddy Simulation) model based on the Spalart-Allmaras formulation is adopted as is it one of the most used hybrid models for massive separations flows [4].

Spalart-Allmaras (S-A) turbulence closure model

Spalart Allmaras [48] devised a one-equation transport model, formulated with only one additional variable, the modified turbulent eddy viscosity $\tilde{\nu}$:

$$\tilde{\nu} = \frac{\nu_t}{f_{v1}}, \tag{2.25}$$

with

$$f_{v1} = \frac{\chi^3}{\chi^3 + c_{v1}^3}, \chi = \frac{\tilde{\nu}}{\nu}$$

where ν is the kinematic viscosity [$m^2\,s^{-1}$] and c_{v1} is an empirical constant. The governing transport equation for $\tilde{\nu}$ is given by

$$\frac{D\tilde{\nu}}{Dt} = c_{b1}\tilde{S}\tilde{\nu} + \frac{1}{c_\sigma}[\nabla\cdot((\nu+\tilde{\nu})\nabla\tilde{\nu} + c_{b2}(\nabla\tilde{\nu})^2] - c_{w1}f_w[\frac{\tilde{\nu}}{d}]^2, \tag{2.26}$$

with

$$\tilde{S} = \omega + \frac{\tilde{\nu}}{\kappa^2 d}f_{v2}, \tag{2.27}$$

$$f_{v2} = 1 - \frac{\chi}{1+\chi f_{v1}}, \tag{2.28}$$

$$f_w = g[\frac{1+c_{w3}^6}{g^6+c_{w3}^6}]^{1/6}, \tag{2.29}$$

$$g = r + c_{w2}(r^6 - r), \tag{2.30}$$

$$r = \frac{\tilde{\nu}}{\tilde{S}\kappa^2 d^2} \tag{2.31}$$

where ω is the curl of u [$rad\,s^{-1}$], κ is the von Kármán constant and d is the wall distance [m]. Additional constants are provided in Table 2.1.

Table 2.1: Constants according to the S-A turbulence model

$c_{b1} = 0.135$	$c_{b2} = 0.622$	$c_{w1} = \frac{c_{b1}}{\kappa^2} + \frac{1+c_{b2}}{c_\sigma}$	$c_{w2} = 0.3$
$c_{w3} = 2$	$c_{v1} = 7.1$	$c_\sigma = \frac{2}{3}$	$\kappa = 0.41$

Detached Eddy Simulation (DES)
The original hybrid model that was introduced in 1997 by Spalart et al. [49] is the DES (Detached Eddy Simulation) model. In this model the attached eddies, in the boundary layers, are modelled using the RANS method since the RANS method can model the near wall regions at low computational costs, in contrast to the LES method that requires a fine grid at these locations. The detached eddies, in separation regions, are modelled using the LES technique. The switch from LES to RANS is based on local flow characteristics, making this approach non-zonal as no arbitrary domain is specified for both methods. Strelets [52] mentions that this feature also suggests a single velocity and eddy viscosity field that is smooth in the transition region. The original formulation of the S-A model was altered to allow for a blending between the RANS and LES models. The wall distance parameter d was replaced with a new length scale l_{DES}, given as

$$l_{DES} = min[d_w, C_{DES}\Delta] \tag{2.32}$$

with $C_{DES} = 0.65$ being an empirical constant and Δ the largest local grid spacing according to the following definition:

$$\Delta = max[\Delta_x, \Delta_y, \Delta_z] \tag{2.33}$$

The connection between the RANS and LES models is based on this length scale parameter l_{DES}. When $d_w < C_{DES}\Delta$ the DES model acts as a RANS model and when $d_w > C_{DES}\Delta$ a subgrid-scale model is applied with a filter width of Δ, showing the functionality of an LES model. The original DES model did show promising results, however it was also observed to contain a number of shortcomings. The DES formulation was based on a wall-normal grid spacing that amply exceeds the boundary layer thickness of the flow. Violation of this condition were shown to result in RANS-LES interfaces within the boundary layer, leading to reduced levels of eddy viscosity when the grid was also not fine enough to correctly resolve the boundary layer. The DES model would not sufficiently capture the velocity fluctuations in the near wall region and so underestimate the resolved Reynolds stresses. The issue was later entitled 'Modelled Stress Depletion' (MSD). The consequence was that the prediction of separation points, in case of flow separation, by the DES model were found to differ with respect to the predictions of RANS-only simulations. Due to the role of the mesh resolution near the wall this phenomenon was referred to as 'Grid Induced Separation' (GIS).

Delayed Detached Eddy Simulation (DDES)
The Delayed Detached Eddy Simulation (DDES) [50] is an adapted DES model that aimed to resolve the issue of MSD. The root of MSD was found to originate in the formulation of the DES length scale that was purely grid dependent. This formulation was then changed to additionally depend on the eddy viscosity field by means of blending functions analogous to a method described by Menter et al. [28]. First a boundary layer sensor, r_d and a shielding function, f_d are specified:

$$r_d = \frac{\nu_\tau + \nu}{\kappa^2 d^2 max(10^{-10}, \sqrt{U_{i,j}U_{i,j}}} \tag{2.34}$$

$$f_d = 1 - \tanh(8r_d)^3 \tag{2.35}$$

where $U_{i,j}$ are velocity gradients [$\mathrm{m\,s^{-1}}$]. The function of r_d assumes a value of 1 in the turbulent boundary layer and decreases to zero towards the boundary layer edge. Contrarily, f_d equals to 0 in the turbulent boundary layer while f_d equals 1 towards the boundary layer edge. With these a new formulation of the DES length scale parameter is given:

$$l_{DES} = d - f_d max(0, d - C_{DES}\Delta) \tag{2.36}$$

Using this definition of l_{DES} the DES model now only enables the LES mode outside the turbulent boundary layer. Due to the nature of this function that delays the switch from RANS to LES mode, the model was named 'Delayed DES'.

Improved Delayed Detached Eddy Simulation (IDDES)
The last adaption of the DES model is the Improved Delayed Detached Eddy Simulation (IDDES) model [46] which aimed to combine two modelling branches: DDES and wall-modelled LES (WMLES). The DDES model showed the possibility of a dual solution and required further revision. The contruction of IDDES was aimed to provide unique solutions as well as to incorporate the advantages of both branches.

The WMLES model is a different approach to reduce the high grid resolution required near the walls of the computational domain. It uses a wall-stress modelling approach to model the behaviour of the flow in a much

thinner near-wall region than the DES method. This results in an interface between the RANS and LES part of the flow that is situated inside the boundary layer. An issue was identified with this approach where the transition between the RANS and LES log-layers was mismatched, known as the *log-layer mismatch* (LLM). The result was an under-prediction of the skin friction coefficient by up to 15-20 % [46]. The development of the IDDES model was to eliminate this issue of the WMLES. The formulation of the IDDES model is discussed in four parts:

- Sub-grid length scale
- DDES branch of IDDES
- WMLES branch of IDDES
- Blending of DDES and WMLES branches

Subgrid length-scale
The definition of the subgrid length-scale, commonly based on the cube-rootof a cell volume (Equation 2.18), was found unsuccessful for general application. In association with the SGS model constants, the (D)DES showed only valid for a certain region of the flow. In this way the model conditions can correctly be calibrated for wall-bounded flows, however it showed insufficient for free turbulent flows. Instead of requiring different SGS model constants for different regions of the flow, the definition of the subgrid length-scale was altered to include a dependency on the wall-distance:

$$\Delta = f(\Delta_x, \Delta_y, \Delta_z, d_w) \tag{2.37}$$

Functions for Δ are specified for three different sub-regions in the flow domain. For high values of d_w, representative of a free-stream region far from the wall, the maximum local grid spacing is considered:

$$\Delta_{free} = \Delta_{max} = max(\Delta_x, \Delta_y, \Delta_z) \tag{2.38}$$

The second region is attributed to that in close vicinity of the wall. The subgrid length-scale should not follow the drastic decrease of the wall-normal grid steps and thus is made dependent on the wall-parallel grid spacing only:

$$\Delta_{all} = f(\Delta_x, \Delta_z) \tag{2.39}$$

Finally, a transition region in between the two limit cases is assumed with a linear dependency on d_w. Additionally, it is assumed that Δ varies within $h_{min} \leq \Delta \leq h_{max}$ at any distance from the wall. A expression is formulated that satisfies all three mentioned functions:

$$\Delta_{wall} = min\{max[C_w d_w, C_w \Delta_{max}, \Delta_{wn}], \Delta_{max}\} \tag{2.40}$$

Where Δ_{wn} is the wall normal grid spacing and C_w is a constant set to 0.15 based on a resolved LES simulation of a channel flow. An example of the variation of the subgrid length-scale across a plane channel with half-width H is presented in Figure 2.4. The solid line represents the case with $\Delta_{wn} \leq C_w d_w$. As long as $d_w \leq \Delta max$, the value of the subgrid length-scale is a constant value of $C_w \Delta_{max}$. When the distance to the wall is sufficiently large so that $d_w > \Delta max$, the subgrid length-scale increases linearly with $C_w d_w$. This occurs until Δ_{max} is reached, after which Δ remains at this value for increasing wall distances d_w. The dashed line corresponds to a plane with a strong wall-normal stretching of the grid. Identical to the solid line, Δ remains a constant value of $C_w \Delta max$ if $d_w \leq \Delta_{max}$. At the moment that $d_w > \Delta max$, a linear growth of Δ is observed that is greater than C_w. This holds until reaching a subgrid length-scale value of Δ_{max}. This specific case illustrates the effects of excessive wall-normal grid stretching and its influence on the subgrid length-scale. It is noted that such a case is undesirable, however the resulting variation of Δ will function in simulations.

DDES branch of IDDES
The first branch that will be discussed considers the DDES model. The IDDES model should only activate this branch when there is no turbulent content in the inflow conditions. A correction function was implemented to avoid unwanted activity of RANS model damping terms when operating in the LES mode. This resulted in reduced levels of eddy viscosity in refined regions of the mesh. To compensate for the background RANS activity, the correction function Ψ was incorporated in the LES length-scale definition:

$$l_{LES} = C_{DES} \Psi \Delta \tag{2.41}$$

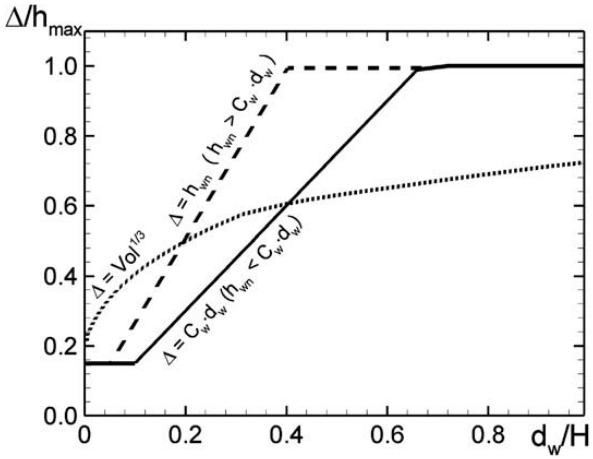

Figure 2.4: Two different functions of the subgrid length-scale accros a plane channel in comparison with the cube-root definition, adopted from [46]

The correction function can be set to $\Psi = 1$ when the background RANS model does not include low-Reynolds numbers low-Reynolds number terms, such as the $k-\omega$ SST model [55]. For the S-A model the following definition is provided:

$$\Psi^2 = min[10^2, \frac{1 - \frac{C_{b1}}{C_1 \kappa^2 f_w^*}[f_{t2} + (1 - f_{t2}) f_{v2}]}{f_{v1} max(10^{-10}, 1 - f_{t2})}] \tag{2.42}$$

where f_w^* is the asymptotic value that f_w approaches for high values of the eddy viscosity. The function reaches $\Psi = 1$ for a subgrid eddy viscosity level of approximately 10ν. The function was proven effective in restoring the eddy viscosity levels of the LES mode, while not disturbing the functionality of the RANS mode.

WMLES branch of IDDES

The next branch corresponds to the WMLES, which is activated when inflow conditions are unsteady and contain turbulent content. It also requires the mesh to be sufficiently refined enough in the boundary layer region for the dominant eddies to be resolved. The coupling of the RANS and LES models is achieved by means of a blended RANS-LES length-scale, which is based on each of the respective model length-scale:

$$l_{WMLES} = f_B(1 + f_e) l_{RANS} + (1 - f_B) l_{LES} \tag{2.43}$$

Where first the blending function f_B is provided:

$$f_B = min(2e^{-9\alpha^2}, 1), \tag{2.44}$$

with

$$\alpha = 0.25 - \frac{d_w}{h_{max}} \tag{2.45}$$

The blending function attains a value in between 0 and 1 within a wall distance of $0.5 h_{max} \leq d_w \leq h_{max}$ as shown with the solid line in Figure 2.5. The result is a rapid switch between the RANS mode ($f_B = 1$) and LES mode ($f_B = 0$). The intention of the blending function is for the blending between the RANS and LES modes to be abrupt so that the dynamics of each model is not excessively intertwined. The next function in 2.54 that will be discussed is the elevating-function f_e. It is formulated to counteract the reduction of RANS Reynolds stresses due to the interaction of the LES and RANS models near the LES-RANS interface. In this way it serves to eliminate the occurrence of the log-layer mismatch. The function of f_e is designed to be close to zero, and therefore inactive, in the following cases:

- when the refinement of the mesh near the wall is sufficient to allow for the use of wall-resolved LES.
- when the final IDDES model functions properly as the RANS background model (the RANS model behaviour would otherwise be disrupted by a non-zero value of f_e).

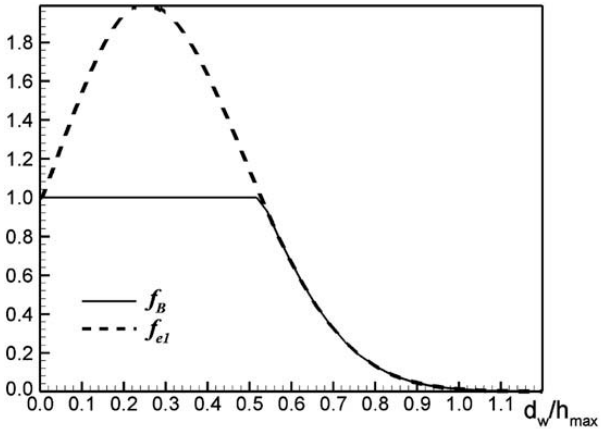

Figure 2.5: Two blending functions arccos a plane channel, adopted from [46]

The function of f_e that satisfies those conditions is given by

$$f_e = max[(f_{e1} - 1), 0]\Psi f_{e2}, \tag{2.46}$$

with

$$f_{e1}(\frac{d}{h_{max}}) = \begin{cases} 2\exp(-11.09\alpha^2), & \text{if } \alpha \geq 0 \\ 2\exp(-9.0\alpha^2), & \text{if } \alpha < 0 \end{cases}, \tag{2.47}$$

$$f_{e2} = 1.0 - max[f_t, f_l], \tag{2.48}$$

$$f_t = \tanh[(c_t^2 r_{dt})^3], \tag{2.49}$$

$$f_l = \tanh[(c_l^2 r_{dl})^{10}] \tag{2.50}$$

where parameters c_t and c_l are model constants that depend on the background RANS model and should result in a value of $f_{e2} = 0$ when either r_{dt} or r_{dl} reach 1.0. For the S-A model they are reported as $c_t = 1.63$ and $c_l = 3.55$. r_{dt} and r_{dl} both result from Equation (2.34) where $r_d = r_{dt} + r_{dl}$ in which the subscript t and l refer to the use of the turbulent viscosity ν_t and laminar viscosity ν, respectively.

The function f_{e1} is only dependent on the grid and is also depicted in Figure 2.5 with a dashed line. It coincides with f_B in the LES-RANS transitions region when $f_B < 1$. It is referred to as an 'elevating' function for the RANS component of the WMLES length-scale. f_{e2} is mentioned to control the intensity of the 'elevating' of the RANS component of the model.

Blending of DDES and WMLES branches

The functionality of the DDES and WMLES branches are combined into the concluding formulation of the IDDES model. The model is intended to select the appropriate DDES or WMLESS model for different regions of the flow. It was unsuccessfully attempted to combine the original DDES length-scale definition with the definition of the WMLES length-scale. Therefore the formulation of the DDES length-scale was modified as follows:

$$\tilde{l}_{DDES} = \tilde{f}_d l_{RANS} + (1 - \tilde{f}_d) l_{LES}, \tag{2.51}$$

with

$$\tilde{f}_d = max\{(1 - f_{dt}), f_b\}, \tag{2.52}$$

$$f_{dt} = 1 - \tanh(8 r_d t)^3 \tag{2.53}$$

With this modified formulation of the DDES length-scale the coupling can be achieved with the WMLES length-scale resulting in a hybrid turbulent length-scale:

$$l_{hyb} = \tilde{f}_d(1 + f_e) l_{RANS} + (1 - \tilde{f}_d) l_{LES} \tag{2.54}$$

In reviewing the performance of the model it was found that in simulations with a turbulent inflow, as aspected, the $r_{dt} \ll 1$ resulting in f_{dt} close to 1.0. Moreover, $\tilde{(}f_b)$ equals to f_B so that the hybrid turbulent length-scale l_{hyb} reduces to l_{WMLES}. Contrarily, when inflow with no turbulent content is considered f_e will become zero, reducing l_{hyb} reduces to $l_{\tilde{DDES}}$.

2.3. Boundary layer modelling

In this section one of the main advantages of the IDDES model is discussed, which is the use of cost effective wall functions. When using the LES or DNS turbulence models for modelling flows with high values of Reynolds numbers a very fine mesh is required near a wall to capture the relevant small scales that contribute to the viscous dissipation of turbulent kinetic energy. This is due to the *no-slip boundary condition* and can result in high aspects ratios of the cells near the wall that introduce mesh induced errors to the solution. To overcome this problem the boundary layer profile can be modelled instead with the use of wall functions so that a coarser grid can be used. The following sections briefly explain the theoretical background of this concept.

2.3.1. No-slip boundary condition

A commonly used characteristic of viscous fluids in numerical simulations is that the relative velocity of the fluid near a solid surface to that of the surface itself is zero. This can be interpreted as if the fluid is stuck to the surface and thus has a velocity that equals the velocity of the surface. This conditions only holds when the attraction force at the fluid-solid interface, also called adhesion, is greater than that between the fluid particles themselves, otherwise called cohesion.

2.3.2. Law of the wall

The concept of wall functions is explained by the theory of the *law of the wall*, based on the work of Launder and Spalding [24]. It stems from a normalized depiction of the mean velocity profile in the wall-normal direction. These quantities are normalised with the use of the friction velocity $u_\tau = \sqrt{\tau_w/\rho}$ [m s^{-1}]. Here ρ represents the water density [kg m^{-3}] and τ_w the wall shear stress [kg m s^{-2}], which is given as:

$$\tau_w = \mu \frac{\partial U}{\partial y}|_{y=0} \tag{2.55}$$

The friction velocity u_τ is used to quantify a dimensionless wall-normal distance y^+ and a dimensionless velocity U^+:

$$y^+ = \frac{y u_\tau}{\nu} \tag{2.56}$$

$$U^+ = \frac{U}{u_\tau} \tag{2.57}$$

In Figure 2.6 both quantities are plotted against each other and by means of observed behaviour empirical functions are described for distinct regions [36]:

- The viscous sublayer holds for $y^+ < 5$ and the corresponding velocity profile is described by a linear relation, given by:

$$U^+ = y^+ \tag{2.58}$$

- The log-law region is represented by $30 < y^+ < 500$ (different upper boundaries are given in literature, e.g. a value of 1000 is given Nichols [32] while Blocken et al. [6] specifies a value of 500-1000). In this region a logarithmic expression applies for the velocity profile that is referred to as the log-law:

$$U^+ = \frac{1}{\kappa} \ln\left(E y^+\right) \tag{2.59}$$

  Here κ is the von Kármán constant and E is a fitting constant, which are approximately 0.42 and 9.79 respectively.

- The transition region in between the viscous sublayer and the log-law region is called the buffer layer and applies to the domain $5 < y^+ < 30$. No fitting function is given for this region and it is therefore recommended to avoid this region by either using a resolved mesh ($y^+ < 5$) or a wall-function based mesh ($30 < y^+ < 500$).

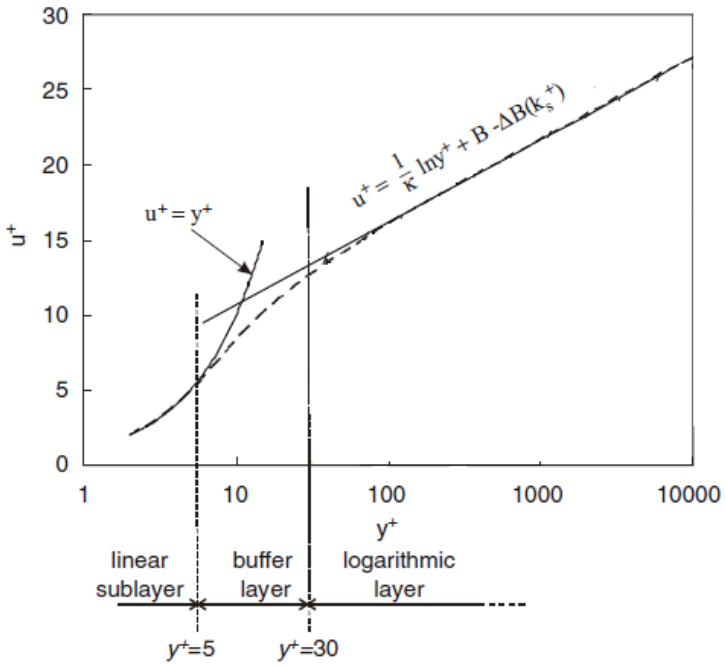

Figure 2.6: Law of the wall, modified from Fig. 2 in Blocken et al. [6]

2.3.3. Surface roughness

In cases where wall functions are used, the surface roughness can be included by alteration of the law of the wall with a roughness function ΔB [6]:

$$U^+ = \frac{1}{\kappa}\ln\left(Ey^+\right) - \Delta B \tag{2.60}$$

The function for ΔB depends on the dimensionless roughness height, K_s^+, and a roughness constant, C_s, that considers the type of roughness accounting for the shape and spacing of the roughness elements. Due to the lack of specific guidelines, a value of $C_s = 0.5$ is generally assumed for channel flow. K_s^+ is defined as follows:

$$K_s^+ = \frac{\rho K_s u_\tau}{\mu} \tag{2.61}$$

In which the K_s is the height of roughness elements [m]. Using this Ks+ value, three regimes are specified for the roughness function ΔB:

- A hydrodynamically smooth regime that corresponds to $K_s^+ < 2.25$. In this regime $\Delta B = 0$, implying that the roughness is sufficiently small to assume no effects on the velocity profile.
- A hydrodynamically rough regime that is applied when $K_s^+ > 90$. In this case the roughness functions is calculated by:

$$\Delta B = \frac{1}{\kappa}\log\left(\frac{K_s^+ - 2.25}{87.75} + C_s K_s^+\right)\sin\left(0.4258[\log K_s^+ - 0.811]\right) \tag{2.62}$$

- And a transitional regime of which the domain is given by $2.25 < K_s^+ < 90$. The roughness function is described by:

$$\Delta B = \frac{1}{\kappa}\log\left(1 + C_s K_s^+\right) \tag{2.63}$$

The effect of the roughness function can be seen in Figure 2.7. In the hydrodynamically smooth regime the roughness function has no influence. In the transitional regime a significant influence is observed of the roughness function and the law of the wall profile is shifted downwards. In the hydrodynamically rough regime the influence of K_s is less significant as the value for ΔB approaches an asymptote for large values of K_s. According to (2.57) the downshift of the function implies an increase of the reference velocity u_τ and

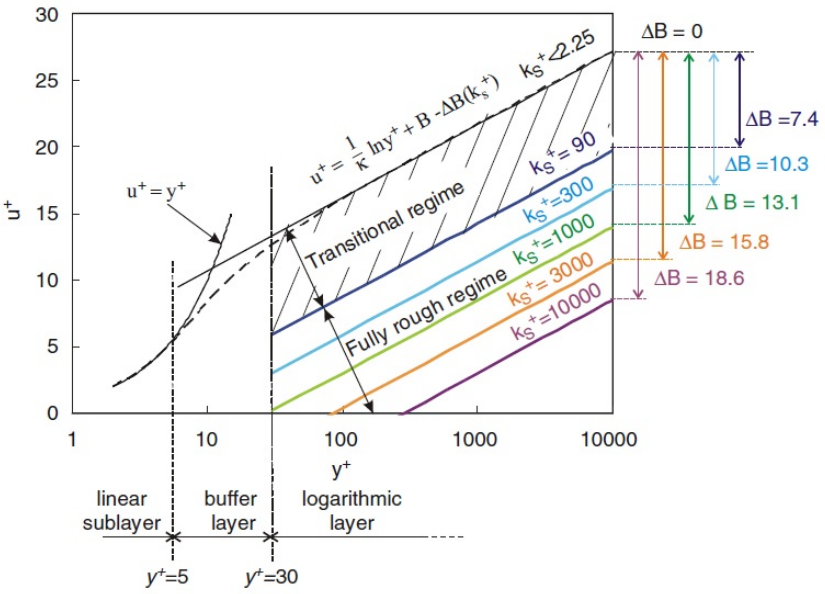

Figure 2.7: influence of the roughness function on the law of the wall, adopted from Blocken et al. [6]

indirectly an increase wall shear stress τ_w. In OpenFOAM this roughness model is considered in a slightly different form:

$$U^+ = \frac{1}{\kappa}\ln(E' y^+) \tag{2.64}$$

Here the roughness parameter ΔB is embedded in the constant E by the following equation:

$$E' = \frac{E}{exp(\Delta B)} \tag{2.65}$$

The roughness model is implemented in OpenFoam through the definition of the wall shear stress (2.55), the log-law (2.64) and the dimensionless velocity (2.57):

$$\nu_t = \frac{\nu y^+}{\frac{1}{\kappa}\ln(E' y^+)} \tag{2.66}$$

which shows that the artificial roughness is included in the calculation of the turbulent viscosity. This is later shown in the specification of the model boundary conditions where wall functions are used for ν_t that include roughness parameters.

2.4. Additional numerical aspects

The implementation of roughness in numerical models, as described in the last section, is an important aspect of this study as it greatly affects the boundary profile. In this section additional aspects are briefly mentioned that are relevant for setting up the simulations and processing of the simulation results.

2.4.1. Courant number

As a requirement for stability of a simulation the Courant–Friedrichs–Lewy (CFL) condition [9] should be considered. It is an important parameter when solving partial differential equations, such as the Navier-Stokes equations, when making use of explicit numerical time schemes. It links the local velocity in the domain with the associated grid spacing and time step so to maintain convergence of the solution. Two of the parameters are controlled by initialization of the simulation, namely the grid spacing of the mesh and the input time step. The CFL criterion is given as the following:

$$C = \Delta t(\sum_{i=1}^{3} \frac{u_{x_i}}{\Delta x_i}) \leq C_{max} \tag{2.67}$$

where Δt is the solver time step [s], u is the flow velocity [$\mathrm{m\,s^{-1}}$] and Δx_i represents grid spacing in different spatial directions for i = 1,2 and 3. C_{max} takes on a value of 1. The condition specifies that an increase of the mesh resolution, so that a finer grid spacing is achieved, should be accommodated with a sufficient decrease of the time step when assuming constant velocity conditions.

2.4.2. Mesh requirements

There are a number of mesh requirements that will be briefly discussed that help increase both the stability and accuracy of the numerical solution.

- The **skewness** of a cell is a measurement of the configuration of the cell with respect to its optimal one. The optimal condition is specified as an equiangular cell configuration, which thus differs between common cell types such as the hexahedra or tetrahedra.
- The **aspect ratio** of a cell is a measure of the severity of the elongation or stretching of a cell. It is given by the ratio of the length of the longest edge to that of the shortest edge. Ideally, an aspect ratio of 1 is considered. However, for one-dimensional flow a stretching in the direction of the flow is allowed so that much higher aspect ratios are viable.
- The **smoothness** of a mesh relates to the change in cell sizes over a certain domain. It ties to the previously mentioned mesh requirements as abrupt changes in cell size often inherently introduce high aspect ratios and skewness values.
- The **non-orthogonality** between cells relates to the face connection between two adjacent cells. Here the face-normal vector is compared to that of the cell-to-cell vector. Ideally, the angular difference between the vectors is kept at a minimum.

2.4.3. Statistical analysis parameters

For the inspection of the velocity fields, three parameters are investigated for comparison between the numerical and test cases. The first quantity is the mean component of the velocity, which is defined as:

$$\overline{u} = \frac{1}{n}\sum_{i=1}^{n} u_i \tag{2.68}$$

with i = 1,2 and 3 specifying each spatial component and with n being the sample size. The next parameter is the standard deviation that denotes a measure of spreading of the fluctuating velocity component. It is given by:

$$\sigma_{u_i} = \sqrt{\frac{1}{n}(u_i - \widetilde{u})^2} \tag{2.69}$$

Finally, the definition of the turbulent kinetic energy is provided:

$$k = \frac{1}{2}\sum_{i=1}^{3} \overline{(u_i')^2} \tag{2.70}$$

2.4.4. Force coefficients

To validate the numerical results also the force coefficients are considered for comparison with test results. The first two force coefficients mentioned are the drag and lift coefficients C_D and C_L. These coefficients are used for expressing the drag and lift forces that act on a body due to interaction with a fluid. Both forces are further elaborated in Section 2.5.1. The coefficients represent single values that incorporates complex model parameters, such as the object shape, relative fluid flow kinematics and fluid conditions. The drag and lift force are respectively given by

$$C_D = \frac{F_D}{\frac{1}{2}\rho A u|u|} \tag{2.71}$$

$$C_L = \frac{F_L}{\frac{1}{2}\rho A u|u|} \tag{2.72}$$

where F_D and F_L are the drag and lift forces respectively [$\mathrm{kg\,m^2\,s^{-1}}$] and A is a reference area of the object [$\mathrm{m^2}$]. The drag coefficient of a cylinder in a fluid flow has been established for a large range of Reynolds numbers as

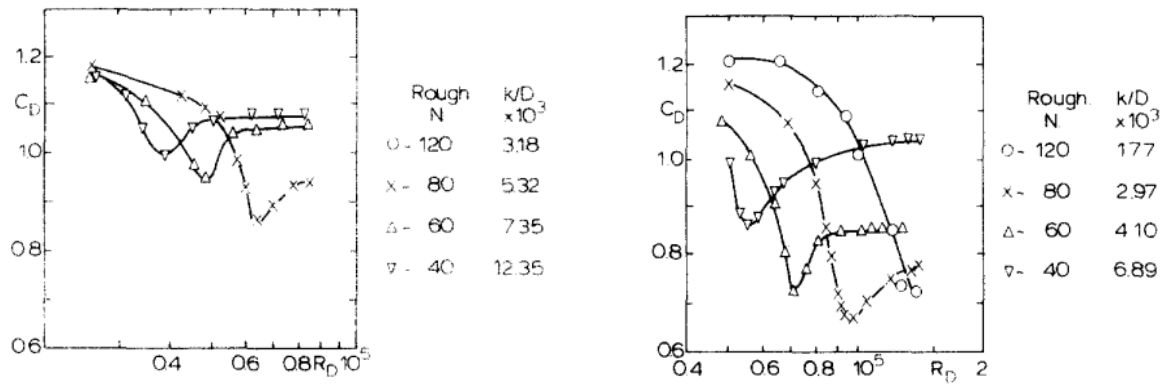

Figure 2.8: Drag coefficient for flow around a cylinder with a diameter of 34 mm (left) and 61 mm (right) as a function of the Reynolds number, adopted from Buresti [7]

shown in Figure 2.8. Both figures show the drag coefficient as a function of the Reynolds number. They also include an overview of the effects of cylinder surface roughness on the drag coefficient. The left figure shows results of fluid flow around a 34 mm cylinder. The right figure includes a number of very small roughness ratios for flows around a 61 mm cylinder. Both figures are included as they indicate drag coefficient values for different Reynolds numbers and roughness-to-diameter ratios $\frac{k}{D}$, with here k being the roughness height [m].

The pressure coefficient is also used for validation. It represents a normalised pressure along the surface of the cylinder and is given by

$$C_p = \frac{p - p_\infty}{\frac{1}{2}\rho u_\infty^2}, \tag{2.73}$$

where subscript ∞ denotes free stream conditions. Pressure coefficient functions from test results for different Reynolds numbers are shown in Figure 2.9. The stagnation point in front of the cylinder corresponds to θ = 0 deg. The associated pressure coefficient at this location has a maximum value of approximately 1 due the normalization with the free stream velocity. From the stagnation point the pressure coefficient values are presented along the cylinder half-plane up to 180 deg.

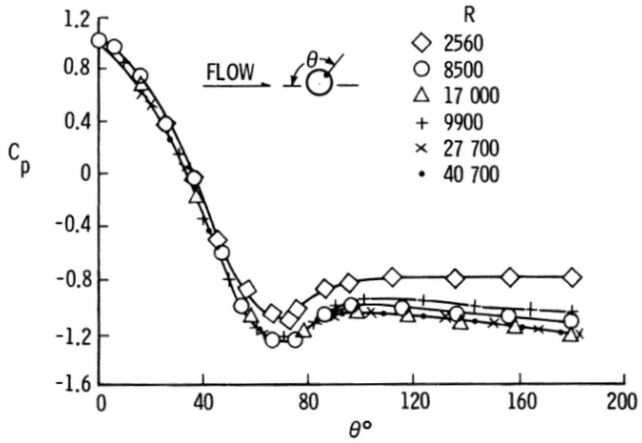

Figure 2.9: Pressure coefficient along the cylinder surface for different Reynolds numbers, adopted from Aeronautics and Administration [2]

2.4.5. Strouhal number

The Strouhal number is a dimensionless parameter that relates to the oscillatory patterns of a fluid. It is given by the following equation:

$$Sr = \frac{fD}{U} \tag{2.74}$$

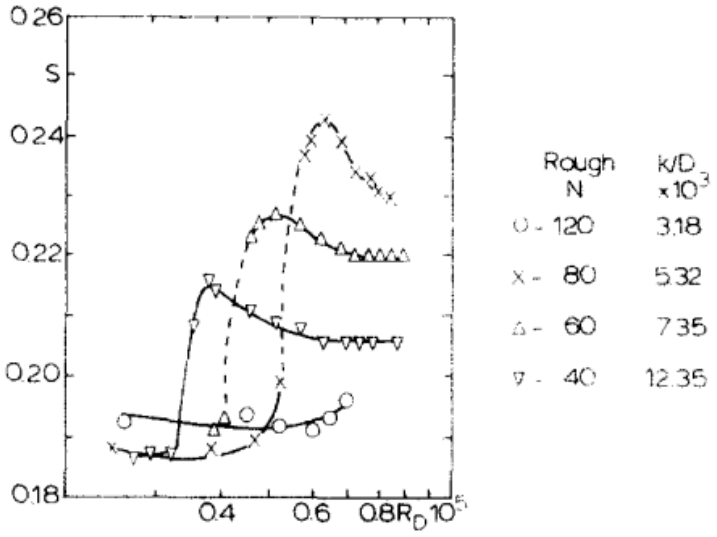

Figure 2.10: Strouhal number for a cylinder with 34 mm diameter including roughness effects, adopted from Buresti [7]

With f being the vortex shedding frequency [Hz] and D being a characteristic length scale [m]. Identical to the drag and pressure coefficient, this quantity has been studied in relation to the Reynolds number. The Strouhal number is presented in Figure 2.10 for a limited range of Reynolds numbers in addition to different $\frac{k}{D}$ ratios. To obtain an estimation for the vortex shedding frequency the previously mentioned lift coefficient is often used.

2.5. Stone stability

The formation of a scour hole around a cylinder can negatively affect the stability of the structure as the depth of the pile foundation reduces and its dynamical behaviour changes. It is for this reason common practise to make use of scour protection methods. The function of scour protection is to limit the sediment transport surrounding the cylinder and thus avoiding the formation of scour holes. A commonly used scour protection method is the deposition of a great number of large rocks in the vicinity of the cylinder base that disrupts the flow patterns near the bottom of the cylinder. This is often combined with the placement of a filter layer, which is made out of smaller sized stones, to prevent sediment from flowing out via pores of the large rocks. It is still possible for the scour protection layers themselves to be damaged and therefore the protection layers should be specifically designed depending on its situational use. In Figure 2.11 different scour protection failure mechanisms are shown [1]:

a) Erosion of the scour protection layer that results in re-exposure of the finer sediment underneath.

b) Incomplete protection of the scour protection layer allowing for the loss of underlying sediment over time.

c) The formation of edge scour due to erosion of finer material surrounding the protection layer. This may lead to local loss of protection material that allows for further erosion. This iterative process results in gradual horizontal elimination of protection material and sediment.

d) Upstream scour resulting in steep bed slopes that increase the instability of the protection layer. Eventually a quantity of sand may slide away, known as a flow slide, displacing the protection material.

The type that is focussed on in this thesis is a). The following sections will first discuss the mechanism by which stones are displacement from a granular bed and the stability criterium for turbulent flows.

2.5.1. Stone entrainment

It is understood that the motion of a stone is initiated by two components of the hydrodynamic force, namely drag and lift. For sufficiently high Reynolds numbers ($Re > 1 \times 10^3$), viscous effects become negligible and

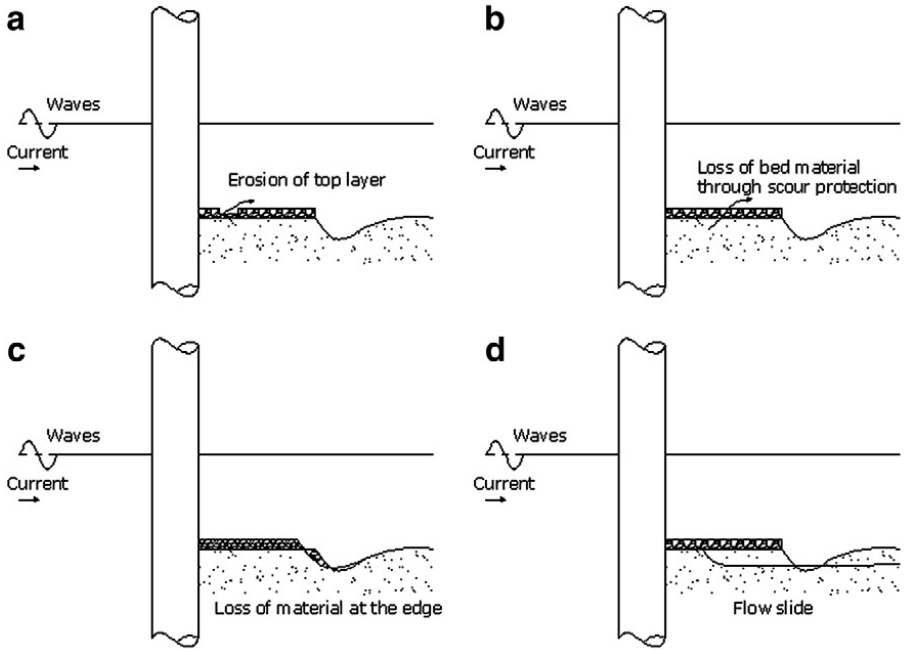

Figure 2.11: Failure mechanism of a scour protection layer due to waves and currents, adopted from Hoffmans and Verheij [17]

it can be assumed that both components are resultants of pressure differences over a body. These pressure differences establish a net force in the direction of the flow, known as drag, and a force normal this direction, known as lift. For this section, the lift force is considered to act in the wall-normal direction. For the mentioned Reynolds number regime, both drag and lift forces are respectively given as

$$F_D = \frac{1}{2} C_D \rho A u |u| \tag{2.75}$$

$$F_L = \frac{1}{2} C_L \rho A u^2 \tag{2.76}$$

These forces represent the steady components of the hydrodynamic loading. However, bed particles are also subjected to fluctuating loads making The issue of stone entrainment is much more complicated. Kalinse [19] mentions two possible sources for the fluctuating component on a particle. The first is the unsteady separation of the flow from a particle. The second are large-scale turbulent structures that originate from the main flow. In Hofland [18] the fluctuating component of the loading is assumed to be generated by the same mechanism as the steady component and is referred to as a quasi-steady force. When considering a relatively time-invariant flow with low levels of turbulent content, so that $|u'| \ll \overline{u}$, the fluctuating drag changes according to Equation 2.75. The resulting quasi-steady drag component of the force is then proportional to:

$$F'_D \propto \overline{u} u' \tag{2.77}$$

Near the bed the turbulent intensity increases so that the extreme values of the fluctuating component $|u'|$ can reach close the value of $\overline{u}$ itself. this results in a new proportionality of the fluctuating drag component, given by

$$F'_D \propto \overline{u} u' + \frac{1}{2} u'^2 - \frac{1}{2} \sigma(u)^2 \tag{2.78}$$

where $\sigma(u)$ is the standard deviation of the fluctuation component [$\mathrm{m\,s^{-1}}$]. The fluctuating lift component is also provided:

$$F'_L \propto a \overline{u} u' + b \overline{u} v' \tag{2.79}$$

The first term of the right side is the result of linear expansion of Equation 2.76, which identical to the first term of the fluctuating drag component. The second term comes from the realization that lift is not only generated from horizontal flow, but can be due to vertical flow as well.

Hofland further investigated the entrainment of stones particular in turbulent flows. He mentions that the force magnitude not only determines the displacement of the stone. This mechanism is also dependent on the duration of the force as well as the application point of the force on the particle. Additional remarks are given about the influence of the size, shape, orientation and position of the stone in the granular bed that all influence the dynamics of a particle. In the end, a general description was provided for the mechanism that caused displacement of a stone particle. The entrainment of stones in bed protections were found to occur during the presence of an increased streamwise velocity in combination with a downward velocity. The hydrodynamically loaded stones are described to initially get lifted by an intense, small-scale fluctuations in the vertical direction. The uprising of the stone from the bed causes additional area to be exposed to the streamwise velocity, making it more easy for it to get dragged along with the flow. This interplay was found to be negatively correlated. An increase in initial lift would further increase the exposed area to the streamwise flow and thus lower the drag force required for entrainment.

2.5.2. Stability criteria

The need to prevent particle erosion from occurring has resulted in the establishment of several stability criteria based on specific hydrodynamic conditions. A well-known formulation for the stone stability in a steady state current is described by the *Shields stability criterion* [45]:

$$\theta_{cr} = \frac{\tau_{cr}}{g(\rho_s - \rho_w)d_s} = \frac{u_{\tau,cr}^2}{g\Delta d_s} \tag{2.80}$$

with τ_{cr} being the critical bed shear stress [kg m s^{-2}], g the gravitational acceleration [m s^{-2}], ρ_s and ρ_w the density of sediment and water respectively [kg m^{-3}] and d_s the sediment grain diameter [m]. $u_{\tau,cr}$ is the critical friction velocity and $\Delta = (\rho_s = \rho_w)/\rho_w$. Once the apparent bed shear stress exceeds the critical shear stress, the respective sediment will be transported by the flow. Due to its derivation for a steady state current, it is not sufficient for estimating the entrainment of a stone in turbulent conditions. However, turbulent features of a flow, such as the near-bed velocity and pressure fluctuations, play a significant role in the dynamics of bed particles [27]. It has been attempted to include empirically determined influence factors to describe turbulence effects in the Shields criterion, but these are based on specific flow simulation resulting in large variety of empirical factor that are often insufficiently validated [51]. Hofland instead adapted this model to account for turbulence in the flow by additionally including the effects of the quasi-steady forces and forces due to accelerations. Its formulation is given by:

$$\Psi_{tot} = \frac{(C_B(\overline{\tilde{u}} + \tilde{u}')^2 + C_M(\overline{\tilde{a}} + \tilde{a}')d)_{max}}{\Delta g d_s} \tag{2.81}$$

where C_B is a combined drag and lift coefficient, C_M is a added mass coefficient, $\overline{u}$ is the average flow velocity [m s^{-1}], u' is the velocity fluctuation [m s^{-1}], $\overline{a}$ is the average flow acceleration [m s^{-2}], a' is the acceleration fluctuation [m s^{-2}] and $\tilde{}$ depicting a projection of the variable on the bed (e.q. $\tilde{u}^2 = u^2 + w^2$). This stability criterion is used to present *indicators* for potentially displacing drag and lift forces. The listing of a mean component with a superimposed fluctuating part implies that the stability of a stone is governed by extreme load conditions. It is therefore considered to perform a statistical analysis of the damage indicator parameters. Hofland himself performed experiments on stone displacement with three pressure sensors in close vicinity of the stone. The pressure sensor locations are shown in Figure 2.12 With pressure signals p_i he listed the following indicators:

- The drag force is obtained from a horizontal pressure difference:

$$D = p_1 - p_3$$

- Drag fluctuations are estimated from associated horizontal pressure difference fluctuations as large-scale streamwise structures are found governing during entrainment. Hereby the small-scale structures are neglected so that a stagnation pressure can be assumed at the sensors. The indicator is given as:

$$D' = p_1' - p_3'$$

- The lift force resulted from local pressure measurements near the top of the stone as it was not possible to generate a vertical pressure difference. During lift of the stone the pressure decreases, so that the following definition for lift was assumed:

$$L = -p_2$$

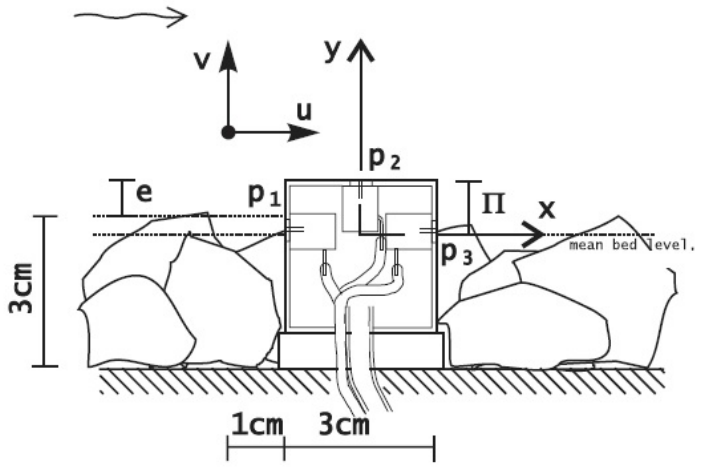

Figure 2.12: Locations of pressure measurement devices in stone entrainment tests, adopted from Hofland [18]

- The lift force fluctuations during stone displacement was assumed directly related to the local pressure as well:

$$L' = -p'_2$$

The idea of specifying drag and lift indicators is adopted for estimating entrainment inducing parameters. This is required because the resolution of the IDDES simulations does not allow for the capturing of individual bed particles or associated small-scale flow phenomena. The following damage indicator parameters are considered for the numerical simulations:

- The drag force and its fluctuating component are estimated from the local wall shear stresses due to near wall flow velocities.

$$D_{ind} = \tau_{wall},$$
$$D'_{ind} = \tau'_{wall}$$

- The horizontal pressure gradient is considered to contribute to the displacements of particles. Similar to the definition of Hofland, the pressure difference can be assumed to result in a net force over a body in streamwise direction and thus indicates a drag force. However, due to the grid scale being larger than bed particles it can also be considered a pressure gradient over the particles themselves. This pressure gradient then suggests a flow acceleration over the bed particles, which in turn represents vertical pressure gradients that are indicative of lift force components. The horizontal pressure gradient is therefore considered a hybrid indicator of both drag and lift forces. The same reasoning applies for the vertical pressure gradient. For analysis the projection onto the bed model is considered via the Pythagorean equation, denoted with $\widetilde{\ }$.

$$H_{ind} = \sqrt{(\nabla p_x)^2 + (\nabla p_z)^2} = \widetilde{\nabla p}$$

- Finally the lift force fluctuations are considered to be related to the spreading of local pressure fluctuations as it shows a severity of the pressure dynamics. Slow-changing pressure fluctuations are not likely to initiate displacements of stones but for ease of analysis the assumption is made that the pressure fluctuations are all of similar time-scale.

$$L'_{ind} = p'$$

With the use of the listed indicators, a variation of the stability formulations given by Equations 2.80 and 2.81 is presented:

$$\Psi = \frac{(\alpha_1 \widetilde{\overline{\tau_w}} + \alpha_2 \widetilde{\tau'_w} + \alpha_3 \widetilde{\nabla p} + \alpha_4 p')_{max}}{(\rho_s - \rho_w) g d_s} \tag{2.82}$$

Here ˜ depicts a projection of the variable on the bed, identical to the definition of Hofland, and coefficients α_1, α_2, α_3 and α_4 are fitting parameters for each of the terms. In this study each of the indicator fields are analysed. However, due to the absence of test data on damage patterns, no fitting of the alpha constants has been performed. The presented formulation of the stability parameter includes the bed shear stress that is found in the definition of Shields stability criterion. This is considered because the local mesh resolution near the bed is insufficient to obtain flow information surrounding individual bed particles, as is required for the variation of Hofland. Additionally, the concept of Hofland's formulation is retained that includes both drag and lift forces and their turbulent component for the entrainment of particles. It is stressed that this formulation is specifically designed to indicate regions of particle entrainment for models with limited resolution, due to the specific definition of the damage indicators.

2.6. Flume measurements

In this chapter the experiments are detailed of which the measurements are used for validation of the numerical results. The experiments were performed at the Eastern Scheldt Flume in the Hydro Hall at Deltares. Here multiple tests were performed to visualize the instantaneous velocity flow field upstream of a cylinder-bed junction by means of Particle Image Velocimetry (PIV). The cylinder was a scaled down version of monopiles found in the North Sea using Froude scaling. During the experiments the surface roughness and the bottom foundation were altered and each case was subjected to a number of predefined wave and current conditions. The observed Reynolds number was approximately 1.4×10^5 based on the channel height and 3.4×10^4 based on the cylinder diameter. The goal was to analyze the influence of the surface roughness of the cylinder as well as the influence of the bed foundation on the upstream flow field due to waves and currents so to ultimately gain insight in the failure mechanisms of bed protection layers.

2.6.1. Experimental set-up

Figure 2.13 an overview of the flume can be seen that was used to perform the tests in. The flume has a total length of 110 meters and can be parted into two smaller flumes with a length of 55 meters each, of which one smaller flume was used for the experiments. The flume has a height of 1.2 m and a width of 1 m. The water depth at the location of the tests was locally calibrated at 0.6 m. In the first section of the flume waves were generated with a piston-type wave generator and by means of water inlet pipes a current could be realized in the flume. The test cases were placed in the middle of the flume at a distance of 24.85 m from the water inlet. The PIV measurements took place in a wooden cabin, which itself is not depicted in the figure. This cabin was to prevent the laser light from doing damage to bystanders as the laser used was of class 4, meaning that it could cause significant eye injuries when exposed in an unprotected manner. Downstream of the tests the waves are eventually broken down by a beach, after which the water flows into a reservoir to be recirculated through the system again. In addition, measurements were taken of the water level and discharge near the flume inlet. Point-velocity measurements were taken by means of Electromagnetic Sensors (EMS) at three different locations along a cross section of the flume. The respective location of each sensor is given in Table 2.2. Here x is the longitudinal distance from the water inlet [m], y is the distance from the left side wall with respect to the flow direction [m] and z is the distance from the bottom wall up [m].

Table 2.2: EMS locations inside the flume

sensor	x [m]	y [m]	z [m]
EMS_1	24.85	0.5	0.055
EMS_2	24.85	0.25	0.255
EMS_3	24.85	0.75	0.455

In Figure 2.14 the experimental set-up can be seen inside the wooden cabin. Here the beam of the laser is diverged and redirected by means of optics so that it illuminates the region of interest, namely the cylinder-bed junction area upstream of the cylinder. A so called 'boat' was installed that allowed for a small region of the surface area to be minimally disturbed by the waves. This is to prevent excessive refraction of the laser beam when it enters the water. Neutrally-buoyant particles are continuously placed in the water which serve as tracer particles. The laser pulses reflect from these tracer particles and are then captured by a camera. From two successive images, containing numerous tracer particles, a processing software can generate a velocity vector field after applying a spatial correlation function. Specifications about the PIV system are described by

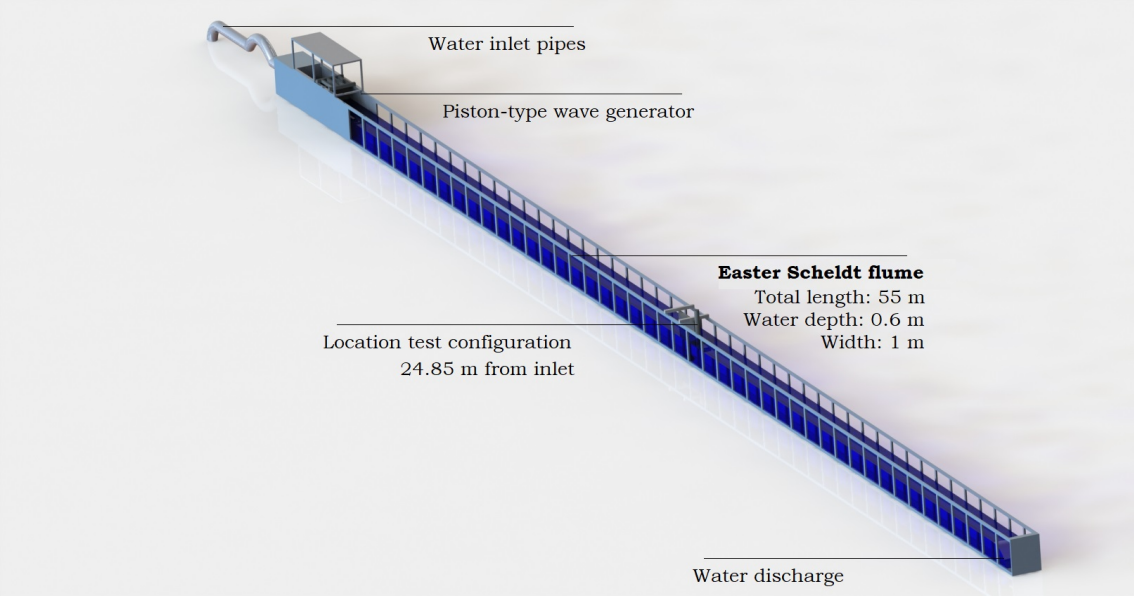

Figure 2.13: Overview of the Eastern Scheldt flume

(a) Laser and optics

(b) 'Boat', calibration plate and the cylinder

Figure 2.14: set-up of the PIV system

Duinmeijer et al. [12]. Field data was acquired with a frequency of 7 Hz, which was limited by the processing speed of the computer and storage of the data.

2.6.2. Test configurations

As mentioned before, the goal of the experiments was to check the influence of the surface roughness of the monopile and the influence of the bed foundation. For this reason different configuration were specified that altered the pile roughness and bed foundation conditions. To observe the effect of the pile and its roughness a **no monopile**, a **smooth monopile** and a **rough monopile** condition were specified. To additionally investigate that of the bed foundation a **smooth bed**, a **mattress bed** and a **rock bed** variation were considered as well. In total 9 different combinations were tested for, which are depicted in Table 2.3. The smooth cylinder had a diameter of 0.158 m and reached sufficiently far above the free surface so water would not overtop in extreme wave conditions. The surface roughness of the rough cylinder was based on marine growth observations of monopiles in the North Sea. When considering the rough cylinder model, a section of the smooth cylinder model was substituted with a rough section. The roughness of this section comprised of ellipsoids,

Table 2.3: Overview of different test configurations

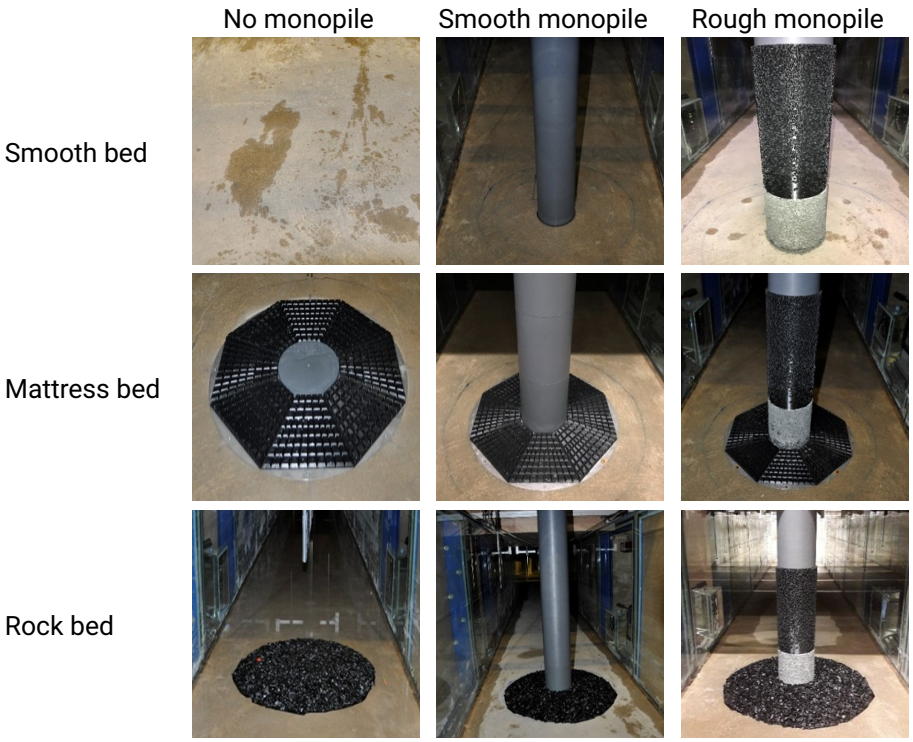

which are simplified representatives of mussels, with a random distribution that increased over the height of the cylinder in terms of occurrence and thickness. The distribution of ellipsoids near the bottom of the cylinder is relatively low and the ellipsoids themselves are also relatively small with a size of approximately 1 mm. The upper section of the rough model has a high distribution of ellipsoids, which are up to 10 mm in size. The rough section was created by means of 3D-printing. The mattress bed was built from eight identical segments, that formed a circular structure when aligning the corners. The segments are partially cut over length and width so that an uneven surface geometry is formed of cubical shapes. Finally, the rock bed consisted of smaller rocks with a size of approximately 5 mm, creating a porous medium. The shape of the outer circumference of the rock bed approximated a circle with a diameter of 34 cm. The height of rock bed was greatest near the centre at around 5 cm and reduced to zero at the outer diameter.

2.6.3. hydrodynamic test conditions

In the flume different hydrodynamic test conditions were produced to capture the relevance of the wave specification, in terms of the K_C number, and that of the current conditions, in terms of the Reynolds number (see Equation 2.1). The Keulegan-Carpenter number, K_C, is defined by

$$K_C = \frac{U_m T}{D} \tag{2.83}$$

in which U_m is the maximum value of the orbital velocity [m s^{-1}], T is the wave period [s] and D is a characteristic length scale [m]. The wave conditions were produced with a piston-type wave generator and a current was realized using water inlet pipes. Each of the test configurations was subjected to the following types of test conditions:

- Regular waves
- NewWaves
- Currents
- Regular waves with a superimposed current

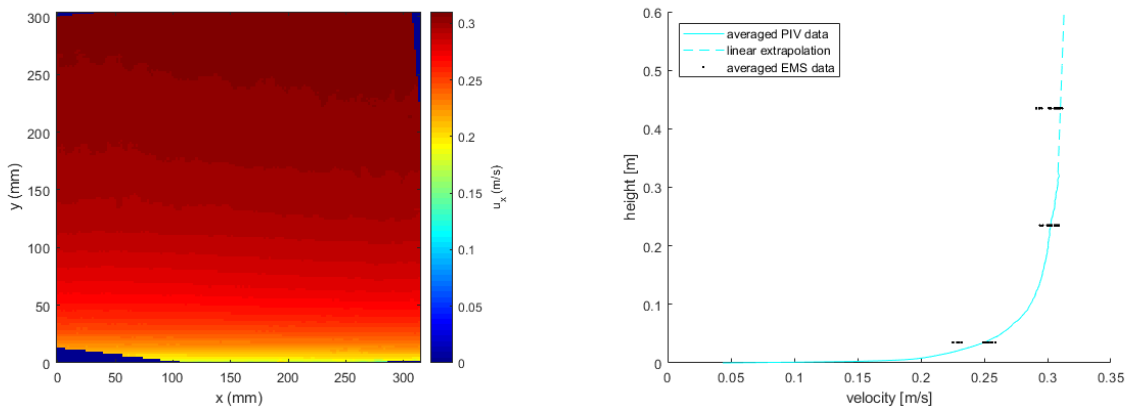

Figure 2.15: Average streamwise velocity field (left) and associated velocity profile (right)

- NewWaves with a superimposed current

Each specific test condition consisted of multiple variations of that condition, altering for instance the current velocity, the wave frequency and the wave amplitude.

2.6.4. Open channel velocity profiles

In this section an example of the post-processed velocity profiles are shown and additionally it is described how the roughness parameter ΔB and friction velocity u_τ are approximated from those profiles. The data from only one test case is considered, namely the open channel case with a smooth bed and no monopile. This allowed for the investigation of an undisturbed boundary layer. First the averaged velocity field is obtained by averaging over 2100 frames, which represents 5 minutes of field sampling at 7 Hz. This averaged field is shown left in Figure 2.15. The sampled field had a size of approximately 300 x 300 mm. However, the field is slightly skewed due to the observing cameras that were placed under an angle. y represents the height dependent variable and x is the space variable in longitudinal direction of the flow. The field also needed re-calibration of the height variable so that bottom wall was located at $y = 0$ mm. The calibration parameter $y_{cal} = 156.7$ mm was obtained from the raw data fields with a pixel-accuracy of 1.9142 [mm]. By additionally space-averaging over the x-variable a velocity profile was obtained, shown right in Figure 2.15. This figure also includes the point-velocity measurements of the EMS's together with a linearly extrapolated line, based on the slope of the velocity profile. The extrapolated line is used to estimate the free surface velocity that, in turn, will be required for the estimation of the boundary layer thickness δ. In general, the boundary layer thickness is defined as 99% of the free surface velocity. Within the turbulent boundary layer, the log-law (see Equation 2.60) holds under the following conditions [36]:

$$y^+ > 30, \frac{y}{\delta} < 0.3$$

where y is distance from the wall. Using these conditions a region in the velocity profile can be specified through which the log-law can be fitted. When using the log-law as fitting function two fitting parameters will be obtained, namely the roughness parameter ΔB and the friction velocity u_τ. This roughness can be specified to OpenFOAM which will introduce an artificial roughness to the bottom so that similar near-wall flow behaviour is obtained. In Figure 2.16 the normalised velocity profile is provided so that the logarithmic region is more easily located. The velocity profile is slightly shifted downwards with respect to the logarithmic region for smooth walls. This implies that the bottom wall of the channel contains a roughness. By using function fitting of the log-law through the logarithmic region of the boundary layer the fitting curve is obtained, shown in the figure as a solid black line. It can be seen that there is a very good agreement between the theoretical fitting function and the experimentally obtained data. The corresponding fitting parameters are $\Delta B = 2.6$ and $u_\tau = 0.0143$ m/s. Those parameters are translated using Equation (2.62) into a roughness height K_s of approximately 5.2×10^{-4} m when assuming a roughness constant C_s of 0.5. The K_s and C_s are used as input parameters for OpenFOAM.

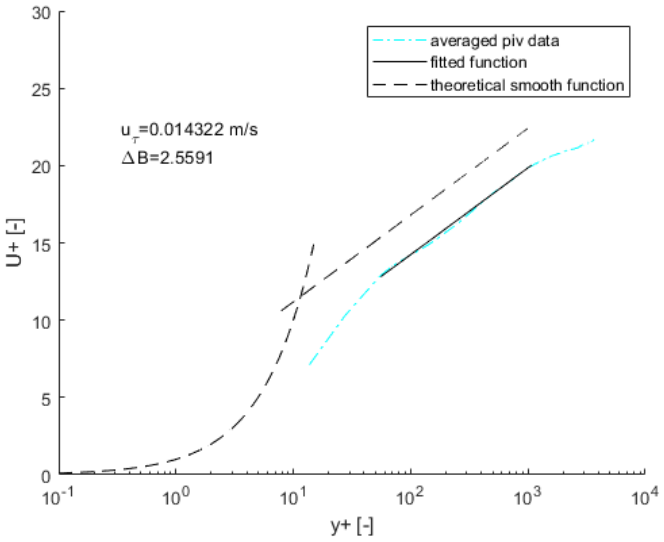

Figure 2.16: Normalised velocity profile of the open channel

3

Numerical models

The numerical models follow from a simulation strategy that considers a basic model, acting as a foundational case, and builds upon this case by subsequently adding features of interest. The numerical strategy allows for the investigation of individual stages of the numerical model during its elaboration. This is an important aspect of the strategy as the simulation model used - the Improved Delayed Detached Eddy Simulation (IDDES) - has uncertainties in terms of its applicability and accuracy in different regions of the flow. The method will be used to examine how well the simulation model predicts flow features with respect to those obtained from PIV measurements of the test cases. In the sections that follow a preliminary numerical study is first discussed. Then the numerical strategy is further emphasised and an overview of the different meshes and simulations settings is provided.

3.1. Preliminary numerical study

Initially, a number of test simulations were performed to asses the numerical capabilities of simulating an open channel case and its ability to generate basic flow properties comparable to those observed in the test cases. Here especially the near-wall performance was of interest since similar regions are studied in the later phases. Recalling that the IDDES model switches to the RANS model in the near-wall region, the choice was made to consider the RANS turbulence models for the test simulations. In total three different RANS models were used, namely the Spalart Allmaras, $k-\omega$ SST and realizable $k-\epsilon$ models. Only the first two models have IDDES variants, but still the realizable $k-\epsilon$ model was investigated to increase the number of test simulations for future comparisons. The numerical domain was representative of a small section of the flume and had

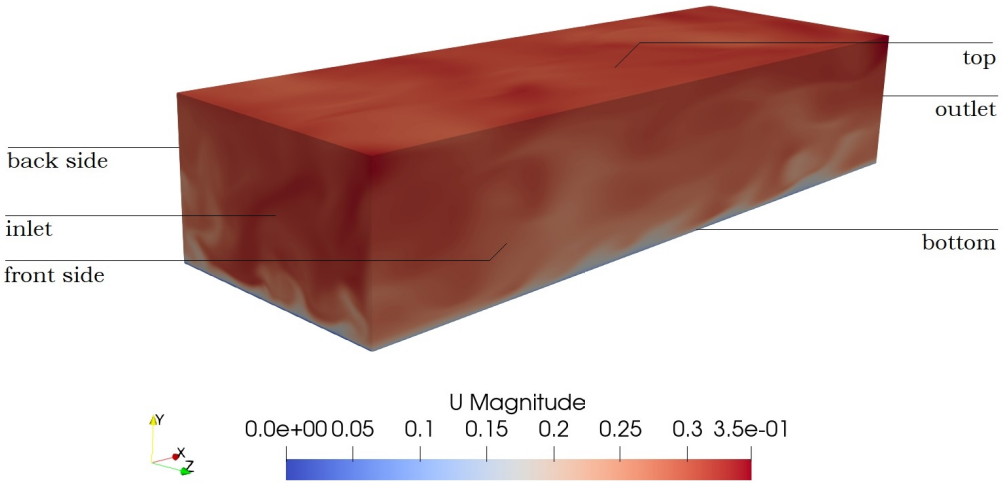

Figure 3.1: Flow domain and patch definition

a length, height and width of 3 m, 0.6 m and 1 m, respectively. This domain is considerably smaller than the size of the flume, which was made possible with the use of *cyclic boundary conditions*. This boundary condition redirects the field variables from one patch to another patch and was applied to connect the inlet and outlet patches, as well as to the side patches in transverse direction. See Figure 3.1 for an overview of the mesh and its patch definitions. The cyclic boundary condition establishes a continuous flow through the domain in which the field variables can develop according to the applied boundary conditions at the top and bottom of the domain. The simulation is initiated with a mean volume-averaged flow velocity $\overline{U}$ of 0.3 m/s in accordance with the flow velocity obtained from discharge measurements in the test flume. The mean flow velocity is enforced by means of an additional momentum source term that iteratively converges to zero when the mean volume-averaged velocity approaches the desired value of $\overline{U}$. The main variable of interest was the mean flow velocity from which the mean velocity profiles over the channel height were obtained. In particular the velocity profile in the middle of the channel was reviewed as this coincided with the region that was observed with the PIV measurement system. Besides comparison of the mean velocity profiles, the profiles were also used to estimate the roughness parameter ΔB and the friction velocity u_τ with the use of the function fitting of the log-law. This process was also applied to the measured velocity profile as explained in Section 2.6.4.

3.1.1. Numerical roughness

In this section an interesting observation is described regarding the simulated boundary layers with the use of function fitting of the log-law in the logarithmic region of the mean velocity profile. The first RANS model used was the realizable $k-\epsilon$ model. It was used to generate mean streamwise velocity profiles for three simulation cases with each case having a different bottom roughness ΔB. The specifics of the roughness input parameters are provided in Table 3.1. A reference roughness height of 9×10^{-4} m was considered that is the same order of magnitude of the K_s value found for the test flume.

Table 3.1: Roughness parameter input

Case	K_s [m]	C_s
Smooth bottom	0	0.5
Moderately rough bottom	0.009	0.5
Rough bottom	0.09	0.5

The velocity profiles of the three cases can be seen in Figure 3.2 that have integrated a smooth, moderately rough and very rough bottom. In addition, the respective fitting curves are shown with solid lines. The figure

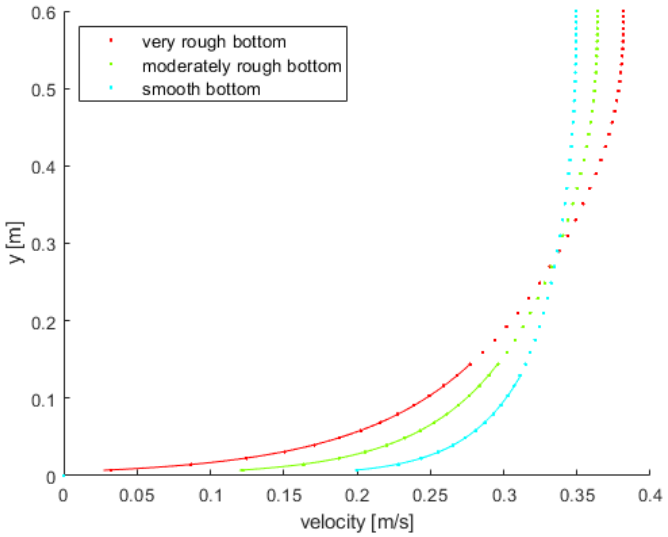

Figure 3.2: Mean streamwise velocity profiles and their respective fitting curves (solid lines) for wall-bounded flows with different bottom roughnesses. Simulations are based on the realizable k-ϵ model

shows that the fitting curves are in good agreement with the mean boundary layer velocities. Interestingly, it

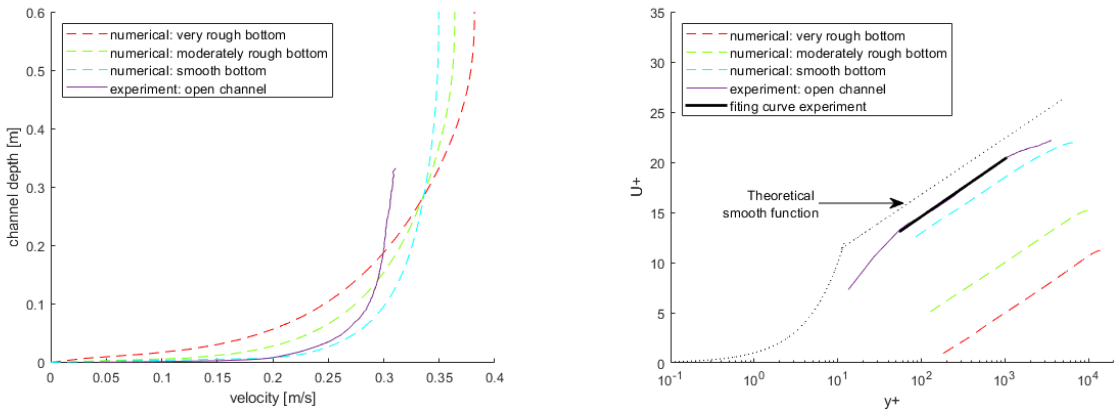

Figure 3.3: Average mean streamwise velocity profile comparison between numerical and test cases, dimensional (left) and dimensionless (right)

was found that the first fitting parameter ΔB did not correspond the to the intrinsic ΔB applied to the wall function via the roughness input parameters K_s and C_s. Further investigation showed that there is an additional roughness present in the form of a positive ΔB, even when a smooth wall function is applied to the bottom wall. To illustrate this issue, the velocity profiles of the experimental and numerical cases are compared in Figure 3.3. Both figures show a misfit of the numerical results with respect to a theoretical smooth case. The left figure shows the dimensional velocity profiles to give a better visual representation of the misfit. It is clear that the bottom roughness influences the shape of the velocity profile over the height of the channel. In the boundary layer the profiles tend to spread over a wider range of flow velocities for higher values of the bottom roughness, or in other words the gradient of the boundary layer decreases for increasing ΔB. The highest gradient is observed in case of a flow over a smooth bottom, but still the inclination of this profile fails to reach that of the experiment case. This already shows that the velocity profiles are not 'smooth enough' and suggests that there is a additional roughness included in the numerical simulations. The right figure shows the dimensionless velocity profiles which allows for a better comparison between the velocity profiles and established literature. The theoretical smooth function is included as reference. As expected, the downwards shift of the profiles corresponds to the roughness of the bottom. Here it clear to see that the numerical case that is being modelled with a smooth bottom is also shifted with respect to the theoretical smooth function. It is more shifted downwards than the fitting curve of the test data, confirming the speculation that indeed the numerical profiles seem to include an additional roughness, which will be referred to as *numerical roughness*.

3.1.2. Iteration error

Further examination of this issue also shows a difference in the second fitting parameter, the friction velocity u_τ, obtained from both function fitting and by direct extraction during the simulation. This is a known issue as others [31] already stated that the wall shear stress is underestimated by approximately 20%. This is expected to be the result of a linearization error. Equation 2.55 is applied to calculate the wall shear stress, which requires a local velocity derivative with respect to the wall-normal distance. This is an approximation that will approach the true wall shear stress when the discrete grid size tends towards an infinitesimally small distance. However, the grid size near the wall is bound in size as the wall functions require a dimensionless wall-normal distance y^+ of at least 30 (see Section 2.3.2). Now since the first grid point is located in the logarithmic region of the boundary layer, the local development of the boundary layer profile is strictly non-linear. It is therefore that a linear approximation of the velocity derivative, and consequently the wall shear stress, is inaccurate. This problem is sketched in Figure 3.4 where both the true and linearly estimated velocity derivative slopes are depicted. D_{true} is the slope that corresponds to the derivative of the log-law (Equation 2.60) at the location of the fictional wall cell centre:

$$D_{true} = \frac{du^+}{dy^+} = \frac{1}{\kappa y^+}\Big|_{y=\frac{1}{2}\Delta_{wall}} \tag{3.1}$$

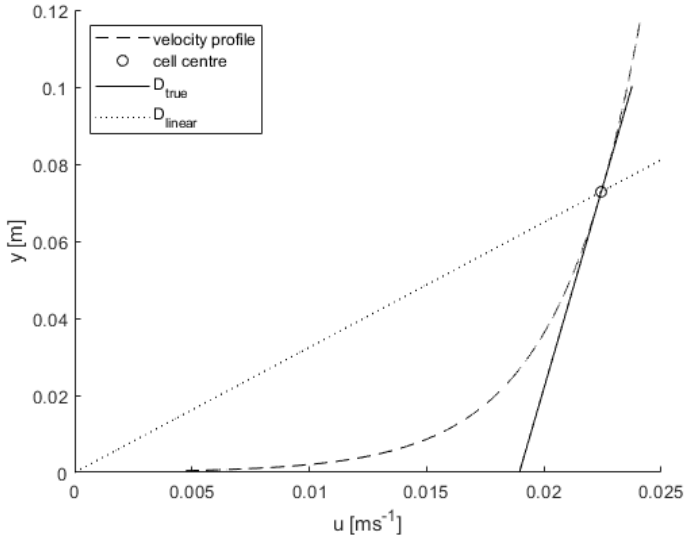

Figure 3.4: Velocity profile with the linearly approximated slope from the wall versus the true slope

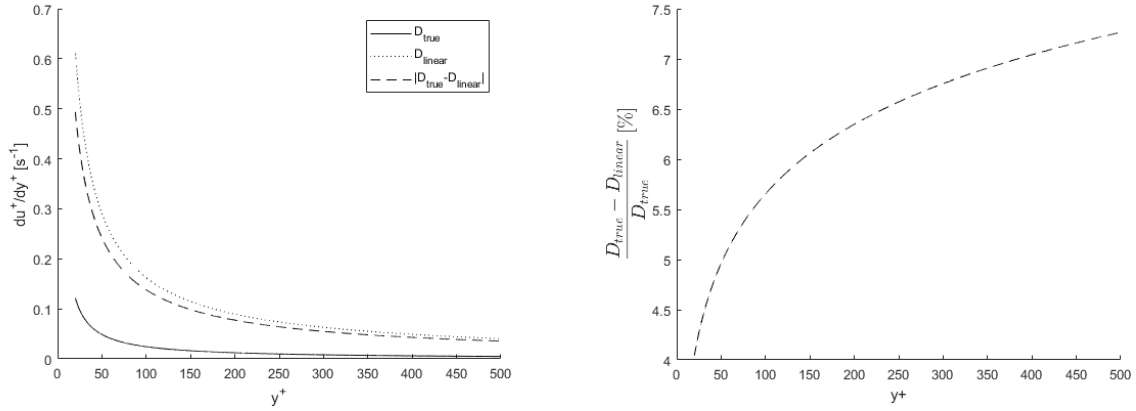

Figure 3.5: Derivative functions D_{true} and D_{linear} and their difference as a function of the first cell centre distance to the wall (left) and the relative error between both functions (right)

Where $\frac{1}{2}\Delta_{wall}$ represents the cell centre of the first wall-normal cell. D_{linear} is the linearly approximated slope from the wall and is described by:

$$D_{linear} = \frac{\Delta u^+}{\Delta y^+} = \frac{\frac{1}{\kappa}\ln(Ey^+) - \Delta B}{y^+}|_{y=\frac{1}{2}\Delta_{wall}} \tag{3.2}$$

Note that in the figure these derivatives are displayed in a dimensional axis system for visual interpretation, which requires a normalisation factor of $\frac{u_\tau^2}{\nu}$. It is clear from the figure that the accuracy of the linear slope estimation to the true slope is dependent on the distance of the first cell centre from the wall. In Figure 3.5 the derivative functions D_{true} and D_{linear} are shown for a large domain of y^+ values for which are normally considered for first wall-normal grid step size when using wall functions. In the left figure it is observed that the linearly estimated derivative D_{linear} approaches the function of D_{true} for high values of y^+. The figure also includes the absolute difference between both function which shows a steady decline for increasing values of the wall-normal grid spacing. This implies that in order to maximally reduce the approximation error of D_{linear} the local grid spacing at the wall should be chosen as large as possible. However, the opposite conclusion is made when viewing the relative error between both function. This is depicted in the right figure. Here is it clear to see that due to the declining nature of D_{true} that approaches zero faster then D_{linear}, actually an increase in the relative error between both functions is seen. The derivative and corresponding difference values are only indicators as they depend on variables such as u_τ and ν, but the general idea still

applies in determining the trend of the error functions. For this reason the simulations are considered with a wall-normal grid spacing that is near the low end of the spectrum of suggested y^+ values.

It is important to further discuss the extend in application of this incorrect wall shear stress, which most importantly is integrated in the wall functions. This will affect the boundary layer in the following iterative manner:

1. Linearization error in the estimation of the wall shear stress so that an inaccurate wall shear stress is estimated
2. Application of the inaccurate wall shear stress in the calculation of the boundary layer profile through wall functions embedded in ν_τ, resulting in an incorrect instantaneous boundary layer profile
3. Linear re-estimation of the wall shear stress, which is based on an incorrect boundary layer, during the next iteration.
4. Return to step 2

This iteration error shows that not only the fitting parameters are inaccurate, but the boundary layer profile itself misrepresents the assumed boundary conditions. This explains the observation of an additional roughness: **A logarithmic wall function is applied (which is clear from Figure 3.2) but it is based on an inaccurately estimated wall shear stress, resulting by iteration in an boundary layer profile that does not fully correspond to the applied wall boundary conditions**. It is important to note that this only becomes apparent when using normalisation of the velocity profile by means of the fitting parameter u_τ. When using the friction velocity that is derived from the directly retrieved wall shear stress, which is known to be underestimated, the errors in both the velocity profile and the friction velocity tend to partially cancel when calculating the normalised velocity profile. This is illustrated in Figure 3.6. The profiles now seem to be situated at the correct level, however the slope, which is a characteristic feature of the boundary layer profile, is misrepresented. To conclude this section, Table 3.2 is provided that shows the relative error of the applied ΔB and u_τ retrieved from OpenFOAM with respect to those obtained from function fitting for three different RANS models: Spalart Allmaras, $k-\omega$ SST and realizable $k-\epsilon$. Referring to Table 3.2 two cases are considered for each model, which include either the smooth bottom with a roughness height of $K_s = 0$ m or the moderately rough bottom with $K_s = 9\times10^{-4}$ m. It shows that of these models the realizable $k-\epsilon$ model contains the largest errors for both ΔB and u_τ, while the Spalart Allmaras model contains the smallest error for both parameters.

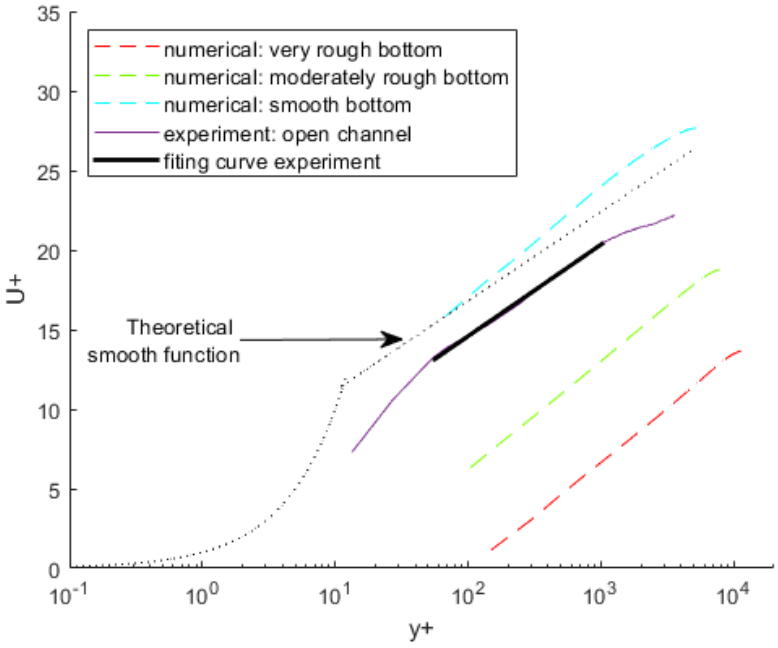

Figure 3.6: Average velocity profile comparison between numerical and test cases. Numerical cases are normalised using the directly extracted wall shear stress from OpenFOAM. Simulations based on the realizable k-ϵ model

Table 3.2: RANS model comparison of ΔB and u_τ for a bottom wall with $K_s = 0$ m and $K_s = 9 \times 10^{-4}$ m

turbulence model	ΔB applied in wall function	ΔB error from function fit	u_τ extracted from OpenFOAM [m s^{-1}]	u_τ retrieved from function fit [m s^{-1}]	relative u_τ error
Realizable k-ϵ	0	3.72	0.0126	0.0158	0.25
Realizable k-ϵ	2.02	3.60	0.0129	0.0160	0.24
k-ω SST	0	1.98	0.0108	0.0127	0.17
k-ω SST	1.82	2.33	0.0119	0.0140	0.18
Spalart Allmaras	0	1.25	0.0115	0.0121	0.06
Spalart Allmaras	1.98	1.79	0.0127	0.0135	0.06

3.1.3. Initial conditions

For the different turbulence models appropriate initial conditions had to be specified. The input parameter values used for the simulations are summarized in Table 3.3.

Table 3.3: Initial parameter conditions for the RANS turbulence models

Parameter	U [m s^{-1}]	p [m^2 s^{-2}]	I [–]	l [m]	$\tilde{\nu}$ [m^2 s^{-1}]	k [m^2 s^{-2}]	ϵ [m^2 s^{-3}]	ω [s^{-1}]
value	0.3	0	0.05	0.076	1.4×10^{-3}	3.38×10^{-4}	1.34×10^{-5}	0.44

The following equation were used to estimate the initial values.
Turbulent intensity:

$$I = \frac{u'}{U} \tag{3.3}$$

Hydraulic diameter:

$$D_h = \frac{4A}{P} \tag{3.4}$$

where A is the cross sectional area of the flow domain [m^2] and P the wetted perimeter [m].
Turbulent length scale:

$$l = 0.07 D_h \tag{3.5}$$

Modified turbulent viscosity:

$$\tilde{\nu} = \sqrt{\frac{3}{2}}(UIl) \tag{3.6}$$

Turbulent energy:

$$k = \frac{3}{2}(UI)^2 \tag{3.7}$$

Turbulent dissipation rate:

$$\epsilon = C_\mu^{\frac{3}{4}} \frac{k^{\frac{3}{2}}}{l} \tag{3.8}$$

where C_μ is a constant with a value of 0.09.
Specific turbulent dissipation rate:

$$\omega = C_\mu^{\frac{-1}{4}} \frac{\sqrt{k}}{l} \tag{3.9}$$

3.2. Numerical strategy

The numerical base model is an open channel case representing a shortened domain of the flume than that used for the experiments, similar to the domain of the numerical preliminary study. This simulation additionally functions as a *precursor* simulation due to this case also generating the necessary inlet flow conditions for successive simulations. This base model is then expanded on by introducing in one case a cylinder, and in another case a bed protection layer. The last numerical model includes both these features, resulting in a combined model of the cylinder and the bed protection layer. For each model only current conditions are considered. Figure 3.7 shows an overview of the described strategy and its numerical models. In the next sections each different model is further detailed.

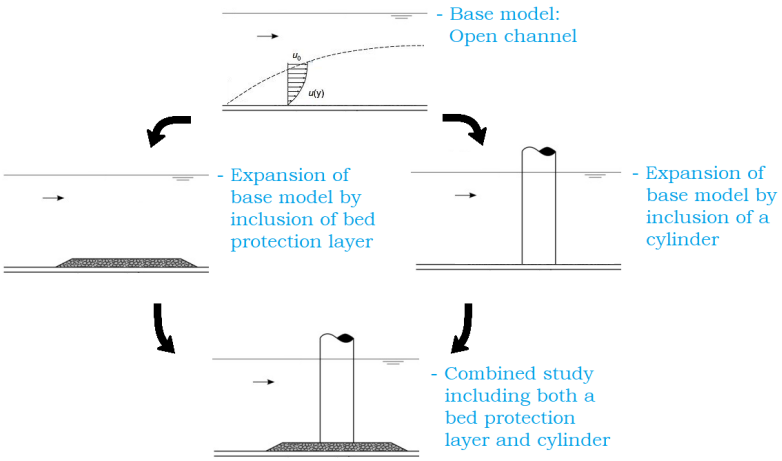

Figure 3.7: Visual representation of the numerical strategy

3.2.1. Open channel model

As stated before, this numerical model is also considered a precursor simulation. It was made using the meshing software Salome. Salome allows for the construction of complex meshes using automatic quadrangular or triangular meshing of specific sub-regions while providing a large degree of freedom in the meshing specification. The domain of the model is 3 x 0.6 x 1 m in size, which is in agreement with the width and height of the test flume. The simulation is initiated with a mean flow velocity of 0.3 m/s in accordance with the flow velocity obtained from discharge measurements in the test flume. On top of this mean flow field a randomly fluctuating velocity signal is added to represent an artificial turbulent component of the velocity field. The open channel simulation has the important function of then developing a flow field with converged turbulence conditions that correctly correspond to the applied boundary conditions. This is established by assigning a *cyclic boundary condition* to the inlet and outlet face of the domain. This boundary condition redirects the field variables at the outlet patch to the inlet patch, essentially assuring a continuous flow through the domain in which the field variables can develop according to the applied boundary conditions. The mesh itself is created according to mesh specification for a periodic channel flow simulation described by Gritskevich et al. [16]. The following general mesh requirements are listed:

- Streamwise cell size (Δx) that is 10 % of the channel half height
- Spanwise cell size (Δz) that is 5 % of the channel half height
- Wall-normal cell size (Δy) that is 5 % of the channel half height in core flow. The size of Δy near the wall reduces to 1.25 % of channel half height, which was found to be too small with respect to the limitation of the wall functions. To avoid y^+ values smaller than a conservatively chosen value of 40, accounting for fluctuation of this variable due to turbulence, a cell size Δy near the wall of 3% of the half channel height was considered.

The authors performed an analyses on the performance of four different grids that all used the IDDES model. In particular the effect of the wall-normal step size was studied when comparing IDDES simulation with and

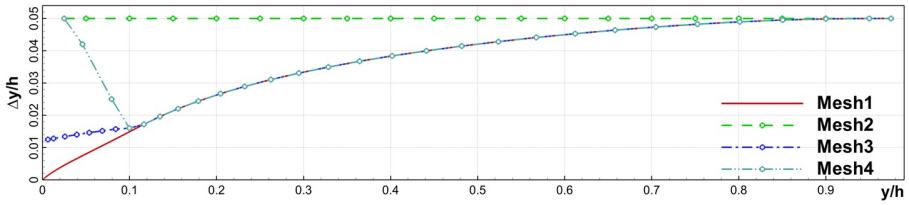

Figure 3.8: Distribution of wall-normal step for four different grids, adopted from Gritskevich et al. [16]

without the use of wall functions. The cell distributions of the different meshes are shown in Figure 3.8. It was mentioned that Mesh 1 satisfies conventional mesh requirements for SSTIDDES - the IDDES model based on the $k-\omega$ SST model - simulations without the use of wall functions. Mesh 2 has a uniform wall-normal cell distribution, which applies to LES simulations that make use of wall functions. Mesh 3 and 4 have cell distributions that are similar to Mesh 1, however the grid steps in the near wall region are varied. It was found that the performance of Mesh 3 was most comparable to that of Mesh 1 and therefore the wall-normal distribution for Δy listed above was recommended when using wall functions. The cell distribution of Mesh 3 was initially recreated for the open channel case of this thesis. However, it was found that the wall-normal grid size Δy was too small as the y^+ values obtained from simulations were smaller than the limit value of 30. Therefore the near wall grid size was increased to approximately 3% of the channel half height, which represents a wall-normal distribution in between those of Mesh 3 and Mesh 4. The total mesh can be seen in Figure 3.9. During this simulation two sections will be sampled. The first is the outlet patch from which the velocity and $\tilde{\nu}$ fields are extracted to be used as inlet condition for the other simulation cases. This is done by means of the *timeVaryingMappedFixedValue* boundary condition that reads in the saved variable fields and interpolates the field in case the grid resolution differs from the initial model. The sampling frequency of 400 Hz was considered for this patch due to the time step limitation that the Courant number enforces for stability of the simulation. The second region of interest corresponds to the area that was observed with the PIV measurement system. For this wall-bounded plane normal to the spanwise (z) direction is sampled with an area of 0.3 x 0.3 meters at 10 Hz. The field variables of interest are the individual velocity components. Finally, the applied boundary conditions for this case are given in Table 3.4

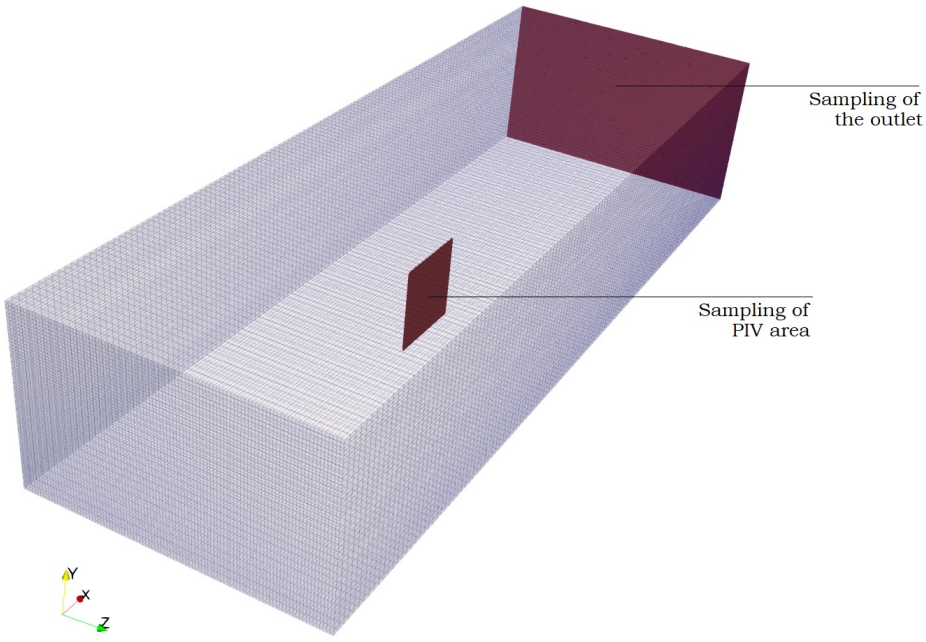

Figure 3.9: Numerical model of the open channel case with the sampled regions highlighted

Table 3.4: Boundary conditions of the open channel case

Boundary	ν_t [$m^2 s^{-1}$]	$\widetilde{\nu}$ [$m^2 s^{-1}$]	p [$m^2 s^{-2}$]	ν [$m s^{-1}$]
inlet	cyclic	cyclic	cyclic	cyclic
outlet	cyclic	cyclic	cyclic	cyclic
top	zeroGradient	zeroGradient	zeroGradient	slip
bottom	nutURoughWallFunction	noSlip	zeroGradient	noSlip
sides	zeroGradient	zeroGradient	zeroGradient	slip

3.2.2. Open channel model including a cylinder

The first successive model is an open channel case from which a cylinder with a diameter of 0.158 meters was extruded, again referring to the cylinder used in the test case. This model was also constructed with the use of Salome. The domain was enlarged in length by a factor of two to account for the pressure diffusion downstream of the cylinder, increasing its size to 6 x 0.6 x 1 meter. The flow inlet conditions originate from the precursor simulation using the timeVaryingMappedFixedValue boundary conditions as described in the previous section. The mesh requirements that were used as a guidelines for the first numerical model are also applied to this case. An additional effort was made to reshape the mesh around the cylinder in a circular manner, as seen in Figure 3.10. This was to reduce instability issues that were observed due to high non-orthogonality values occurring in the mesh. An overview of the total mesh can be seen in Figure 3.11. This time three sections are sampled for post-processing of which one is already discussed, namely the area that was examined with PIV measurements. The second is the surface of the cylinder from which the local pressure and velocity values are sampled to determine the drag, lift and pressure coefficient that can be used for validation of the simulation. The third section to be sampled is the surface area surrounding the cylinder so that the flow patterns and associated hydraulic forcing patterns can be identified. Here the pressure, velocity and shear stress values are examined. All section are sampled with a frequency of 10 Hz.

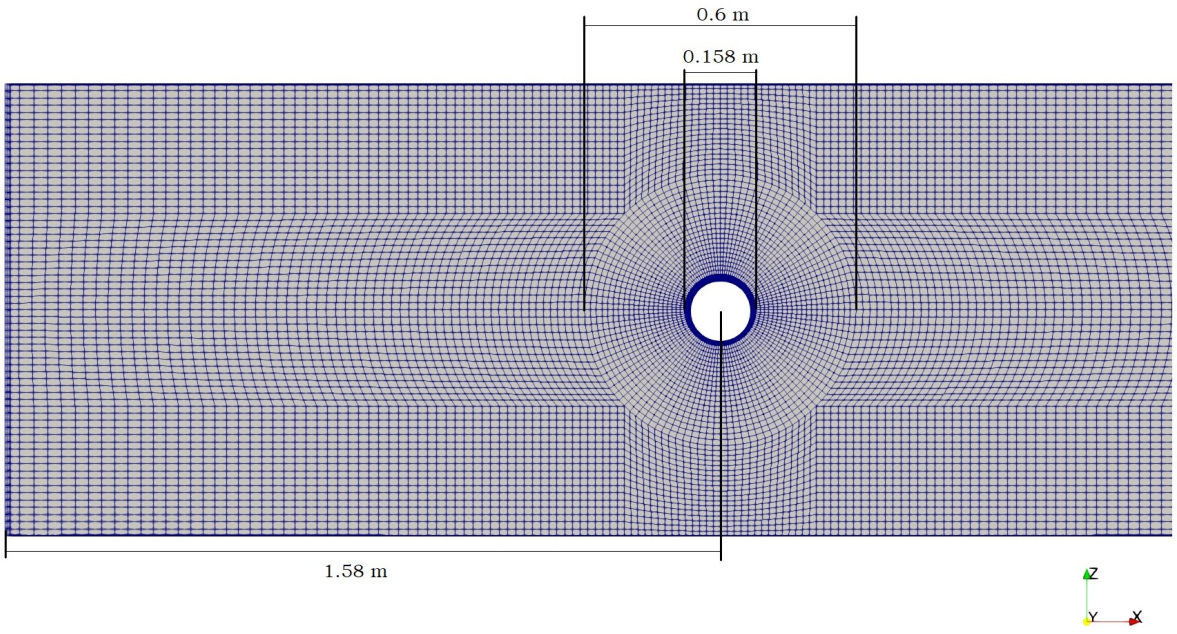

Figure 3.10: Zoomed-in top view of the open channel case with a cylinder

3.2.3. Open channel model including a bed protection layer

The second successive model considers an open channel model with a bed protection layer only. Identical mesh requirements and boundary conditions apply as those stated for the first two models. In this case most effort was put in the extrusion of the bed protection layer. A model of the bed protection layer was obtained from 3D stereo-photography and had a resolution of approximately 0.5 mm. However, due to the cell requirements of the mesh and especially the most limiting requirements near the wall, this resolution

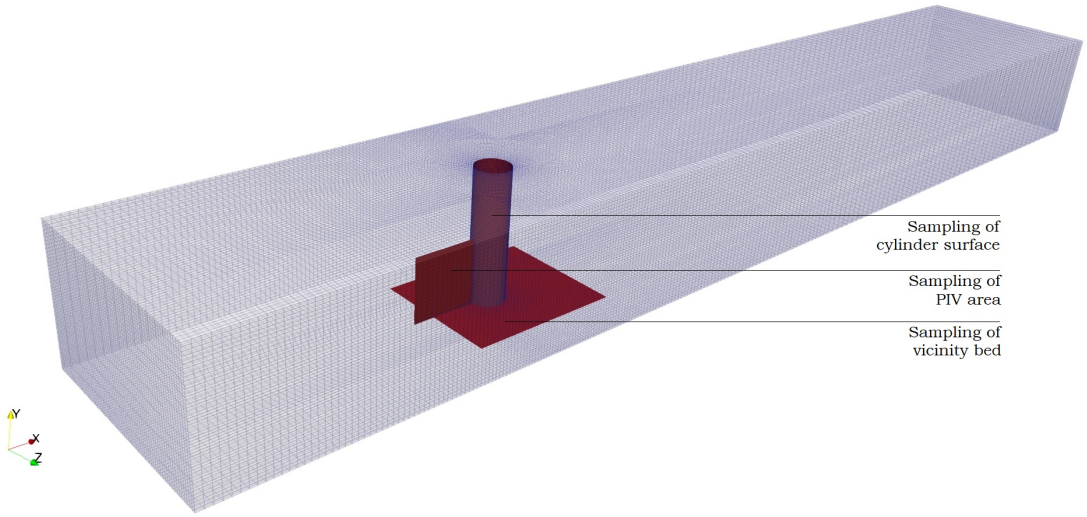

Figure 3.11: Numerical model of the open channel case that includes a smooth cylinder

could not be realised in the numerical model. In fact, most details of the protection layer geometry were not captured due to the resolution difference. Ultimately, the protection layer model was chosen to be smoothed out, removing all information of surface roughness in the model. This was compensated for by the inclusion of an artificial ΔB roughness. The appropriate value of numerical roughness follow from quantities, such as the roughness height and type, that were difficult to determine for the test model. Additionally, there is a numerical roughness present when using the wall function that should be accounted for. Estimation of the roughness parameter ΔB for the bed model by function fitting the log-law through the local boundary layer profile was dubious as the measured boundary layer was still adjusting to the bed surface. Because of this the estimated ΔB of the bed model was considered a reference case and three test simulations were performed with similar roughness conditions. The roughness condition that was found most appropriate with respect to the test observation is further investigated. It is important to note that the real bed protection layer model was porous, but due to uncertainty in the applicability of the porous media models in turbulent flows this feature was not implemented. Instead, the bed protection model was considered a solid geometry. An overview of the mesh can be seen in Figure 3.12. The figure again highlights the regions that are sampled at a frequency of 10 Hz.

3.2.4. Open channel model including both a cylinder and bed protection layer

Finally, a combined study is performed that examines an open channel with a cylinder as well as a bed protection layer. Essentially the numerical model is formed by additional extrusion of the bed protection layer from the open channel case that includes the cylinder. The artificial roughness ΔB for the bed model is used from the previous study that corresponded the most with findings from the experiments. The resulting mesh in visualised in Figure 3.13 and additionally highlighted regions are shown that are sampled with a frequency of 10 Hz.

3.2.5. Boundary conditions of successive models

The successive models had different boundary conditions applied to them then the open channel simulation. This first simulation was initialized with a different strategy and therefore used cyclic boundary conditions. The other cases all used identical boundary conditions, as listed in Table 3.2.5. Note that not every boundary condition was used in each simulation. The cylinder and protection layer boundary conditions are only required if the respective models are actually present in the simulation domain.

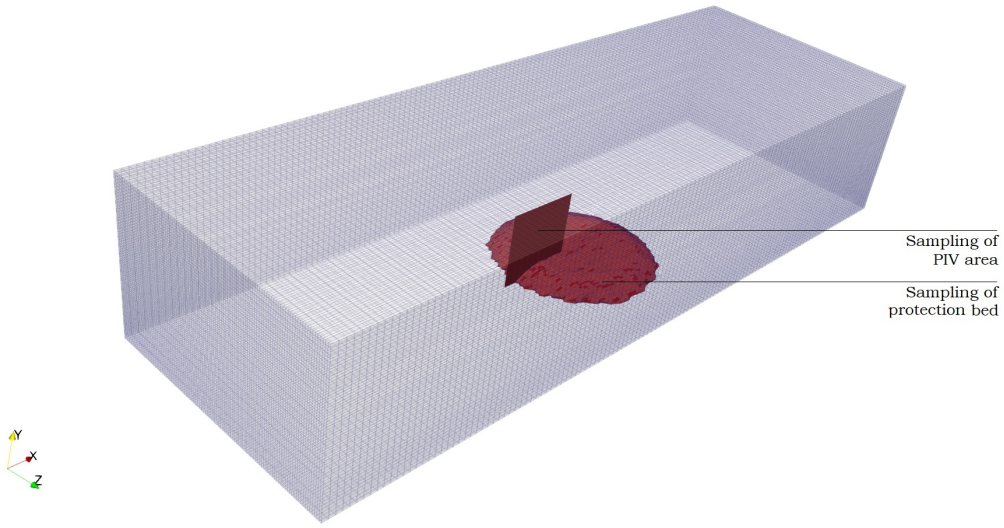

Figure 3.12: Numerical model of the open channel case that includes a smooth cylinder

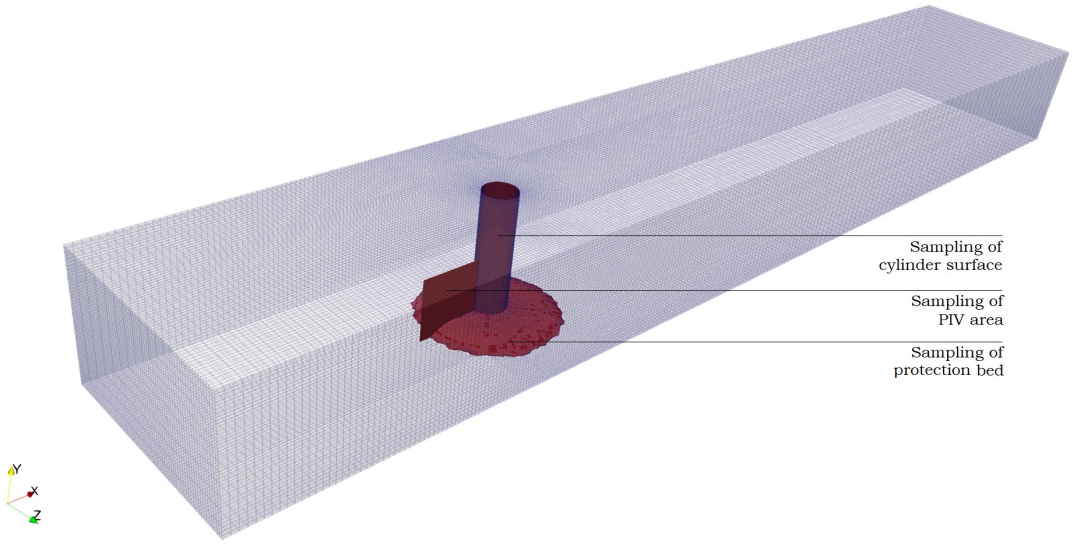

Figure 3.13: Numerical model of the open channel case that includes a smooth cylinder

Table 3.5: Boundary conditions for the numerical cases that include a cylinder and/or a protection layer

Boundary	ν_t [$m^2 s^{-1}$]	$\widetilde{\nu}$ [$m^2 s^{-1}$]	p [$m^2 s^{-2}$]	v [$m s^{-1}$]
inlet	calculated uniform 0	timeVaryingMapped- FixedValue	zeroGradient	timeVaryingMapped- FixedValue
outlet	calculated uniform 0	zeroGradient	fixedValue uniform 0	inletOutlet uniform (0 0 0)
top	zeroGradient	zeroGradient	zeroGradient	slip
bottom	nutURoughWallFunction	fixedValue uniform 0	zeroGradient	noSlip
sides	zeroGradient	zeroGradient	zeroGradient	slip
cylinder	nutURoughWallFunction	fixedValue uniform 0	zeroGradient	noSlip
protectionLayer	nutURoughWallFunction	fixedValue uniform 0	zeroGradient	noSlip

3.2.6. OpenFOAM solver/scheme settings

The following two tables include the discretization settings (Table 3.6) and the solver settings (Table 3.7) that were used for each numerical case.

Table 3.6: Discretization schemes

Type	Parameter	Numerical scheme
Time schemes	ddtSchemes	backward
Gradient schemes	gradSchemes	Gauss linear
Divergence schemes	divSchemes	Gauss LUST Guas limitedLinear 1 Gauss linear
Laplacian schemes	laplacianSchemes	Gauss linear corrected
Interpolation schemes	interpolationSchemes	linear
Surface normal gradient schemes	snGradSchemes	corrected
Wall distance	wallDist	meshWave

Table 3.7: solver parameters

Type	Parameter	Value
Pressure p	solver smoother tolerance	GAMG DIC 1×10^{-6}
Velocity U	solver preconditioner tolerance	PBiCG DILU 1×10^{-6}
Turbulent kinetic energy k	solver preconditioner tolerance	PBiCG DILU 1×10^{-6}

4

Results

In this chapter the results obtained from the simulations are presented in direct comparison with data from the tests or data found in literature. This comparison acts as a validation process to increase the confidence in the accuracy of the simulation results. In addition, simulation results are shown of flow parameters that indicate the initiation of scour and entrainment of granular bed material.

4.1. Open channel simulation

The open channel simulation was mainly performed to see how accurate the flow variables are captured with respect to the test case and whether the statistics of these variables are comparable. In particular, a statistical analysis is performed to review the extreme load conditions. This analyses is based on 5 minutes of sampling time for the experiment case with respect to 40 minutes of duration for the numerical case. This is due to the lack of resolution of the numerical case which is compensated for by a longer and more frequent sampling period. This will be further discussed in the next section.

4.1.1. Velocity profile

The velocity profiles are computed by averaging of the velocity fields in both space and time. The spatial averaging is performed over the streamwise direction, so that the resulting velocity profile depicts the variation of mean velocity over the height of the channel. As stated before, the sample regions of the experimental and numerical cases are approximately of equal size with an area of 300 x 300 mm. The resolution of the experiment data is 1.91 mm in both directions. The limitation of the wall-normal grid spacing in the numerical domains resulted in a resolution of 7.5 mm in vertical direction at the wall, which increases to a value of 5.7 mm in the near wall region and again decreases to a resolution of 8.2 mm far from the wall (see Figure 3.8). The horizontal resolution is a constant 24 mm. The lack in resolution of the numerical case was partially addressed

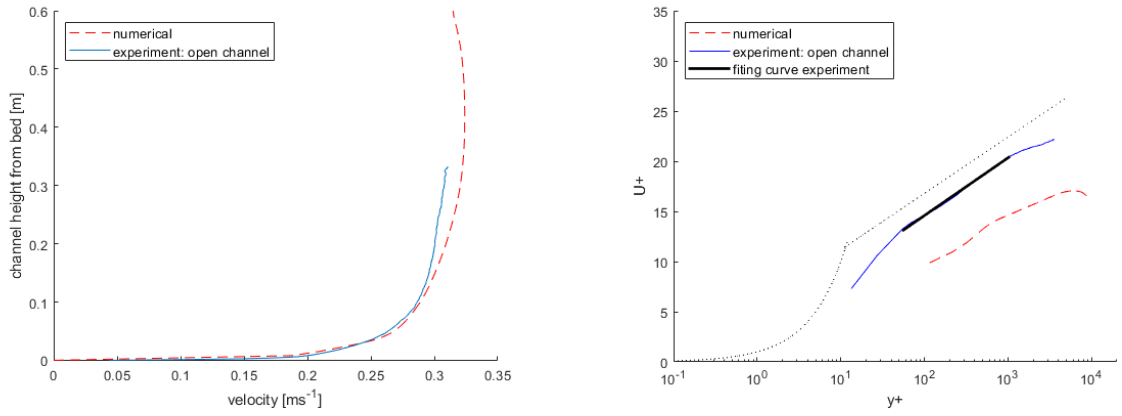

Figure 4.1: Average numerical and experimental velocity profiles of the open channel, dimensional (left) and dimensionless (right)

by increasing the frequency of data sampling. Because of this the region of the numerical case was sampled at 10 Hz, whereas that of the experimental case was sampled at 7 Hz. Both velocity profiles were averaged according to their sampling frequency and are shown in Figure 4.1. As described in the previous chapter, the shape of the simulated velocity profile can be associated with a bottom roughness that is larger than that of the experiment. It is apparent that this results in an overshoot of the mean velocity profile starting at a channel height of approximately 0.1 m. The simulated velocity profile also shows a decline of the mean velocity near the free surface, referred to a *velocity dip*. The location of the maximum velocity from the channel bottom is known as the *velocity-dip-position*. This phenomenon is also observed in practise where maximum mean velocity usually occurs at a distance of 5 to 50 % below the free surface depending on parameters such as the width of the channel, the variation of bed roughness or the bathymetry [23]. The velocity-dip-position of the simulation was located almost 30 % below the free surface. This location could not be identified for the test case due to the limited region that was measured.

4.1.2. Statistical analysis on the flow field

Next, a statistical analysis is performed on the velocity field by comparison of the numerical and test results. This is to gain insight in the ability of the numerical model to predict turbulent features of the flow, which are later used for particle entrainment predictions. The probability density function (PDF) and cumulative density function (CDF) are computed for sub-regions of the sampled area. Each individual region is approximately 300 x 50 mm in size so that in total six regions are investigated with varying heights. The six different sub-regions within the simulated mean streamwise velocity field are depicted in Figure 4.2. However, only the four closest to the bottom are depicted to avoid excessive clustering of data in the figures. The PDF and CDF of the streamwise velocity are provided in Figure 4.3. The distribution are differentiated by the average domain height of each sub-region. It can be seen that the distributions of the simulation and test case are overall in good agreement. Especially the distributions at larger distances from the wall are well predicted by the simulation. The peaks of the PDF's are situated at the correct velocity levels, however the associated probability is mostly over-predicted by the numerical case. An interesting difference between the respective distributions is observed for the region closest to the bottom. In this sub-region the lower range of velocities are being overestimated by the numerical model, while the higher range of velocities are much better in accordance. The velocity statistics of the numerical case do not correspond to a normal distribution, which the numerical model does seem to predict for other sub-regions. This difference is believed to result from the presence of the LES-RANS interface within the first sub-region. Investigation showed that, on average, the interface is located at varying wall-normal distances that range from the second up to the fifth consecutive cell from the wall. Sub-region 1 consists of seven layers of wall-normal cells in total, meaning that the LES-RANS interface resides in the more than half of the total number of cell layers. This corresponds to the disordered distribution of the streamwise velocity of sub-region 1, where a misfit is observed for the lower end of the spectrum that abruptly transitions into a well-behaved distribution that is comparable to the test results. In Table 4.1 a direct comparison is provided between the mean and standard deviation values of the numerical and test results for each of the six sub-regions. It shows that the simulation captures the increasing trend of

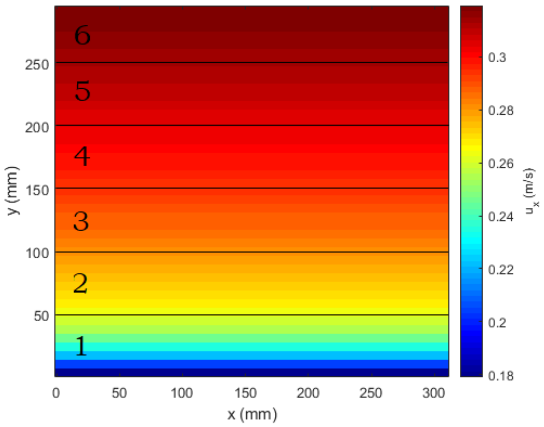

Figure 4.2: Numerically obtained mean streamwise velocity field divided into six sub-regions

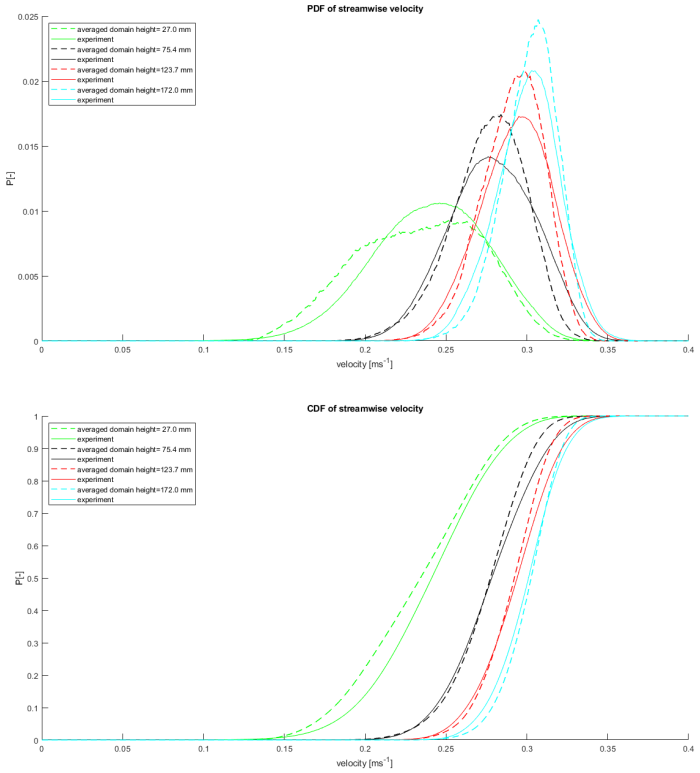

Figure 4.3: PDF (top) and CDF (bottom) of the streamwise velocity component

Table 4.1: Mean and standard deviation values of streamwise velocity component for each sub-region

Sub-region	Simulation		Experiment		Relative difference	
	μ [ms^{-1}]	σ [ms^{-1}]	μ [ms^{-1}]	σ [ms^{-1}]	$\lvert\mu\rvert$ [%]	$\lvert\sigma\rvert$ [%]
1	0.2346	0.0265	0.2384	0.0291	1.584	8.995
2	0.2778	0.0226	0.2787	0.0262	0.306	13.637
3	0.2933	0.0191	0.2933	0.0227	0.013	15.523
4	0.3039	0.0168	0.3001	0.0200	1.265	15.850
5	0.3117	0.0144	0.3038	0.0188	2.579	23.311
6	0.3179	0.0124	0.3066	0.0181	3.689	31.200

the mean values and the decreasing trend of the function spreading as the sub-region distance from the wall increases. The maximum peak value of the mean fluctuating component was located in the top section of sub-region 1, which was comparable to that observed of the test.

Besides the streamwise component, also the wall-normal velocity component is considered for the statistical analysis. The associated PDF's and CDF's are computed for identical sub-regions as described before and they are shown in Figure 4.4. Because in this figure the distribution are even more clustered, only three sub-regions are depicted that are closest to the bottom of the channel since these are most of interest. A large discrepancy is seen again for the lowest sub-region where the numerical case inaccurately captures the spreading of the flow velocity. This results in a substantial overestimation of the peak occurrence of velocities near 0 m/s. The location of this peak occurrence is predicted well in comparison with the other sub-regions. Contrarily, The distributions of the other sub-regions are more comparable in terms of their spreading. The numerically obtained PDF's do approach the apparent normal distribution shape of the test case PDF's. In Table 4.2 again a comparison is provided between the mean and standard deviation values of the numerical and test results for the sub-regions. The mean values of the simulation case are relatively small values with respect to the test data so that the relative mean values are nonsensical and have been left out. The mean values of the test case can be seen increasing for larger sub-region distances from the wall. This is possibly

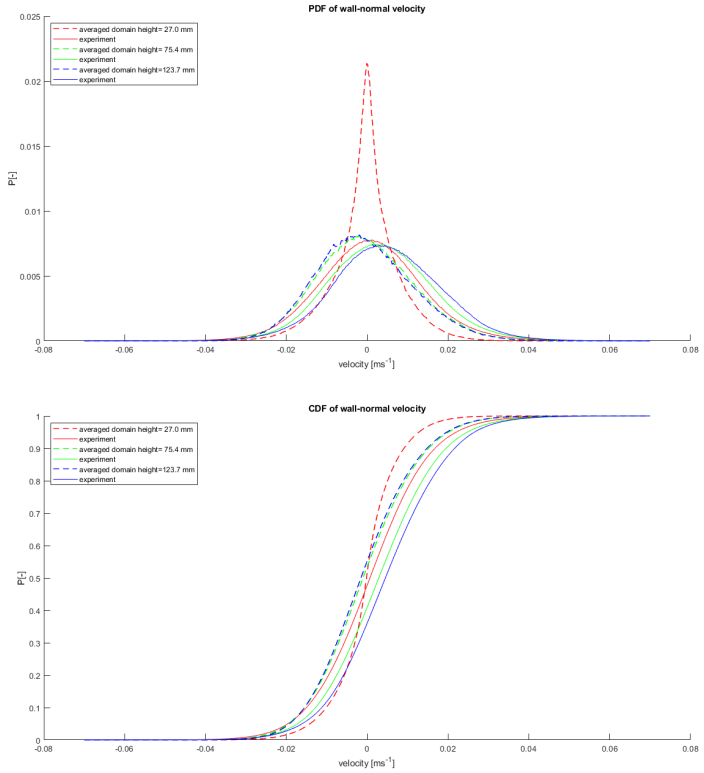

Figure 4.4: PDF (top) and CDF (bottom) of the wall-normal velocity component

Table 4.2: Mean and standard deviation values of wall-normal velocity component for each sub-region

Sub-region	Simulation		Experiment		Relative difference	
	μ [ms^{-1}]	σ [ms^{-1}]	μ [ms^{-1}]	σ [ms^{-1}]	$\lvert\mu\rvert$ [%]	$\lvert\sigma\rvert$ [%]
1	1.2994×10^{-5}	0.0073	0.0010	0.0126	-	42.373
2	-5.0864×10^{-4}	0.0121	0.0034	0.0130	-	7.081
3	-9.7501×10^{-4}	0.0119	0.0050	0.0131	-	9.638
4	-1.2316×10^{-3}	0.0112	0.0056	0.0134	-	16.403
5	-1.3811×10^{-3}	0.01033	0.0057	0.0137	-	24.562
6	-1.6112×10^{-3}	0.0094	0.0054	0.0138	-	31.724

explained by the presence of the boat upstream of the test models that obstructs the incoming flow field as described in Section 2.6.1. The positive mean values represent a net upwards flow due to recirculation of flow at the backside of the boat. Interestingly, the behaviour of the trend of the standard deviations for greater wall distances is opposite for the numerical case than it is for the test case. The exact reason for this is unknown, but might also be related to the fluid-boat interaction.

The last component is the spanwise velocity of which the PDF's and CDF's are provided in Figure 4.5. Here also the functions of only the three sub-regions closest to the bottom are presented to avoid clustering of the data. The numerical model is able to predict comparable velocity distributions as those obtained from the test measurement, however there is a consistent tendency to underestimate the spreading of the distributions and overestimate the peak occurrences of velocities near 0 m/s. The mean and standard deviation values are given in Table 4.3. For the same reason as mentioned earlier, the relative difference of the mean variable is nonsensical and therefore chosen to be excluded. For the most part the behaviour regarding the distribution spreading is appropriately captured as it decreases with increasing wall distances. However, the reduction of the spreading is overpredicted in the numerical simulation so that the error margin increases at greater wall-normal distances. This can also be seen by the increasing nature of the relative standard deviation differences.

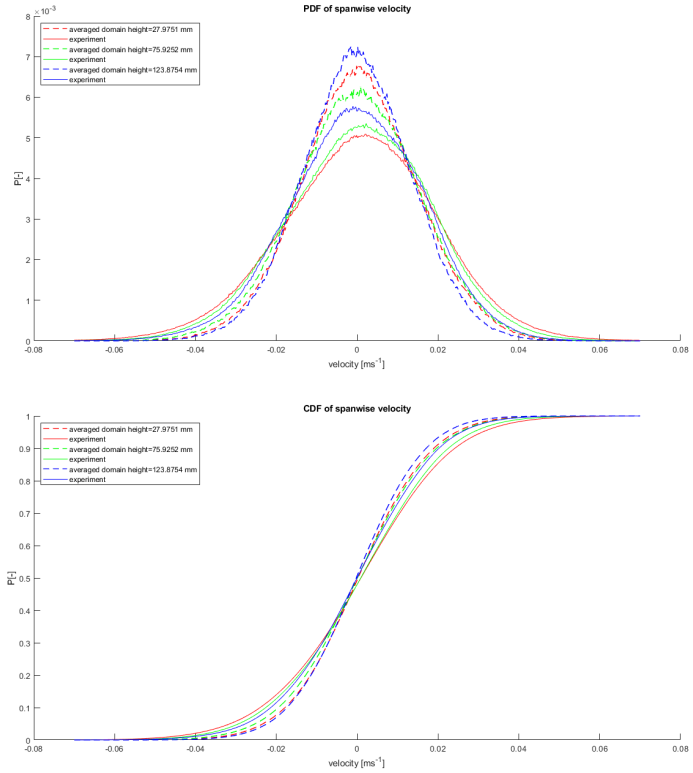

Figure 4.5: PDF (top) and CDF (bottom) of the spanwise velocity component

Table 4.3: Mean and standard deviation values of spanwise velocity component for each sub-region

Sub-region	Simulation		Experiment		Relative difference	
	μ [ms^{-1}]	σ [ms^{-1}]	μ [ms^{-1}]	σ [ms^{-1}]	$\lvert\mu\rvert$ [%]	$\lvert\sigma\rvert$ [%]
1	-4.1773×10^{-4}	0.0144	7.7053×10^{-4}	0.0195	-	26.226
2	7.0599×10^{-5}	0.0154	8.9558×10^{-4}	0.0182	-	15.336
3	1.2114×10^{-4}	0.0135	4.6975×10^{-4}	0.0170	-	20.582
4	-1.3532×10^{-4}	0.0120	-7.4452×10^{-4}	0.0164	-	26.802
5	-1.4748×10^{-4}	0.0106	-0.0017	0.0160	-	33.869
6	-1.7872×10^{-4}	0.0094	-0.0021	0.0157	-	40.069

By inspection of the data it is stated that the mean component is well predicted for each of the velocity components. The accuracy of the spreading of the distributions differs for each of the velocity components, but generally ranges from 10 % to 40 % within the inspected flow area. It is stressed that the most critical region is believed to be sub-region 1 due to the presence of LES-RANS interfaces within this region that is found to result in unphysical flow statistics.

4.1.3. Turbulent kinetic energy spectra comparison

Finally, the turbulent behaviour is inspected by means of turbulent kinetic energy (TKE) spectra. Energy functions $E(k)$ along both the streamwise and spanwise directions of the whole flow field are generated from the corresponding velocity fluctuations in those directions. This allows for a better interpretation of the turbulent behaviour when investigating the separate fluctuation components. It should be noted that only the resolved turbulent fluctuations are included in the calculation of the TKE. The parameters of interest are the large-scale structures in the flow as they contain more energy and govern the initiation of particle entrainment. Those large-scale structures are resolved by the IDDES model down until scales the size of bed particles, whereas the small-scale structures are modelled instead. The primary interest is therefore to observe the resolved TKE. It is also mentioned that no normalization is applied to the resulting function. This is

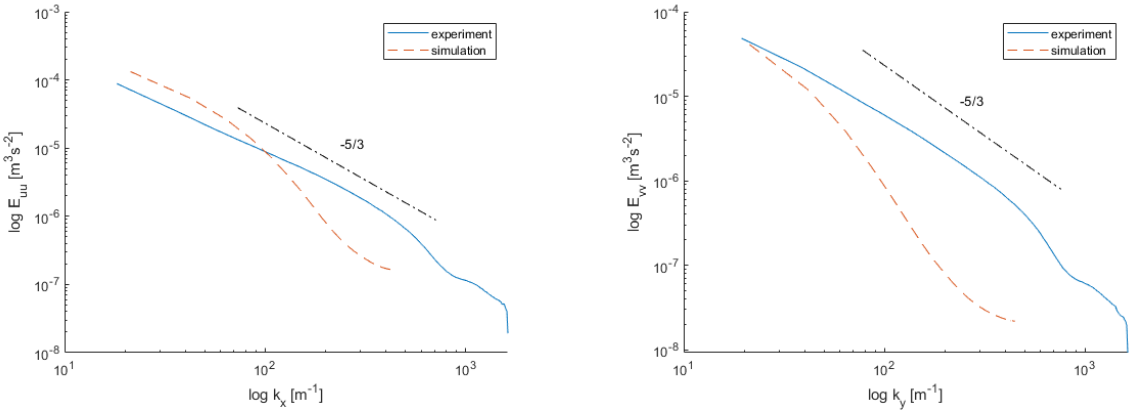

Figure 4.6: Turbulent kinetic energy functions $E_{uu}(k_x)$ (left) and $E_{vv}(k_y)$ (right)

because the normalization depends on ${u_\tau}^2$ which has been shown to differ significantly between the numerical and test case. This would make the comparison unnecessarily difficult, especially since similar situations are being viewed. The energy functions are generated for every sample frame and ultimately averaged so that a time averaging process is applied. Both streamwise and wall-normal spectra are shown in Figure 4.6. In addition to the energy functions, a reference function is plotted with a slope proportional to $k^{-5/3}$ which is characteristic for the inertial subrange of a turbulent flow. The figure shows that the energy functions from measurement data do indeed have a similar slope to that of the reference slope of $k^{-5/3}$ over a large range of wave numbers. This is expected since it is beforehand known that the observed flow was turbulent. The simulated energy function $E_{uu}(k_x)$ shown in the left figure gives an overestimation of the TKE for lower wave numbers with respects to the spectra obtained from test measurements. At approximately $k_x = 100\ m^{-1}$ the function starts to increasingly underpredict the TKE levels in comparison with the test case. This is partly due to the function only expressing the resolved part of the TKE. The IDDES model also includes modelled TKE that, if depicted, will influence the function at higher wave numbers. Since this part is excluded an underprection of the TKE levels is observed. The figure right shows the simulated energy function $E_{vv}(k_y)$ which is very similar in shape to that of $E_{uu}(k_x)$. However, in this case the simulation continuously underestimates the TKE with respect to that of the test case. The best correspondence is again found for lower wave numbers. For a small section of the depicted energy function the reference slope of $k^{-5/3}$ is well approximated by the numerical case.

4.2. Open channel simulation including a cylinder

Next, the results of the open channel with the integration of a cylinder are investigated. In this case several new methods are used to validate the obtained numerical results that include the drag, lift and pressure coefficient around the cylinder. Then the model is used to predict scour inducing variable fields around the cylinder. First, to get a general idea of the flow field and the numerical accuracy, a visual comparison is performed. Here the mean streamwise velocity component of the flow field are compared between the numerical and test cases upstream of the cylinder (see Figure 3.11). Contours of the mean streamwise velocity component are depicted in Figure 4.7. It is noted that missing data is shown as a black region. Identical colorbar ranges are used to allow for direct comparison of the velocity levels. The simulated velocity plane is seen to correspond well to the measured flow field. A few remarks are given regarding the general flow structure. First, the velocity overshoot can clearly be observed when considering the incoming flow. In particular the velocities far from the wall are overestimated. When approaching the cylinder wall the flow deacceleration is captured quite well when looking at the general shapes of the contour lines. Also the distance from the cylinder wall at which the flow deacceleration becomes significant is appropriately predicted by the simulation model. However, a substantial difference is observed close to the cylinder-bed junction. Here the simulated velocity field shows an excessive backflow where the measured flow field shows a stagnation region. It is this region where the initiation of upstream scour begins due to the formation of horseshoe vortices. The numerical results thus misrepresent the flow phenomena close to the cylinder-bed junction to a certain degree. A possible explanation for this observation is the presence of a velocity overshoot that results in a negative pressure gradient towards the cylinder that is greater than in the test case. This then results in a greater mean

downwards flow velocity and ultimately a greater backflow as this reaches the cylinder-bed junction. Secondly, the issue could be attributed to the invalidity of wall functions in regions of separated flow. Near the cylinder-bed junction the flow in known to separate from the bed due to interaction with incoming boundary flow. The local flow profile does not correspond to a boundary layer with a logarithmic sub-layer, which is a characteristic that the formulation of the wall function is based on. For this specific region the wall functions are thus not applicable, resulting in unphysical flow behaviour.

4.2.1. force coefficient validation

Next, a validation process is performed based on the drag, lift and pressure coefficients of the cylinder. In literature many experiment have been performed on flows around a cylinder that show a dependence of these force coefficients on the Reynolds number. These results will be used to check the validity of the numerical case. It is mentioned that the simulated case is not fully representative of experimental cases found in literature. The case differs in that the bottom wall contains a numerical roughness and so does the cylinder wall, which are varying unknown quantities based on the local wall shear stress. Also the simulation considers a small channel which impacts the flow upstream and downstream of the cylinder. Both aspects can affect the resulting force coefficients in comparison with a free flow condition. Therefore small deviations are expected in the comparison. The goal is to obtain results that approximate the validation cases so that the numerical case can reliably be used to estimate entrainment indicators. The considered Reynolds number is 3.6×10^4 based on the cylinder diameter.

The drag and pressure coefficients are given in Figure 4.8. The drag coefficient C_D is shown as a time series over the duration of the simulation. Note that an initial period is not accounted for to allow the appropriate flow field of the simulation to establish. The resulting mean is computed by averaging over the time series, resulting in a mean drag coefficient of C_d = 1.23. Referring to Figure 2.8, this result approximates the drag coefficient function with a small surface roughness. This result can be explained by the fact that wall functions were used as boundary conditions for the cylinder surface. Therefore a numerical roughness can be expected for the cylinder walls. White [54] includes the effect of the cylinder length-to-diameter ratio $\frac{L}{D}$ as well. For a $\frac{L}{D}$ ratio of nearly 4, which corresponds to the cylinder in the numerical model, it is shown that the drag coefficient is approximately 0.73. This value increases towards a value of 1.20 for increasing $\frac{L}{D}$ ratios. This difference is most likely observed due to the cylinder not being completely submerged in the water, but it reaching the bottom and top boundaries of the domain. In combination with the symmetrical plane at the top boundary it is as if the cylinder is sufficiently long that no overflow at both cylinder ends is simulated. This is thought to severely influence the perceived $\frac{L}{D}$ ratio and ultimately the drag coefficient as if a long cylinder case is simulated.

The pressure coefficient C_p is briefly discussed in Section 2.4.4 and the reference validation diagram is given in Figure 2.9. The presented C_p function in Figure 4.8 is obtained by averaging the pressure coefficient values on the cylinder wall over the height of the cylinder as well as over time. The low C_p values near the bottom are neglected as inclusion of these would skew the resulting function. The stagnation pressure coefficient is slightly higher than one which is the result of an underestimation of the local maximum velocity used for normalisation. In comparison with the reference diagram the location and associated C_p value of the func-

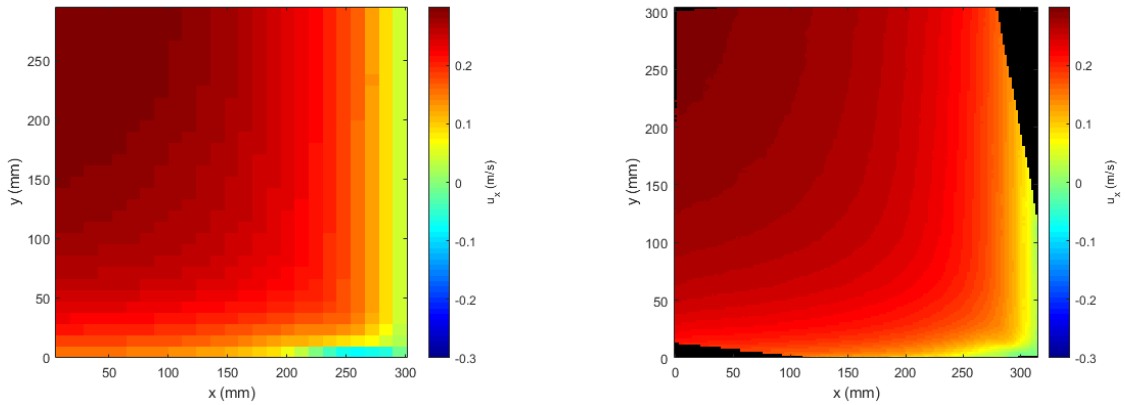

Figure 4.7: Mean streamwise flow field near the cylinder-bed junction from the simulation (left) and test measurements (right)

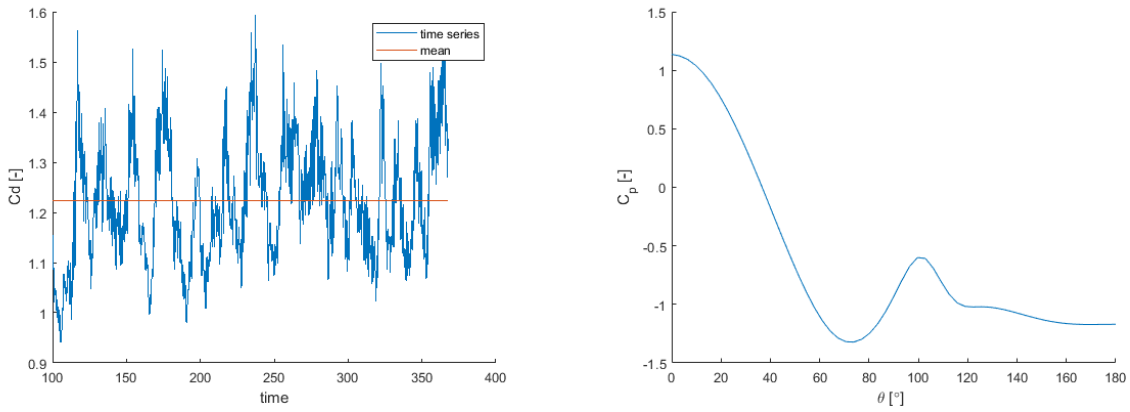

Figure 4.8: Numerically obtained drag (left) and pressure (right) coeffients

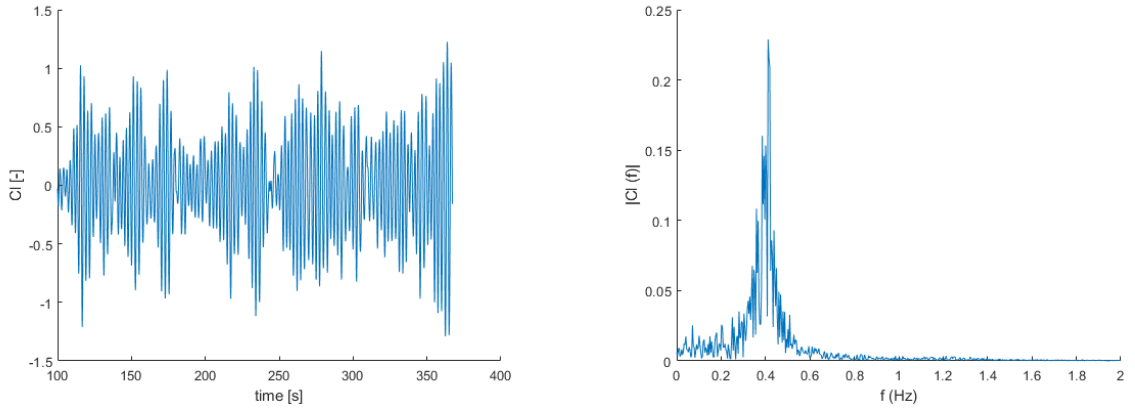

Figure 4.9: Lift coefficient time series (left) and the Fast Fourier analysis (right)

tion minimum are considered, which are found to be approximately θ = 72 ° and C_p = -1.32. This corresponds well to the pressure coefficient function in the reference diagram with an associated with a Reynolds number of 3.6×10^4. The peak found at θ = 100 deg with C_p = -0.6 is overestimated with respect to the validation diagram. In fact, the pressure coefficient functions do not show a distinct peak such as the numerically obtained pressure coefficient function. This behaviour indicates that the IDDES model has difficulties in accurately capturing the flow mechanism at locations of flow separation.

The last validation coefficient is the lift coefficient C_L. The corresponding validation parameter is the Strouhal number as discussed in Section 2.4.5. In Figure 4.9 the lift coefficient time series is shown left. The fluctuations show unsteady behaviour due to the incoming turbulent flow. To estimate the governing vortex shedding frequency, the Fast Fourier transform was applied to the time series as shown in the right figure. A peak vortex shedding frequency of 0.41 Hertz was found resulting in a Strouhal number of 0.22. Reference Figure 2.10 shows that this corresponds to a Strouhal number with the largest presented roughness ratio k/D.

By consideration of the obtained numerical results in comparison with values found in literature it is found that the numerical model is able to predict the force coefficients well. However, the results do somewhat correspond to a cylinder surface that is rough. This additionally confirms the presence of a numerical roughness when wall functions are used as described in Section 3.1.

4.2.2. Wall shear stress evaluation

This next section is dedicated to the wall shear stress prediction of OpenFOAM. The goal is to see how well the statistic of the wall shear stress are predicted, which is of interest because it is one of the main parameters that is responsible for the phenomenon of scour. A statistical analyses is considered because the extreme load conditions on the bed are most likely to result in entrainment of sediment. In Section 3.1 it was found that the

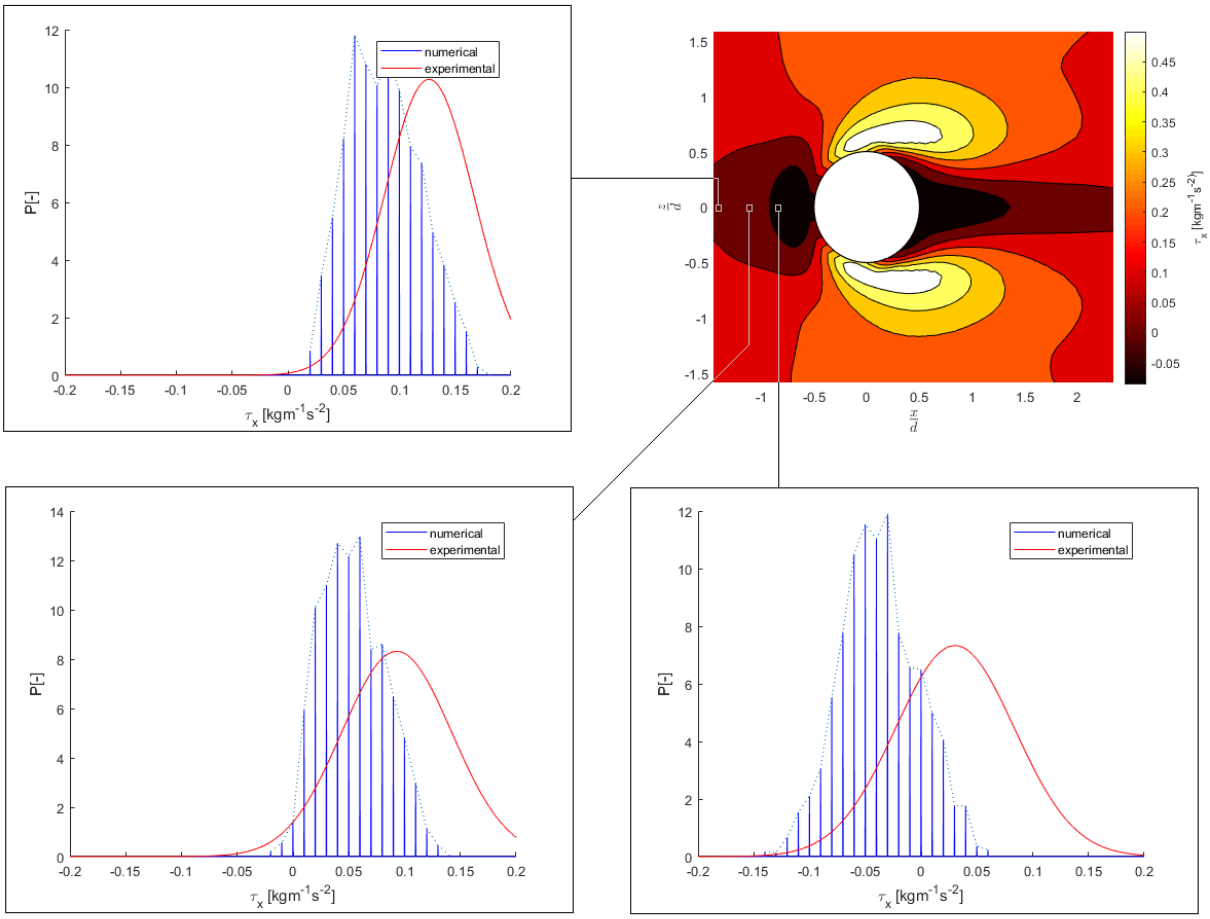

Figure 4.10: Top view of the cylinder displaying the magnitude of the wall shear stress. A statistical analysis is performed for three location upstream of the cylinder

friction velocity is inaccurately estimated due to a linearisation error in OpenFOAM. The friction velocity is closely related to the wall shear stress by its definition, $u_\tau = \sqrt{\tau_w/\rho}$. It is therefore expected that a difference is observed between the wall shear stress of the numerical and experiment case. This analysis tries to expand this knowledge by showing the extend of the error. The wall shear stress surrounding the cylinder is shown in Figure 4.10. For three locations upstream of the cylinder a comparison is shown regarding the streamwise component of the wall shear stress. In general, the measured PDF's all are similar in terms of their shape and location. They show symmetrical behaviour with respect to the origin. In contrast, the numerically estimated PDF's contains more spreading than the measured PDF's and they are shifted different distances with respect to the origin. The overall shape of the distributions remain similar at the different locations. The shift seems to be dependent on the cylinder distance, with increasing positive shift to the right for smaller cylinder distances. This can be associated with the gradient of the decreasing flow velocity towards the cylinder over the excessive backflow near cylinder-bed junction. The distributions at these specific locations show that the extreme absolute value of the streamwise component of the wall shear stress is 2 to 3 times larger for the numerical case than the test case. However, this depends on the trend of the shift and requires further investigation. It is restated that only one component of the wall shear stress is discussed here and no claims can be made regarding the magnitude of the wall shear stress.

4.2.3. Scour indicator parameters

Using the numerical model the scour indicator parameters, which are discussed in section 2.5.2, are computed at the bottom wall in the vicinity of the cylinder. They include the wall shear stress, wall pressure and their fluctuating component in addition to the pressure gradients in streamwise and spanwise directions. To

visualize the obtained stability fields, the standard deviation is considered to represent the severity of fluctuations at a given locations. This assumption alters the stability formula of Equation 2.82 to the following one:

$$\Psi = \frac{(\alpha_1 \widetilde{\overline{\tau_w}} + \alpha_2 \sigma(\widetilde{\tau_w}) + \alpha_3 \widetilde{\nabla \overline{p}} + \alpha_4 \sigma(p))_{max}}{(\rho_s - \rho_w) g d_s} \tag{4.1}$$

Where σ denotes the standard deviation of a specific variable. The assumption to considered the standard deviation is not entirely correct as it provides a measure of spreading, which does not necessarily indicate that it is associated with the extreme fluctuations found within the numerical domain. However, the occurrence of an extreme fluctuation is not only of importance for entrainment. The displacement of a particle also depends on the duration of an applied force and its frequency. Because of this it is opted not to considered the observed extreme values, but the spreading of the fluctuations instead. Each of the terms of Equation 4.1 represents one of the indicator parameters and the contribution to the stability parameter is altered with the alpha constants. For this analysis the individual fields are only inspected and an assessment is made based on test measurements. It is restated that no fitting of the alpha constants is performed due to absence of test data on damage patterns. Top views of normalized indicator fields around the cylinder are presented in Figure 4.11. The normalization is based on a reference value far upstream of the cylinder. Additionally, the axis system has been normalized with the diameter of the cylinder.

The drag component D_{ind} of the hydrodynamic forcing is indicated by the magnitude of the wall shear stress. This field shows relatively low values of shear stress in the stagnation region in front of the cylinder. From this point, as the flow start to accelerate around the cylinder, the shear stress values are seen to increase

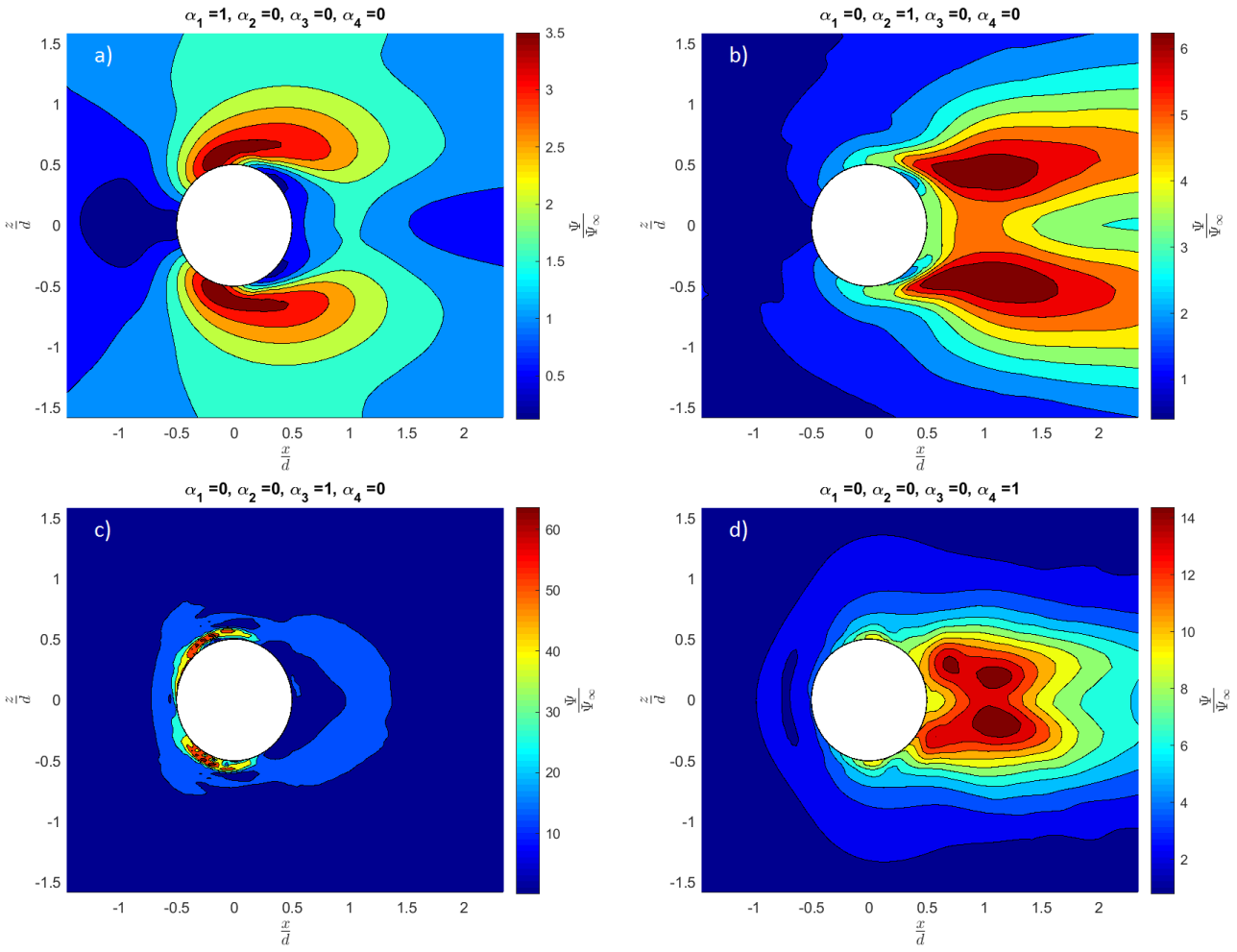

Figure 4.11: Top view of indicator D_{ind} defined by wall shear stress (a), indicator D'_{ind} defined by wall shear stress fluctuations (b), indicator H_{ind} defined by pressure gradients (c) and indicator L'_{ind} defined by pressure fluctuations (d) around a cylinder

in a rapid fashion up to a maximum value at approximately 75 deg about the cylinder. This location seems to coincide with the minimum of the pressure coefficient function shown right in Figure 4.8. This is in accordance with Bernoulli's principle where in general high flow velocity are accompanied with low flow pressure values. From this location the shear stress values decrease relatively slowly downstream of the cylinder. In this case the region with high shear stresses are considered potential entrainment locations due to drag.

The drag force fluctuations D'_{ind} are indicated with the wall shear stress fluctuations, visualized with the standard deviation of this parameter. In contrast to the region that was assumed dominated by the drag D_{ind}, this field reaches its highest values downstream of the cylinder. This is due to the highly distorted velocity field in the wake of the cylinder as flow separates from the cylinder surface. A relatively large domain is highlighted, that stretches to more then two cylinder diameters downstream of the cylinder, where prominent stability values are observed. It is interesting to notice that the largest stability values of indicator fields D_{ind} and D'_{ind} live in distinctly different regions.

An indicator of both lift and drag components was depicted by the hybrid indicator H_{ind}, which includes the horizontal and spanwise pressure gradient projection onto the bed model. These components were mentioned as hybrid candidates for both lift and drag forces. In the stability formula the projection of the pressure gradient parameters onto the bed is considered with the use of Pythagoras' equation. The field depict large pressure gradients close the cylinder wall, primarily towards the front side of the cylinder. The most prominent values are found in the region where also the wall shear stress values were highest. It is noticed that a large spreading of stability values is observed for this field that quickly differ in severity.

Finally, the indicator for lift fluctuations L'_{ind} is the local pressure fluctuation and it as well is suggestive of a prominent region of lift-induced entrainment behind the cylinder. The region approximates a size similar to that of the cylinder itself and reaches downstream of the cylinder. This is again explained by the turbulent flow behaviour in the wakes of the cylinder. As a result, the region where the largest stability values are found for L'_{ind} are vastly different than that of hybrid indicator H_{ind}. The same observation was made previously for indicator fields D_{ind} and D'_{ind} so that the statement is made that mean flow parameter indicators primarily highlight regions upstream and to the side of the cylinder, whereas turbulent parameter indicators mostly highlight regions downstream of the cylinder.

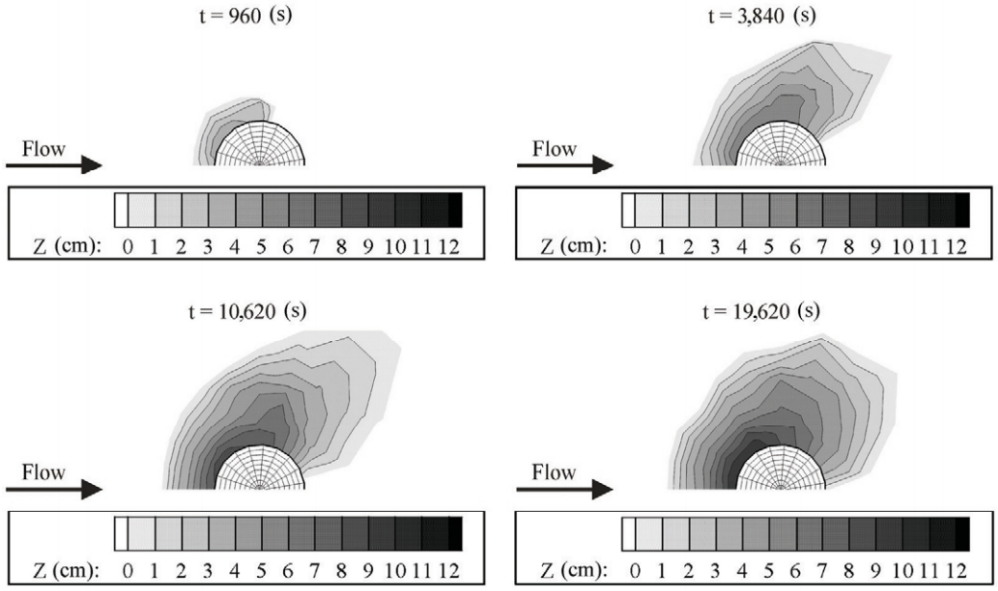

Figure 4.12: Initial scour depth patterns in azimuthal half-planes for different time steps, adopted from Link et al. [25]

With this the dominant drag- and lift-induced entrainment regions are estimated for turbulent flow around a cylinder. A most probable region of particle displacement is than estimated by the overlapping prominent indicator regions, as it is expected that here the extreme field stability values are found. However, the contribution of each indicator is unknown. Therefore the indicator fields are compared to a test case with similar dimensions so to investigate the scour patterns in relation to the prominent regions of the indicators. Link et al. [25] studied the formation of a scour over time for a cylinder with a diameter of 0.2 m inside a 26 m long, 2 m wide and 1 m deep flume with a mean flow velocity of 0.247 m/s. The water depth was 0.3 m. Assuming

an identical water viscosity as that during the flume tests in the Hydro Hall, an similar Reynolds number Re_D of 0.4×10^5 is calculated for the study case. Because of this it is assumed that the scour pattern is representative of one that could be observed for the simulated case. Findings of Link et al. are depicted in Figure 4.12 that show the formation of a scour hole around a cylinder during its early stages. The figure shows the initiation of scour at the front side of the cylinder. This region is most accurately captured by indicators D_{ind}, H_{ind} and V_{ind}, while only limited displayed in L'_{ind} and D'_{ind}. The evaluation of the scour hole shows further growth to the sides and eventually to the back of the cylinder. This process is well in line with the pattern of indicator D_{ind}. This indicates that the bed particle entrainment is dominated by drag and pressure gradient indicators during the initial formation of scour holes. It is noted however, that the difference in channel width is expected to affect the evaluation of scour formation. This is due to the cylinder contributing to an increased blockage ratio of the flume when considering a smaller channel width. This ultimately affects the pressure and flow fields upstream and downstream of the cylinder. The difference in scour formation, however, is expected to limited so that the general observations of the study by Link et al. still apply for analyses of the numerical case.

4.3. Open channel simulation including a protection layer

Next the results of the numerical model that includes only the protection layer are discussed. First simulations are performed to obtain a better estimate of the bed model roughness. This is investigated by comparison of velocity fields and local velocity profiles. The roughness parameter K_s that is best in agreement with test results will be used for the assessment of initial bed particle entrainment. This will be done in comparison with results of the smooth bed model so to analyse the effects of bed roughness on the entrainment indicators. No reference data for damage pattern were found so that the indicator fields are only individually assessed.

4.3.1. Effect of bed model roughness

Due to uncertainties in the roughness parameters of the bed model, three simulations have been performed with varying bed roughnesses. With the use of function fitting of the log-law through the local boundary layer profile an estimation of the bed roughness ΔB was made. An associated roughness height K_s of approximately 20 mm was found. This value is higher then the size of the bed particles of the test bed model, which were approximately 5 mm, and therefore two additional simulations were run with smaller K_s values of 10 mm and 5 mm. The last two mentioned simulation cases showed promising results and will be discussed together with a smooth bed simulation case to analyse the effects of bed surface roughness on the velocity field. The streamwise component of the mean velocity fields are visually compared in contour plots shown in Table 4.4. The fields have been mapped to an identical grid by linear interpolation so to allow for the creation of difference plots. It is mentioned that the averaging process is based on obtained results from a total simulation time of 500 seconds due to the expensiveness of the *timeVaryingMappedFixedValue* boundary condition at the inlet. The numerically obtained fields depict an incoming flow field that reaches higher velocities in the top region of the domain than found in the experiment case. This again can be attributed to the velocity overshoot that was apparent in the simulated velocity profile. In relation, the contour plots in the lower regions of the incoming boundary flow are better approximated. Each of the simulations depict similar flow acceleration behaviour along the slope of the bed, which are comparable to that of the test case. By looking at the difference plots, a consistent overestimation of the velocity along the slope of the bed is predicted in the order of 0.05 m/s. The simulation models show distinct boundary layer developments after flattening of the bed model. The smooth bed model suggests a more rapid redevelopment of the boundary layer that is accommodated with relatively high velocity values in comparison with the test case. By increase of the bed model roughness to K_s = 5 mm and K_s = 10 mm, the velocity distribution of the boundary layer is altered, with incremental reduction of the near-wall flow velocities towards zero as the bed roughness increases. This observation can also be seen in Figure 3.2 where velocity profiles for different bottom roughnesses are depicted. Inspection of the difference plots shows that the near-bed velocities are better predicted when considering a bed roughness height of K_s = 10 mm. This is emphasized in Figure 4.13 where the mean streamwise velocity profiles of the test and numerical cases are compared for specific bed locations. Here it can be seen that the velocity profiles of the numerical cases are all very similar for locations x = 0.05 m and x = 0.10 m as the duration of the fluid-bed interactions is still limited at this point. From here the divergence of the velocity profiles becomes clear when viewing the predicted near-bed velocities. The largest differences with experiment results are consistently given by the simulation that includes a smooth bed model. As claimed before, the best

Table 4.4: Comparison of the streamwise velocity component between the experiment results and three numerical cases that differ in bed roughness. K_s values of 0 mm (top), 5 mm (middle) and 10 mm (bottom) are considered

Experiment	Simulation	Difference
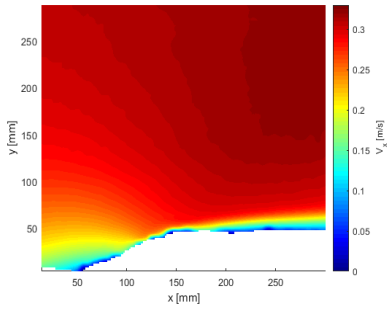	K_s = 0 mm 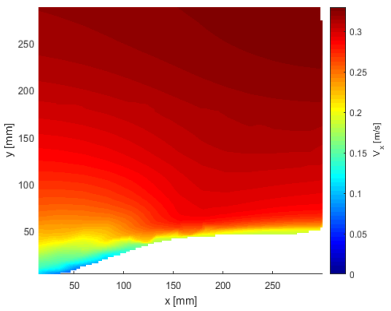	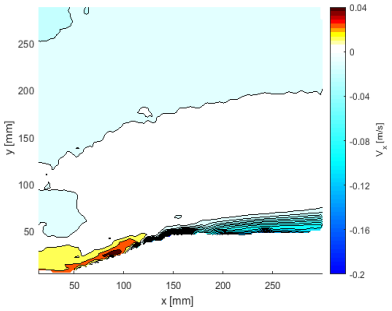
	K_s = 5 mm 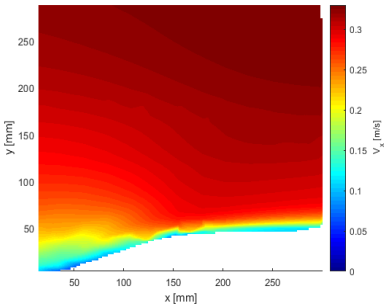	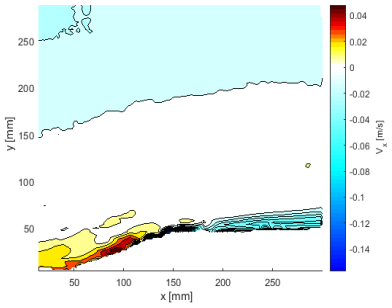
	K_s = 10 mm 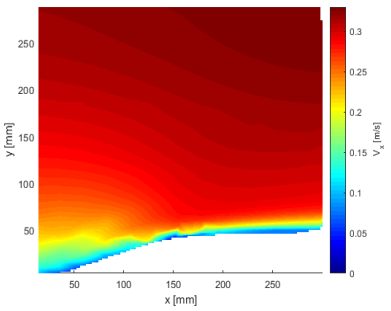	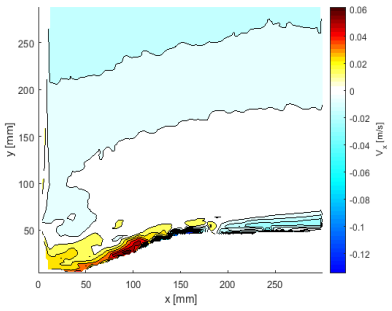

correspondence for the near-bed velocities is found with a bed model roughness of K_s = 10 mm. However, the ambient velocities are slightly better estimated with a bed model roughness of K_s = 5 mm. Because flow predictions near the surface of the bed are most of interest for this study, the model with a roughness height K_s = 10 mm is considered for the entrainment analysis.

4.3.2. Wall shear stress evaluation

In the next section the wall shear stress prediction of the simulation is again investigated. In particular, the statistics of this variable are considered as it is used in the particle entrainment analysis. The wall shear stress over the bed model is shown in Figure 4.14. For three locations along the bed surface the statistics of the streamwise component of the wall shear stress along the bed are compared between the numerical and test cases. A smooth bed model and a rough bed model simulation case has been included to asses the effects of surface roughness. In contrast to the wall shear stress comparison for the cylinder model, a significant difference is observed when a bed model is included in the domain. During the initial fluid-bed interaction the difference is limited when considered a smooth bed model. However, at greater distances along the slope the misfit is very apparent. This is issue amplified when a rough bed model is considered, where both the spreading and the mean component of the wall shear stress are severely overpredicted. The reason for this

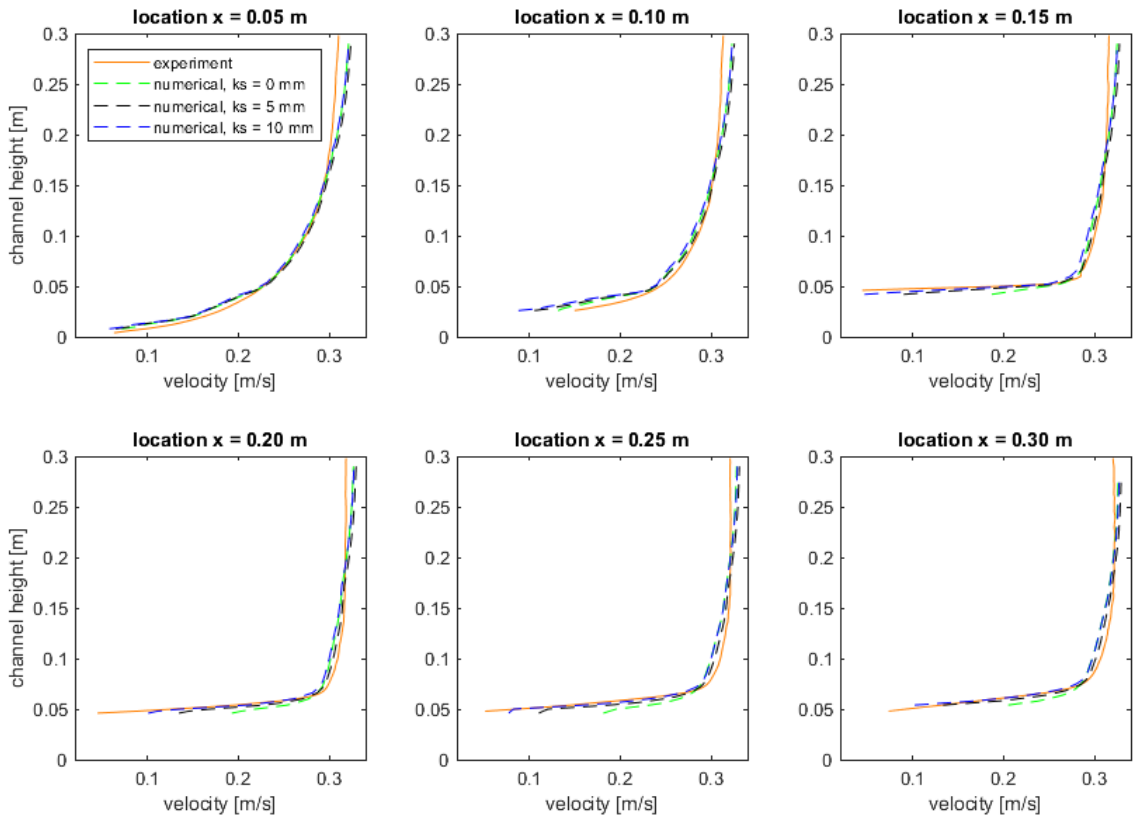

Figure 4.13: Mean streamwise velocity profile comparison at different bed locations

behaviour is unexpected as the velocity profiles in Figure 4.13 show comparable velocity profiles close to the bed. There are a number of possible reasons listed for the observed misfit.

- Discrepancies in near-bed flow behaviour are expected due to the wall functions that introduce a numerical roughness. The extend of this roughness is unknown as the bed length is not long enough for the boundary layer to redevelop. Additionally, the LES-RANS interface is previously found to also influence the near-bed flow behaviour. Therefore the observed misfit is in part believed to be related to the use of wall functions and the presence of LES-RANS interfaces near the bed.
- The snappyHexMesh utility extruded the bed model out of the channel domain, resulting in quite skewed cell elements near the bed model. The utility tries to correct for this by iteration of the extrusion. However, the mesh output might have been inappropriate for the intended use in terms of mesh quality.
- The wall shear stress parameter is calculated by OpenFOAM and directly extracted for analysis. The wall shear stress of the test case is calculated with the use of velocity gradients. The bed model of the tests contains a surface that has a decent amount of variation due to the small roughness elements. This potentially results in small wake regions behind the bed particles where the local velocity gradients would differ from the numerical results.
- In continuation of the last item, the presence of bed particles makes it difficult to establish a ground level for the bed model where the velocity is defined as zero. This is necessary for the velocity gradient estimation since the highest values are expected to be located close to the bed surface. No practical way was found to establish the ground level, so instead the velocity derivative was based on two subsequent wall-normal cell values closest to the bed. This is still in close proximity to the bed surface, however it might be far enough to result in severe underestimations of the wall shear stress. This would agree with the numerical findings that give consistently higher wall shear stress estimations.

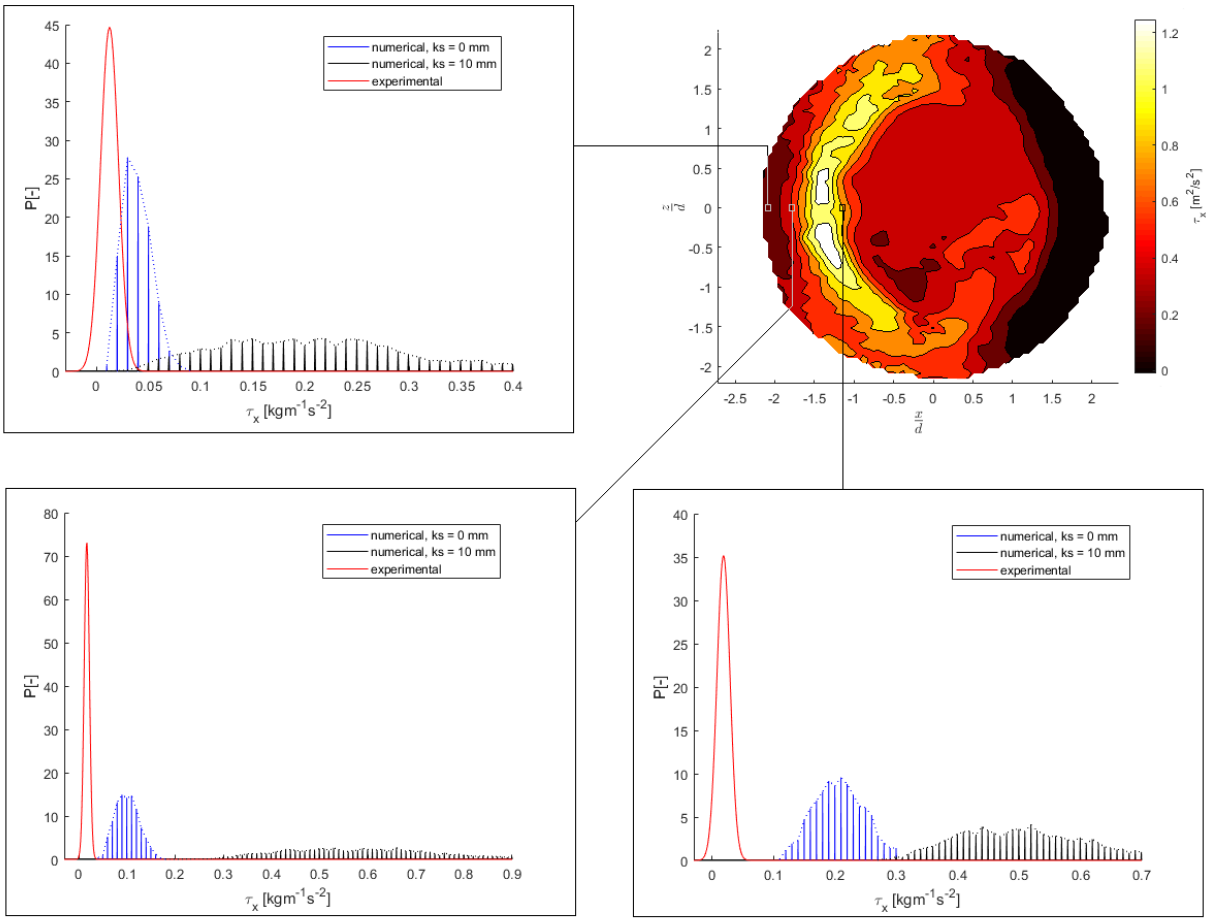

Figure 4.14: Top view of the streamwise component of the wall shear stress for a bed model with K_s = 10 mm. A comparison is provided for three location along the bed surface

- Turbulence models such as the Spalart-Allmaras model make use of an effective viscosity ν_{eff} that is comprised of a laminar and turbulent component. In this case the turbulent viscosity is being modelled by the solver so that there is a additive component in the viscosity ν. This is not being considered in the calculation of the wall shear stress for the test results. This additive component should approach very small values near the wall so that it has only little influence on the value of ν. However, this has not been investigated for the bed model and might affect wall shear stress estimations by the numerical model.

It is mentioned that the contribution of each of the listed items requires further investigation and that the issue remains not well understood. The implication of this observation is limited for the purpose of this study, since the indicator fields are only analysed at this point. It does, however give insight in the application issues of the IDDES model in case flow-bed interaction is being modelled.

4.3.3. Entrainment indication parameters

To asses the entrainment of stones from the bed protection layer model, the indication parameters for drag and lift are again considered. Each of the damage indicating parameters at the bed surface are depicted in Figure 4.15 for a smooth bed surface and Figure 4.16 for a rough bed surface with K_s value of 10 mm. First the results of the smooth bed model are discussed.

The drag component D_{ind} of the hydrodynamic forcing is indicated by magnitude of the wall shear stress. The field shows a steady increase of the drag component during the initial fluid-structure interaction along the slope of the bed up to a maximum value when the bed model flattens out. The opposite observation is made at the other end of the bed model where the flow starts separating from the model. The increase in wall

shear stress is related to the flow velocity increase seen in Table 4.4 where to highest flow velocities are seen after the slope changes and the bed model remains more or less equal in level.

Next, the drag fluctuation indicator D'_{ind} is considered that is represented by shear stress fluctuations. The field shows that the prominent regions are located at sections where the surface slope of the bed model alters. Additionally, the highest values are observed at the back side of the model. This can be explained by the flow separation that occurs at this location. In general, the field is very similar to that of indicator D_{ind}, however the field shows much less diversity in accentuated regions on top of the bed model.

The projection of pressure gradients of indicator H_{ind} shows vastly different prominent regions for entrainment. The field indicates that the largest pressure gradients are found at the front side and back side of the model with respect to the flow direction. The largest damage values are seen at the top section of the slope. It is again mentioned for this field that a large spreading of stability values can be seen.

The lift fluctuations indicator L'_{ind} shows quite distinct regions that partly coincided with those of fields H_{ind} and V_{ind}. In contrast with the mentioned fields, the L'_{ind} indicator field accentuates the very first fluid-structure interaction region at the sloping section of the bed model. Additionally, it suggests entrainment of bed material at regions where the surface slope flattens primarily at the front and back sides of the model.

When looking at the fields of the rough bed model in Figure 4.16 a consistent trend can be observed. All fields now indicate entrainment regions at the front side of the bed model. The largest differences are seen by comparison of the drag fields D_{ind} and D'_{ind} with those obtained with a smooth bed model. At first those fields suggested particle entrainment at the backside of the model instead. It is also apparent that the spreading of the stability values for the mentioned fields have significantly increased. A possible explanation for this trend is that the surface roughness results in higher local turbulence levels, so that larger near-bed velocity fluctuations are obtained. Because of this the field values of D'_{ind} are generally higher than observed for the smooth bed model case.

It is restated that the entrainment of bed material is expected to be a result of the combined effort of different indicators. The coinciding regions between the mentioned indicators are therefore most of interest. However, as seen with the cylinder model, the initiation of stone displacement might be governed by specific force contributors. For the presented rough bed model a entrainment region is identified at the front side of the bed model which trails of to the side of the model. Due to the absence of test data this is a suggestive prediction only.

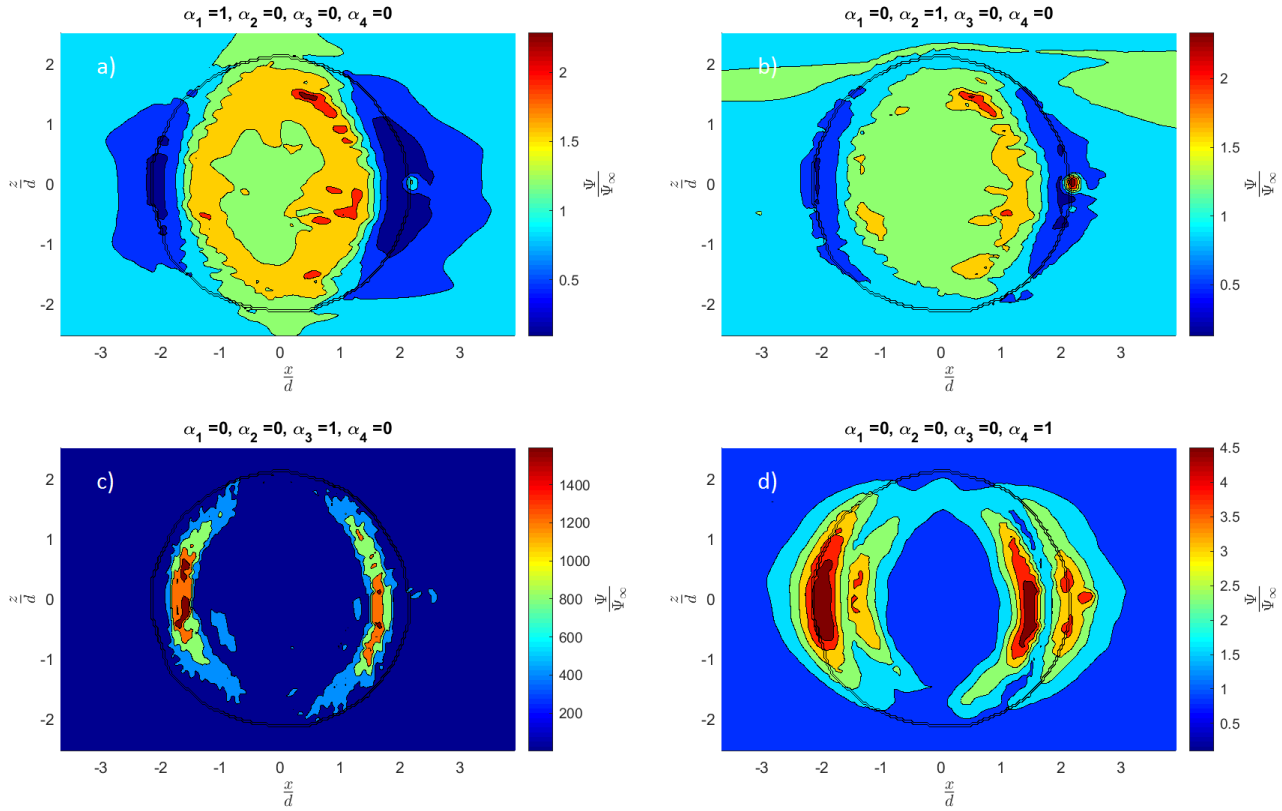

Figure 4.15: Top view of indicator D_{ind} defined by wall shear stress (a), indicator D'_{ind} defined by wall shear stress fluctuations (b), indicator H_{ind} defined by pressure gradients (c) and indicator L'_{ind} defined by pressure fluctuations (d) over a smooth bed model

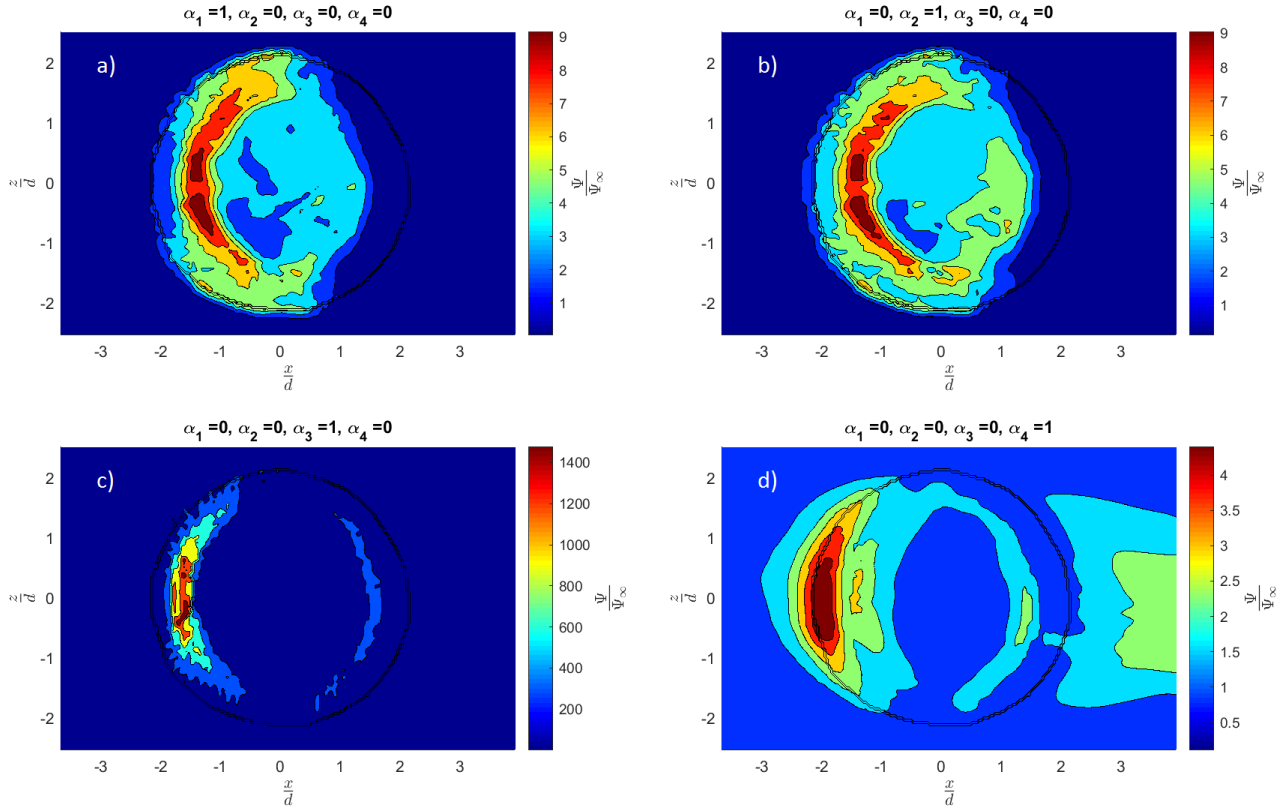

Figure 4.16: Top view of indicator D_{ind} defined by wall shear stress (a), indicator D'_{ind} defined by wall shear stress fluctuations (b), indicator H_{ind} defined by pressure gradients (c) and indicator L'_{ind} defined by pressure fluctuations (d) over a rough bed model with K_s = 10 mm

4.4. Open channel simulation including both a cylinder and protection layer

In this section the final simulation case is discussed that includes a cylinder and a protection layer. The procedure of the analysis is similar to that of the last section where the flow fields are investigated in addition to the wall shear stress statistics and the entrainment indication parameters.

4.4.1. Effect of bed model roughness

In the previous section an analysis on the bed roughness was performed and ultimately a bed roughness height of 10 mm was considered to correspond best to test results. This bed roughness is also applied to this model for the rough bed model simulation. To analyse the effects of surface roughness also a smooth bed model simulation is performed. The streamwise component of the mean velocity fields are shown in Table 4.5 for the test and numerical cases. By comparison of the flow velocity fields the velocity overshoot is again noticeable in both simulation cases. The flow velocity increase along the slope of the bed corresponds very well to that of the test. However, the point of flow deacceleration that the test case shows is situated closer towards the cylinder than the numerical models predict. In addition, the numerical models again show an excessive backflow region near the cylinder-bed junction. This was also observed when only including a cylinder in the domain. The issue was related to the presence of a velocity overshoot and the local inapplicability of the wall function. Another possible cause is the bed model that is being modelled as a solid medium, whereas the actual bed was porous. This limits the possible flow direction near the cylinder-bed junction so that flow might ultimately be forced backwards. However, this is not believed to be a governing reason as the issue of excessive backwards flow was already observed in absence of the bed model. Interestingly, the difference plots of the simulation models suggest a larger error in the near-bed velocity predictions for the rough bed with K_s = 10 mm. Even though this surface roughness gave better predictions in case only a bed model was considered. This suggests that the presence of the cylinder dominantly influences the upstream flow fields that is predicted by the numerical model. This is further inspected in Figure 4.17 where the mean streamwise velocity profiles from the test and numerical cases are shown for specific bed locations. Here it is noticed

Table 4.5: Comparison of the streamwise velocity component between the experiment results and three numerical cases that differ in bed roughness. K_s values of 0 mm (top) and 10 mm (bottom) are considered

Experiment	Simulation	Difference
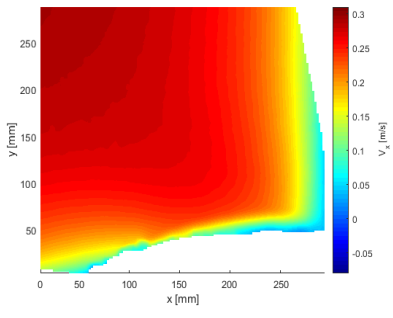	K_s = 0 mm 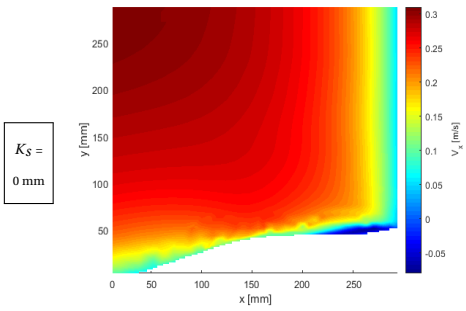	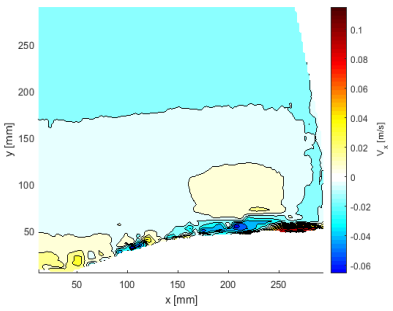
	K_s = 10 mm 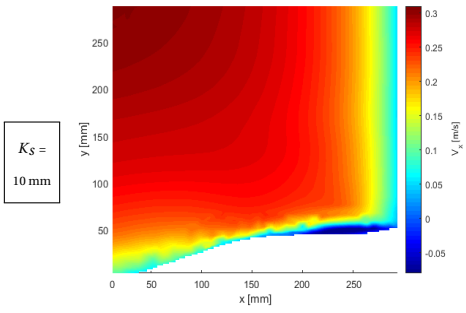	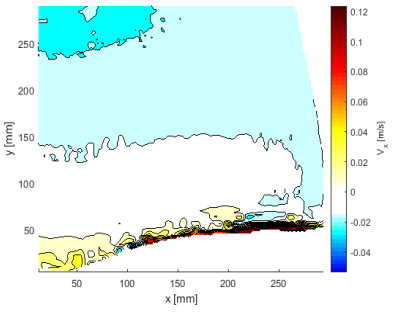

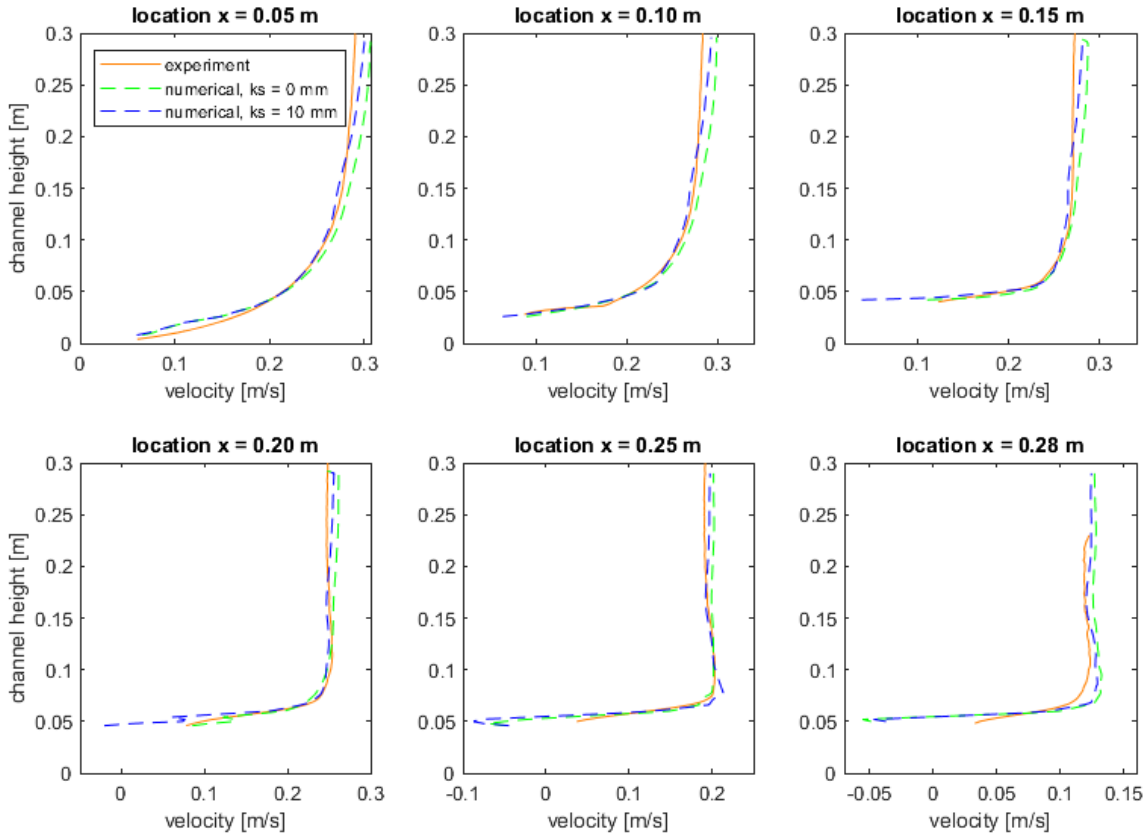

Figure 4.17: Mean streamwise velocity profile comparison at different bed locations

that, in general, the simulation with a smooth bed model better predicts the near-bed velocities, whereas the rough bed simulation gives better predictions for the ambient velocities. Very close to the cylinder the models predict very similar velocity profiles. So the difference is primarily noticeable at larger distances upstream from the cylinder where the bed surface level remains a constant height of approximately 5 cm. The cause for this observation could be related to the lowering of near-bed velocities in case of a rough surface bed. This is ultimately compensated for higher up in the channel column where higher flow velocities are expected to occur. This then will increase the negative pressure gradient towards the cylinder, so that a larger downwards flow is obtained that also results in a larger backflow region. This seems to bo the case as, after flattening of the rough bed model, the very near-bed velocities are actually negative which indicates that the backflow region has expanded. It is therefore claimed that this issue is at least partially related to the inability of the wall functions to accurately predict flow separation in backflow regions.

4.4.2. Wall shear stress evaluation

Next, the wall shear stress estimations of the numerical models are compared with those of test results. The wall shear stress over the bed model is shown in Figure 4.18. For three locations upstream of the cylinder a comparison is shown regarding the streamwise component of the wall shear stress. Identical observations are made regarding the statistics of the wall shear stress as in case only a bed model is included in the domain. It is again apparent that the simulation case with a smooth bed model gives wall shear stress estimations that are more comparable with those of the test case, however a consistent overprediction can seen. This issue is amplified for the simulation case that includes a rough bed model. The estimated wall shear stresses are lower in comparison with the simulations results that only include a bed model. So this indicates that the presence of a cylinder reduces the upstream wall shear stress values. It was previously stated that the additional inclusion of a cylinder in the domain seemed to have a dominant effect on the flow patterns upstream of the cylinder. The results depicted here contradict this statement as the statistics of the wall shear stress

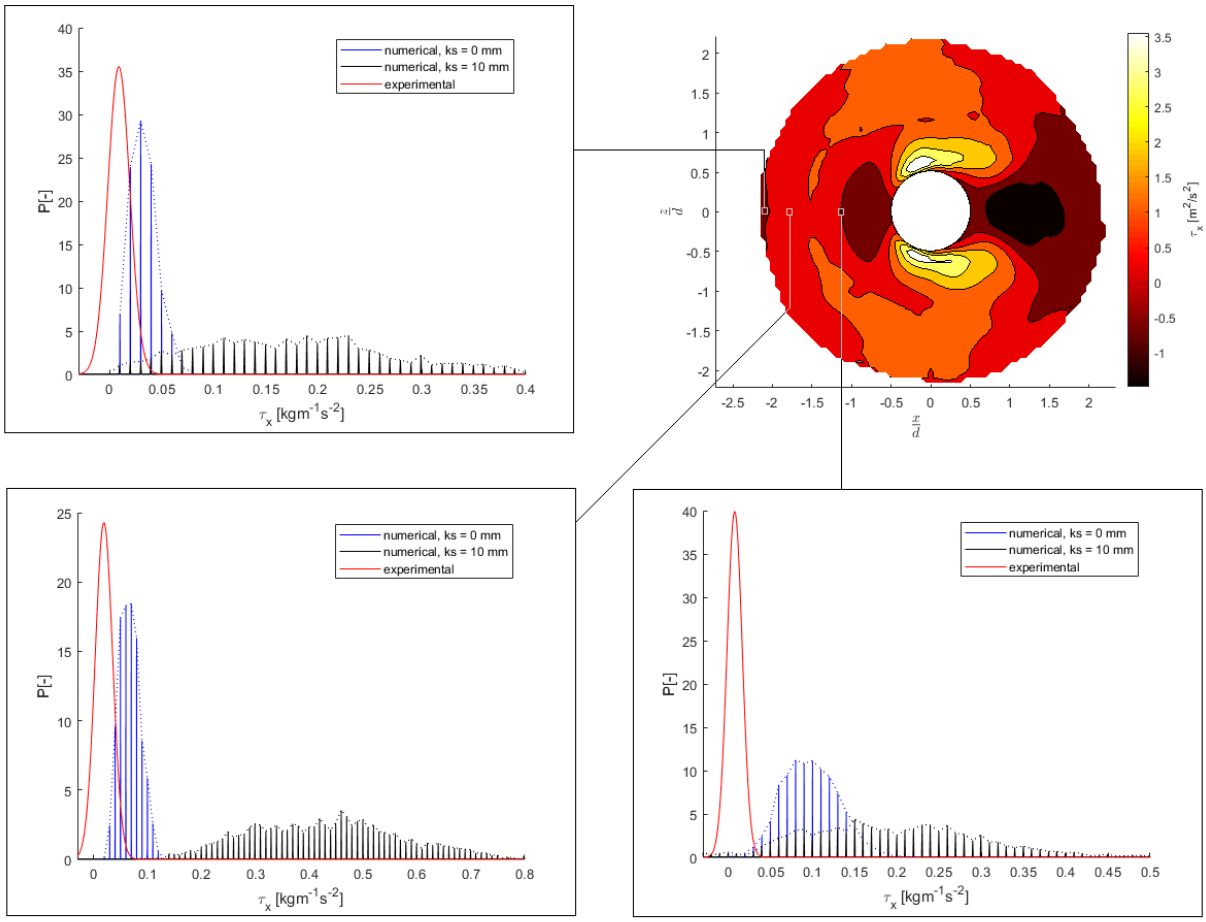

Figure 4.18: Top view of the cylinder displaying the magnitude of the wall shear stress for a bed model with K_s = 10 mm. A statistical analysis is performed for three location upstream of the cylinder

primarily corresponds to the bed model simulations. It is restated that the differences between the distributions are not fully understood. In Section 4.3.2 a number of potential causes are listed for the misfit between the numerical and test cases.

4.4.3. Entrainment indication parameters

Finally, the simulation models are used to give estimations of entrainment indication parameters for the drag and lift components of the hydrodynamic forcing. Each of the damage indicating parameters at the bed surface are depicted in Figure 4.20 for a smooth bed surface and Figure 4.21 for a rough bed surface with a K_s value of 10 mm. It is interesting to notice that the indicator fields with a smooth bed model surface are very similar to those of the results with only a cylinder included. The main difference is that the stability parameter indicates larger extreme values so that the severity of the loading is expected to increase. In comparison with the rough bed model in Figure 4.21 the same regions are being accentuated by the indicators. The stability values of fields D_{ind} and D'_{ind} have substantially increased, whereas those of H_{ind} and L'_{ind} have decreased instead with respect to those of the smooth bed model simulation. The effects of surface roughness seem limited in terms of the location where entrainment can be expected. Therefore the inclusion of the cylinder is stated to be a dominant factor over the bed roughness in terms of the location where entrainment is expected. The bed roughness does, however, have an effect on the stability parameter so that the severity of damage to the bed during initial stages alters. This of course depends on the contribution of each of the indicators with respect to field test data. The regions that is of interest are the overlapping indicator regions so that a maximum value of the stability formula is obtained. In this case, identical to the model that only includes a cylinder, two separate regions are considered. The first includes the prominent regions of indicators D_{ind}

and H_{ind} upstream and towards the side of the cylinder. The second coinciding region comprises of the accentuated regions of D'_{ind} and L'_{ind} that are located downstream of the cylinder.

In Figure 4.19 the damage patterns due to co-directed waves and currents are shown as a result of fluid-structure interactions with a cylinder and rough bed protection layer. The presence of wave conditions is known to result in backfilling behaviour of the scour holes. This results in less scour depth in mild combined-current-and-waves loading than in current-only conditions, assuming identical current conditions [38]. The damage patterns of Figure 4.19 are therefore considered to give insight in the specific locations where entrainment can be expected. It is stressed, however, that the figures are not depicting initial scour patterns. It is assumed that long-term scour effects are related to initial scour effects in terms of the specific scour locations, so that the figures can be used as reference for bed damage patterns. The left figure depicts the bathymetry level after hydrodynamic loading, showing significant scour effects on top of the protection layer model. The right figure provides a measure of scour depth, given in percentages of the cylinder diameter. Identical to the simulation results, two regions of particle displacement are observed. The first is located upstream and towards the side of the cylinder and the second is located further downstream of the cylinder. The figures also indicates disposition of material at the backside of the cylinder, that is believed to influence the upstream and downstream flow patterns and scour effects over time. It is interesting to notice that indicator D_{ind} with a rough bed model does depict a more concentrated region of critical stability values than when a smooth bed model is considered, which is more in accordance with the test damage patterns to the side of the cylinder. For the downstream scour region the D'_{ind} indicator fields of both bed models depicts a critical entrainment region more towards the side of the cylinder, whereas both L'_{ind} fields are situated directly at the backside of the cylinder. The last one mentioned does compare better with the downstream scour region of the test case. In general, the comparison does suggest that the numerically obtained indicators are able to predict similar entrainment regions as the presented test case.

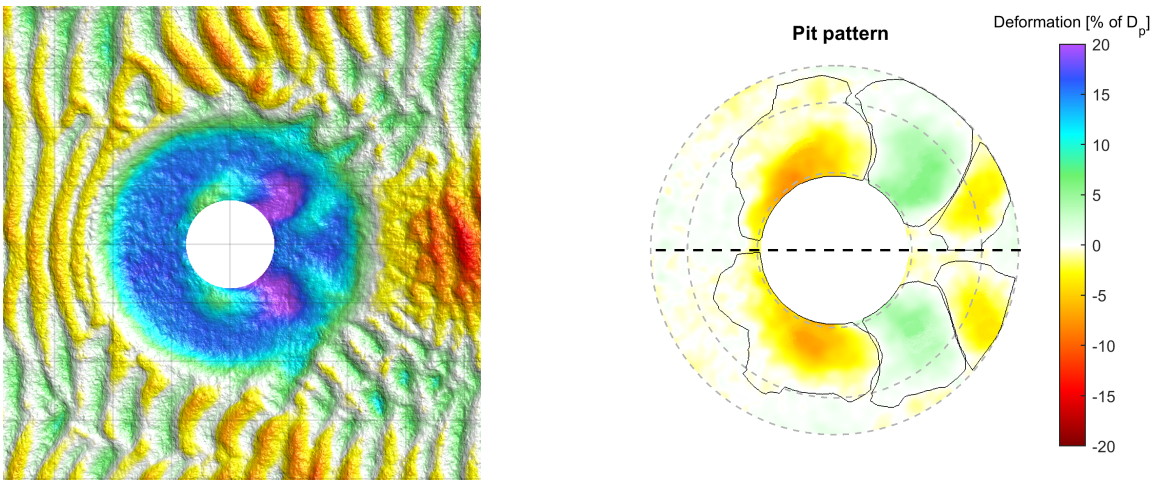

Figure 4.19: Test damage patterns (left) and corresponding entrainment locations (right) due to wave and current interaction with a cylinder and rough bed protection model

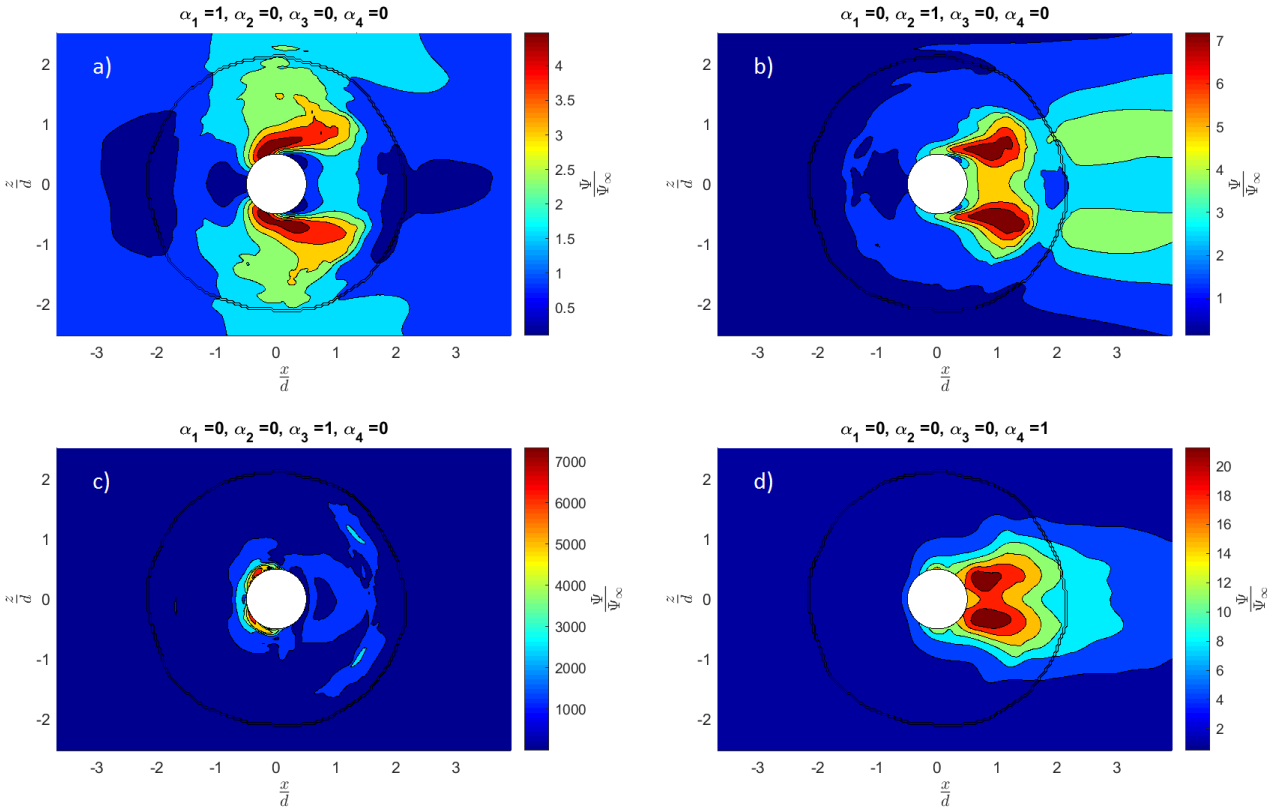

Figure 4.20: Top view of indicator D_{ind} defined by wall shear stress (a), indicator D'_{ind} defined by wall shear stress fluctuations (b), indicator H_{ind} defined by pressure gradients (c) and indicator L'_{ind} defined by pressure fluctuations (d) over a smooth bed model

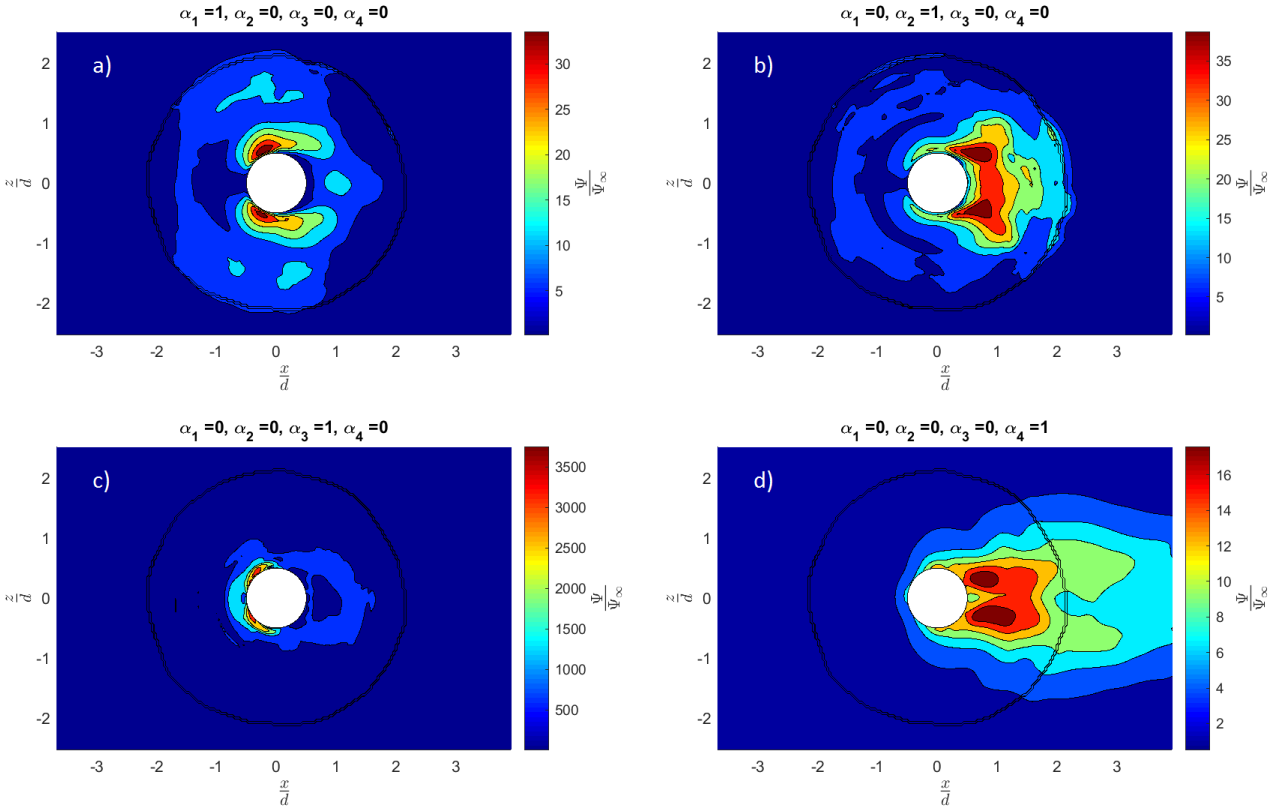

Figure 4.21: Top view of indicator D_{ind} defined by wall shear stress (a), indicator D'_{ind} defined by wall shear stress fluctuations (b), indicator H_{ind} defined by pressure gradients (c) and indicator L'_{ind} defined by pressure fluctuations (d) over a rough bed model with K_s = 10 mm

5
Discussion

In this chapter a reflection is provided on the performed experiments and the numerical test results. This is included to stress uncertain aspects experienced during the study.

5.1. Considerations regarding the experiments

First, a few remarks regarding the processing of experimental data are given. Overall, it was found that fitting of the log-law through velocity data in the logarithmic region of the boundary layer yielded good results. It was, however, also observed that the calibration of the measurements results had moderate influence on this fitting process. This calibration was required to shift the measurement data in accordance with the location of the wall as the zero point was set in the centre of the sampled test region by the processing system. To have the zero point in wall-normal direction related to the position of the wall, a calibration distance towards the wall had to be specified. This process was somewhat imprecise as the measurement data showed a large, highlighted region near the wall due to the sensitivity of the camera to the wall-reflected laser light. The estimation of the calibration parameter was ultimately based on the first pixels encounter in the measured field that showed high light intensities. It was found that this parameter does have a significant influence on the dimensionless velocity profile and the downwards shift, thus affecting the fitting process of the log-law function. This ultimately results in different values for the fitting parameters ΔB and u_τ.

The EMS measurements were used to extrapolate the obtained field measurements of the PIV system to obtain an estimate of the free surface velocity in the channel. However, he EMS data showed a moderate amount of spreading, making it difficult to approximate the velocity profile in the upper region of the channel. This was accentuated by the fact that only one EMS was located above the PIV-sampled region so that numerous ways of extrapolation were possible. The assumption was made to consider a slope with a very small velocity gradient. In hindsight, the occurrence of velocity-dip phenomenon was overlooked which actually corresponds better with the EMS measurement data. This would have resulted in a different estimation of the free surface velocity, which in turn affects the boundary region approximation. It is noted however, that the difference is expected to be small as the currently obtained function fit is in very good agreement with the velocity data.

5.2. Considerations regarding the numerics

5.2.1. Wall functions

Next, numerical consideration are discussed. One of the main findings of the preliminary numerical study was the inaccuracy of the wall shear stress estimation during the simulation when using wall functions. For RANS models an under prediction of approximately 6 % for the Spalart Allmaras model up to 25 % for the realizable k-ϵ was found for the friction velocity with respect to the fitting parameter u_τ. In case of the IDDES hybrid model the extend of the error was found much greater with relative differences found up to a value of 64 %. In observing the accuracy of the fitting function for both the RANS and IDDES models, it is found that the logarithmic region of the boundary profile is better approximated in the RANS model. In case of the IDDES the function fit of the log-law is not as accurate as shown in Figure 5.1. The misfit is believed to result from an interplay between the RANS and LES modes. This has also been mentioned in Section 4.1.2 where

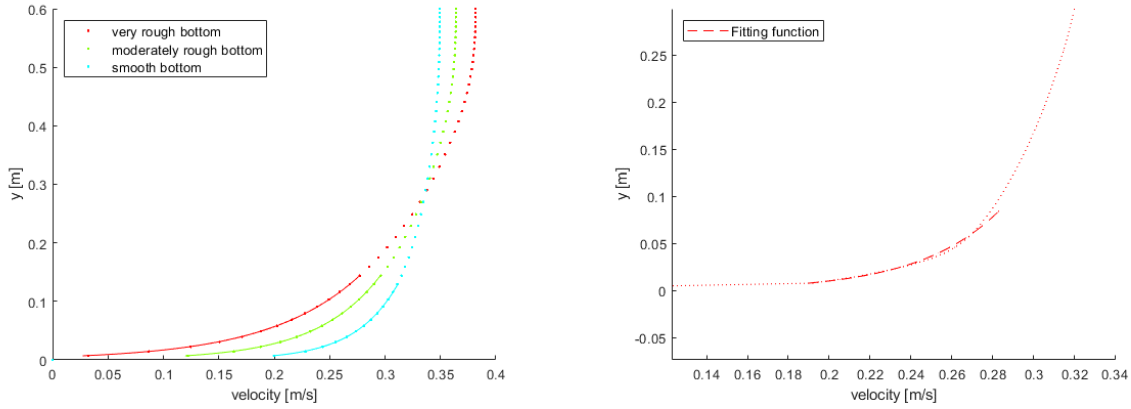

Figure 5.1: Fitting curves through velocity profiles computed with RANS (left) and IDDES (right)

discrepancies of flow statistics were found for the first couple of successive wall-normal cells in which the RANS-LES interface was found to be located. Because the function fit showed discrepancies, the resulting fitting parameter u_τ is not fully representative of the local boundary profile. So the issue is not necessarily attributed to the different values obtained for the friction velocity, but to the misfit of the log-law function for the IDDES model. A possible reason for this issue is that the implementation of the IDDES model, based on Spallart Allmaras, in OpenFOAM is erroneous as difficulties were also found in applying the IDDES model, based on the $k-\omega$ SST model. The latter model was namely found to return an averaged velocity field only as if a RANS model was used. Initial iterations during simulation showed that a large percentage of the domain was solved in LES mode, however the situation quickly converged to a RANS mode only. The issue is only mentioned here and requires further investigation.

With regard to the wall functions themselves, their use in simulations is considered dubious regarding wall shear stress estimations as the resulting velocity profile does not fully correspond to the wall roughness input. In this way it was found that, when assigning a smooth wall function to a wall, the resulting velocity profile was indicative of one that relates to a rough wall. This inherent roughness is referred to as numerical roughness. Its value differs depending on the model used, the locally estimated wall shear stress as well as the actual roughness input. Since it is not a constant, it is difficult to estimate the apparent roughness that is incorporated in the simulation model. This is illustrated with the following equation:

$$\Delta B_{tot} = \Delta B_{input} + \Delta B_{numerical} \tag{5.1}$$

ΔB_{tot} represents the total roughness that is actually accounted for at the wall by the model. ΔB_{input} is the roughness input via parameters K_s and C_s that is specified by the user of the wall function. $\Delta B_{numerical}$ is the numerical roughness present in the model due to the inaccurate estimation of the wall shear stress. Since $\Delta B_{numerical}$ is a variable quantity it is difficult to accurately estimate the total roughness ΔB_{tot} that is included in the model. Since it is found that $\Delta B_{numerical} > 0$, it also implies that no smooth wall can be represented in the numerical domain with wall functions.

Even though $\Delta B_{numerical}$ is a variable quantity, Table 3.2 indicates that the $\Delta B_{numerical}$ is somewhat correlated for each model. The realizable $k-\epsilon$ model shows a numerical roughness in the order of 3.7 for walls with small to no roughnesses. For identical conditions the $k-\omega$ SST model shows a numerical roughness in the order of 1.98 - 2.33, whereas the S-A model shows a numerical roughness of 1.25 - 1.79. In order to compensate for this observation a restoring component is suggested that counteracts the numerical roughness according to the following equation:

$$\Delta B_{tot} = \Delta B_{input} + \Delta B_{numerical} - \Delta B_{restore} \tag{5.2}$$

Where $\Delta B_{restore}$ is an empirically determined restorative component that attains a value depending on the input roughness and RANS model. Different values of $\Delta B_{numerical}$ for walls with small to no roughnesses have been mentioned that could be counteracted by $\Delta B_{restore}$. Note that this parameter also depends on the wall shear stress so that the simulation terrain is of importance. It is additionally noted that this is a measure to counteract the roughness error that is observed in the fitting parameter ΔB, which is found to represent a horizontal velocity shift of the boundary profile. Fitting parameter u_τ is not being altered, which primarily

contributes to the shape of the boundary profile over the height. Fixing this issue is actually more important as the wrongly estimated wall shear stress (and therefore u_τ) results in the inclusion of a numerical roughness. A similar issue has been studied by Mukha et al. [31] for the WMLES model who proposes sampling of the third consecutive off-the-wall cell centre instead of the wall-adjacent cell as this yielded significant better results for the wall shear stress estimation. Mukha mentions that the methodology is applicable to complex geometries, however this statement is questioned in severely disturbed boundary flows or reverse flows where the velocity gradient of the third consecutive off-the-wall cell centre might not correlate well to that of the log-law profile. The same statement can be made for the current implementation of the wall shear stress estimation, so it is currently unknown which implementation would result in a better shear stress estimation in case of severely disturbed boundary flows or reverse flows.

5.2.2. Model application in flow separation regions

An important observation of the simulation results was the presence of an excessive backflow region upstream of the cylinder model. This possibly result from the use of wall function in specific regions where the local flow profile does not correspond to a logarithmic sub-layer, which the formulation of wall functions is based on. Further analysis shows that critical regions can be isolated with the use of the averaged $y+$ field of the simulation. An example is provided in Figure 5.2 where the numerical domain with a cylinder is considered. For every simulation case a wall-normal cell distance was specified that resulted in an averaged $y+$

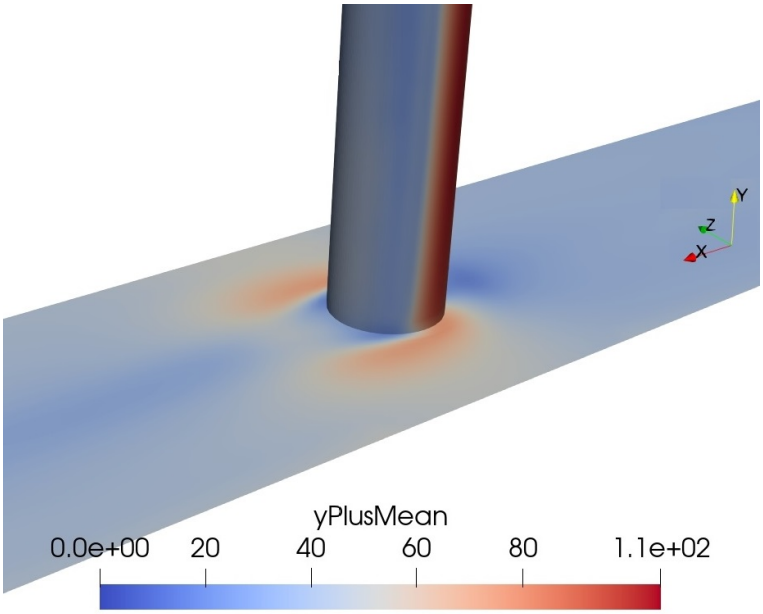

Figure 5.2: Depiction of averaged $y+$ values downstream of the cylinder

value of approximately 40 in the free stream condition. A recommendation value of 30 is given in literature, however it was found that the value of $y+$ fluctuates according to associated velocity fluctuations. Therefore, to account for the parameter fluctuations, an additional margin was considered. In the figure an increase of the averaged $y+$ value can be seen due to the fluid-structure interaction that result in an increase of flow velocity around the cylinder. However, downstream of the cylinder, where flow separation occurs, the opposite is true as low parameter values are observed. This can also be seen in the stagnation region upstream of the cylinder. The specific regions are expected to have low averaged $y+$ values as the local velocities are anticipated to be relatively low as well. So this issue is unavoidable when using wall functions in simulation cases where flow separation is expected. In Chapter 7 a suggestion in made that attempts to refrain from the use of wall functions in regions of flow separation.

5.2.3. Schematization of roughness elements

Following up, the numerical inaccuracies with respect to the test cases due to model differences are stressed. The first mentioned is the significant resolution difference of the protection layer model that was due to

specific mesh requirements near the wall that followed from using wall functions. The resolution difference mainly affects the surface roughness of the numerical model which as a result is severely underrepresented. Because of this the bed model was smoothened and an estimation of the roughness parameter ΔB was made for the velocity profile over the bed surface. The velocity profile and the corresponding fit are shown in Figure 5.3. It can be seen that the logarithmic boundary layer fit is not as accurate since the boundary layer is still developing. This, in combination with the presence of a numerical roughness, makes it difficult to estimate a sufficient roughness parameter beforehand to be applied to the bed model.

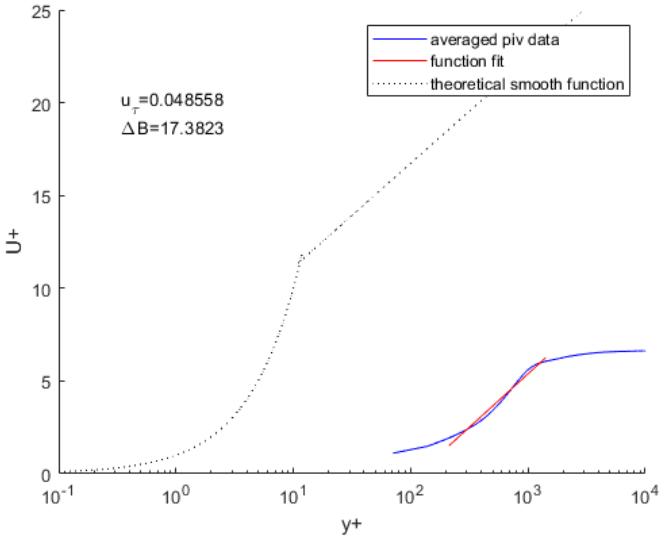

Figure 5.3: Normalised velocity profile above the rough bed and associated fitting function

The second aspect regarding the protection layer model relates to its porous structure. Due to uncertainties in the applicability of Darcy's law in turbulent flow conditions it was modelled as a solid impermeable structure instead. This naturally affects the flow around the model as the fluid-structure interaction is different than in the test model. The numerical model is expected to overestimate the flow acceleration over the model as a result of this assumption. This is because the local flow is not being allowed to partially circulate in the bed model, as is expected for a porous bed model, and is ultimately forced over it instead. This means that the flume cross section is effectively more reduced when a impermeable bed model is considered than when a permeable one is. Therefore, according to the continuity equation, the flow velocity over the bed model is expected to increase.

6

Conclusion

The objective of the performed numerical study is stated as the following in Chapter 1:

To evaluate the applicability of the IDDES hybrid modelling technique for simulating a cylinder-bed junction in an open channel so to asses its ability to predict particle entrainment due to turbulent flow conditions.

In order to achieve the formulated objective, four research questions are formulated which are discussed in this section.

Which numerical modelling approach is most appropriate in simulating turbulent flows near a cylinder-bed junction region related to the entrainment of sediment?

In this study turbulent flow conditions associated with a Reynolds number of 3.6×10^4, based on the cylinder diameter, were analysed. The specific region of interest was close to the cylinder-bed junction where entrainment of sediment is expected due to flow-structure interactions. The Direct Numerical Simulation (DNS) and Large Eddy Simulation (LES) methods were investigated for use and research showed that these models require very fine mesh resolutions near the wall in turbulent flow regimes to accurately resolve the associated vortex structures. Thereby the conclusion was made that both models are too expensive for simulating multiple test configurations with respect to the time frame of the study. To still resolve part of the turbulent features in the flow a hybrid modelling technique was considered. Specifically, the Improved Delayed Detached Eddy Simulation (IDDES) model was considered as the mesh requirements near the wall were severely reduced. This model tries to combine the advantages of multiple simulation methods which is ultimately depend on the mesh resolution and flow conditions. For coarse meshes it uses a relatively cheap Reynolds Averaged Navier-Stokes (RANS) model, whereas with finer mesh resolution it switches to the Wall-Modelled LES (WM-LES) or even wall-resolved LES. With this the computational time of each simulation can be reduced, however at the cost of numerical accuracy. For the purpose of this study, where multiple simulations were performed in a limited time span, it was found most appropriate to consider the hybrid modelling technique, where the IDDES model was presented as the most flexible model regarding the mesh requirements.

How to properly account for the surface roughness in the numerical model and how well is the assumed near wall boundary profile approximated?

Since a hybrid modelling method was considered, the mesh resolution near the wall was limited so that the boundary profile could not accurately be resolved. This problem, however, is avoided with the use of wall functions. Wall functions are empirically determined from test studies and resolved DNS simulations. The boundary profiles show that there is a specific region within the boundary layer profile that corresponds very well to a calibrated logarithmic function, known as the log-law. Since the log-law is specifically specified for a certain region of the boundary profile, the mesh has to be accordingly constructed so that its first wall-adjacent cells reside within this logarithmic region. This constraint can not always be complied with since the assumption of a developed boundary profile is not always valid, such as for a separated flow or a

reattachment zone. The roughness of a surface can also be accounted for in the wall functions by means of a roughness parameter ΔB. A study was performed towards the accuracy of wall functions in describing the assumed boundary profile. Multiple mean velocity profiles were generated and the log-law function was fitting through the logarithmic part of the boundary layer. Surprisingly, it was found that the use of wall functions is associated with an artificial roughness due to an inaccurately estimated wall shear stress. This inherent roughness is referred to as *numerical roughness* as it results from a local numerical discretization scheme. It was found that numerical roughness is a varying quantity that depends on parameters such as the turbulence model, the input roughness and the local shear stress. The result of the numerical roughness is an altered velocity profile over the height of the channel than is expected with the roughness input parameters. It is additionally assumed that it affects the near-bed flow characteristics. To partially resolve the issue a restoring parameter $\Delta B_{restore}$ is suggested that counteracts the numerical roughness to a certain degree. However, the issue is believed to originate from the linear velocity derivative estimation in the definition of the wall shear stress. Therefore further investigation is suggested regarding this issue so that an appropriate solution is obtained.

What is the accuracy of the numerically obtained flow patterns and associated statistics of entrainment-indicating parameters on the bed?

The first simulation was based on an open channel case with no inclusions present within the numerical domain with the goal to compare numerically obtained flow features to that measured in the experimental case. Results depicted that the measured mean velocity profile over the height of the channel could decently be approximated by numerical means. However, due to the presence of a numerical roughness a velocity overshoot in the upper region of the channel was observed. Statistical analyses on the mean flow field showed very comparable results between the measured and simulated flow field as shown in Figure 4.3 and Figure 4.4. A noticeable difference is observed by comparison of the wall-normal component of the velocity in the near-wall region where a relative difference of 40 % was found for the standard deviation. The same region depicts a dubious asymmetrical distribution for the streamwise velocity component. A possible explanation for those observations are the RANS-LES interfaces that reside within this region. Inspection of this interface showed that the corresponding logarithmic profile was misrepresented, suggesting that the error originates from the interplay between the LES and RANS modes.

The next simulation was focussed on a flow around a cylinder. Here the cylinder walls were modelled with wall functions. Analysis of the flow behaviour related decently well to reference values in literature. A prominent finding was that the flow around the cylinder, which was modelled with smooth walls, actually corresponded to a flow around a cylinder with walls that include a certain degree of roughness. This observation is in line with previous findings regarding wall functions and the inclusion of a numerical roughness. An assessment was made on the statistics of the wall shear stress values and were found to consistently underestimate the wall shear stress values of test results. The difference was found largest near the cylinder-bed junction due to an excessive backflow region that was predicted by the model. This is attributed to the invalid use of wall functions in regions where flow separation is expected and to the presence of a velocity overshoot in the velocity profile. Based on the stability criteria of Hofland [18] and Shields [45] a new formulation is presented that attempts to accounts for the limited grid resolution of IDDES-based simulations that make use of wall functions. The formulation makes use of different potential entrainment-inducing parameter D_{ind}, D'_{ind}, H_{ind} and L'_{ind} that were specified to represent lift, drag and respective fluctuating components of the hydrodynamic forcing on the bed. These indicators were used to predict regions where displacement of sediment is most probable during initial stages of flow around a cylinder. It was found that the drag force indicator D_{ind} and H_{ind} correlated best to the particle displacement around cylinders observed in test cases. It is therefore assumed that initial entrainment of bed particles is dominated by those indicators. The test results also showed particle displacement to the side and downstream of the cylinder, which is in correspondence with D'_{ind} and L'_{ind}. In general, the damage indicators showed promising results regarding the entrainment regions when using the IDDES model.

How does the inclusion of a bed protection layer alter the hydrodynamic load conditions on the bed and to what extend is the numerical model able to predict its inclusion regarding the hydrodynamic forcing on the bed?

The final two simulation cases introduce a bed model so that an analysis was performed on the entrain-

ment of protection layer particles. In addition, the effects of bed surface roughness were analysed. The first simulation cases include only a smooth bed model. The results showed high drag indicator values D_{ind} and D'_{ind} at the top side of the bed, whereas H_{ind} and L'_{ind} indicated particle entrainment at the frontside and backside sloping section of the bed model. Inclusion of a rough bed model with roughness height K_s = 10 mm instead resulted in a shift of the most prominent stability values towards the front side of the model. The indicator fields have not been compared to test damage patterns as no such data was acquired.

The final simulation cases include a bed model as well as a cylinder model in the numerical domain. It was found that the most prominent regions where entrainment is expected were comparable to those of the simulation model that only includes a cylinder model in its domain. Two separate regions are identified where indicator regions overlap so that highest bed load parameters are obtained. The first includes the prominent regions of indicators D_{ind} and H_{ind} upstream and towards the side of the cylinder. The second includes fields D'_{ind} and L'_{ind} that suggest entrainment directly downstream of the cylinder. Inclusion of a bed roughness had limited effect on the location of expected entrainment region. However, the indicated bed load was altered by a change of the indicator field values. The numerically obtained indicator fields were found to predict similar entrainment regions as observed in a test case. However, it is stressed that the damage patterns of the test case depicted long-term scour effects in addition to wave scour effects. Therefore additional comparisons are recommended that include test data of initial scour pattern and current-only conditions.

It is mentioned that the statistics of the wall shear stress showed substantial different results for the numerical cases that include a bed model. The exact reason for this observation is not yet understood and requires further investigation.

7

Recommendations

In this study different cylinder-bed configuration have been simulated so to indicate region of potential initial particle entrainment. The hybrid IDDES turbulence model, based on the Spalart Allmaras formulation, was considered to reduce the expensiveness of the simulations. Based on the findings during the project the following recommendations are formulated:

- The concept of the wall functions is quite elegant, however a number of issues that were encountered have been attributed to the inaccurately estimated wall shear stress that is used in the application of wall functions. Is is therefore suggested that, in the scope of very near-bed flow phenomena, the estimation of the wall shear stress is improved in terms of its accuracy. A suggestion is provided that focusses on the improvement of the linear wall shear stress estimation in critical near-wall regions in which the use of wall functions is found inappropriate, such as in flow separation regions. A controlling function is proposed to be build into the hybrid model that recognizes regions of potential flow separation by assessment of flow characteristics in the wall-adjacent cells. Whenever an incoming boundary flow encounters a region of backflow, flow separation is expected to locally occur. Depending on the $y+$ values of the associated near-wall cells, a mesh refinement operation could take place in the surrounding region that reduces the wall-adjacent $y+$ values to a level that resides within the viscous sublayer. In the viscous sublayer a linear velocity profile is expected so that a linear estimation of the wall shear stress is more appropriate. Hereby the assumed velocity profile from the wall functions is than linearly interpolated onto the refinement region and by iteration a new equilibrium establishes for the separation region. The IDDES model is already calibrated to apply the wall-resolved LES mode when the grid is sufficiently fine. This means that the critical near-bed flow regions would be modelled with the LES method, whereas surrounding near-bed regions are still being modelled with the RANS model. It is mentioned in this thesis that the LES-RANS interface is believed to be associated with discrepancies that were found in the modelled boundary layer. The suggestion would introduce additional LES-RANS interfaces in the both directions parallel to the wall. Therefore it is additionally recommended that the LES-RANS interface is further investigated so to improve the ability of the hybrid model to predict near-bed flow behaviour. The suggestion of local mesh refinement aims to remain with most of the functionality of the IDDES model, while improving the applicability of the model after analysis of the shortcomings of wall functions. It is mentioned that the implications of a dramatic mesh refinement have not been studied in this thesis. Also, the dramatic mesh refinement will inevitably increase the expensiveness of the simulations. Here ultimately a compromise should made between model accuracy and cost, which is true for each of the available numerical models.

- in Section 5.2.1 a restorative component $\Delta B_{restore}$ is proposed that partially counteracts the numerical roughness $\Delta B_{numerical}$ that results from the use of wall functions. A number of test simulations have been performed for the $k-\epsilon$, $k-\omega$ SST and the Spalart Allmaras models that show that $\Delta B_{numerical}$ varies for each different model. To better understand the magnitude of the error that is observed in each model, numerous more simulations are suggested to be performed with varying roughness input values for ΔB_{input}. Ultimately, the obtained findings can be summarized in $\Delta B_{numerical}$ versus ΔB_{input} graphs that depict the extent of the error. The same graphs can then be used to estimate the

counteracting component $\Delta B_{restore}$. However, it is stressed that this is only a partial corrective measure as the error originates in the linear estimation of the wall shear stress, which the last item tries to address.

- Looking at the output of the IDDES model in comparison with the test results it is apparent that the estimation of flow characteristics is decently accurate for the mean flow component, whereas the fluctuating component shows differences of 10 to 40 % in terms of the standard deviation over the column of the channel. This margin should be accounted for when making predictions for extreme flow conditions if considering the IDDES turbulence model. Additionally, the flow statistics in the region closest to the bottom wall showed an asymmetrical distribution for the streamwise velocity component. In comparison with test results the distribution showed somewhat unphysical. This issue is attributed to the local presence of LES-RANS interfaces. It is recommended that, in case a hybrid model is considered, the near-bed velocity flow behaviour is considered with this knowledge so that (partial) unphysical behaviour is assumed.

- The statistics of the wall shear stress predictions by the simulations that include a bed models showed significant divergence from the test result. The observation of this discrepancy was surprising as the near-bed flow behaviour showed decent correspondence. It was also found that the effects of bed surface roughness had a large influence on the mean and standard deviation values of the wall shear stress. A number of possible causes for this observation have been listed in Section 4.3.2 and for a better understanding of the issue further investigation is recommended.

- In Section 3.1.2 the approximation of the velocity derivative is investigated so to analyse the extend of the error in the wall shear stress estimation. It was found that, referring to Figure 3.5, the relative difference of the velocity derivative is minimized when considering small $y+$ values at the wall. However, it is stressed that the use of wall functions is recommended in literature for a limited region of $y+$ values only. Therefore it is suggested to use $y+$ values near the lower end of suggested values. Additionally, it is advised to account for potential fluctuations of the $y+$ parameter due to flow fluctuations.

- The indicator fields of the simulation cases that include both a cylinder and a bed model were compared to a test case that depicted long-term scour effects and additionally included wave scour effects. It is recommended that the simulation results are also compared to initial scour patterns due to current-only conditions to further test the capabilities of the IDDES model in predicting initial scour entrainment.

- This study only analyses the indicator fields by means of the prominent regions that are depicted. The indicator parameters have been combined into a stability formula where entrainment is most probable based on fitting constants α_1, α_2, α_3 and α_4. The next step is to consider initial damage patterns of field tests and use the results for fitting of the stability formula to obtain estimates for the alpha constants. It is stated, however, that the use of wall functions and the presence of LES-RANS interfaces are believed to limit the applicability of the formulated stability formula with the IDDES formulation, as both are inherently present in the hybrid model.

Bibliography

[1] Empirical design of scour protections around monopile foundations: Part 1: Static approach. *Coastal Engineering*, 58(6):540 – 553, 2011. ISSN 0378-3839.

[2] United States. National Aeronautics and Space Administration. *NASA Conference Publication*. Number nr. 2085 in NASA Conference Publication. Scientific and Technical Information Office, National Aeronautics and Space Administration., 1979. URL https://books.google.nl/books?id=MYJWAAAAMAAJ.

[3] Yasin Aghaee and Habib Hakimzadeh. Three dimensional numerical modeling of flow around bridge piers using les and rans. 01 2010.

[4] Debashis Basu and Awatef Hamed. Des and hybrid rans/les models for unsteady separated turbulent flow predictions. *43rd AIAA Aerospace Sciences Meeting and Exhibit - Meeting Papers*, 01 2005. doi: 10.2514/6.2005-503.

[5] Abhinivesh Beechook, Humberto Medina, Hasna Fadhila, Svetlana Aleksandrova, and Stephen Benjamin. Effect of grid-filter width definition on implicitly filtered large eddy simulations using openfoam. volume 1863, page 030033, 07 2017. doi: 10.1063/1.4992186.

[6] Bert Blocken, Ted Stathopoulos, and Jan Carmeliet. Cfd simulation of the atmospheric boundary layer: wall function problems. *Atmospheric Environment*, 41(2):238 – 252, 2007. ISSN 1352-2310. doi: https://doi.org/10.1016/j.atmosenv.2006.08.019. URL http://www.sciencedirect.com/science/article/pii/S135223100600834X.

[7] G. Buresti. The effect of surface roughness on the flow regime around circular cylinders. *Journal of Wind Engineering and Industrial Aerodynamics*, 8(1):105 – 114, 1981. ISSN 0167-6105.

[8] Gary N. Coleman and Richard D. Sandberg. A primer on direct numerical simulation of turbulence - methods, procedures and guidelines. AFM 09/01a. University of Southampton, March 2010.

[9] R. Courant, K. Friedrichs, and H. Lewy. Über die partiellen differenzengleichungen der mathematischen physik. *Mathematische Annalen*, 100(1):32–74, Dec 1928. ISSN 1432-1807. doi: 10.1007/BF01448839. URL https://doi.org/10.1007/BF01448839.

[10] Corey D. Anderson and Stephen Lynch. Time-resolved stereo piv measurements of the horseshoe vortex system at multiple locations in a low-aspect-ratio pin–fin array. *Experiments in Fluids*, 57, 12 2016. doi: 10.1007/s00348-015-2091-7.

[11] Lars Davidson. An introduction to turbulence models, 2018.

[12] A. Duinmeijer, G. Oldenziel, and F. Clemens. Experimental study on the 3d-flow field of a free-surface vortex using stereo piv. *Journal of Hydraulic Research*, 58(1):105–119, 2020. doi: 10.1080/00221686.2018.1555558.

[13] Bojan Å ekutkovski, Ivan Kostic, Zoran Stefanovic, Aleksandar Simonovic, and Olivera Kostic. A hybrid rans-les method with compressible k-omegasstsas turbulence model for high reynolds number flow applications. *Tehnicki Vjesnik*, 22:1237–1245, 10 2015. doi: 10.17559/TV-20140404130058.

[14] Lewis F. Richardson. *Weather Prediction by Numerical Process*, volume 20. Cambridge U. P., 01 1922. doi: 10.2307/2003575.

[15] Nicholas J. Georgiadis, Donald P. Rizzetta, and Christer Fureby. Large-eddy simulation: Current capabilities, recommended practices, and future research. *AIAA Journal*, 48(8):1772–1784, 2010. doi: 10.2514/1.J050232.

[16] Mikhail Gritskevich, Andrey Garbaruk, and Florian Menter. A comprehensive study of improved delayed detached eddy simulation with wall functions. *Flow, Turbulence and Combustion*, 98:1–19, 08 2016. doi: 10.1007/s10494-016-9761-2.

[17] G. J. C. M. Hoffmans and H. J. Verheij. *Scour manual*. Rotterdam, Netherlands: A.A. Balkema, 1997.

[18] Bas Hofland. Rock & roll: Turbulence-induced damage to granular bed protections. *Communications on Hydraulic and Geotechnical Engineering*, 5, 12 2005.

[19] A.A. Kalinse. Movement of sediment as bed load in rivers. *Eos, Transactions American Geophysical Union*, 28(4):615–620, 1947. doi: 10.1029/TR028i004p00615.

[20] M. J. Kirkby. The fractal geometry of nature. benoit b. mandelbrot. w. h. freeman and co., san francisco, 1982. no. of pages: 460. price: £22.75 (hardback). *Earth Surface Processes and Landforms*, 8(4):406–406, 1983. doi: 10.1002/esp.3290080415. URL `https://onlinelibrary.wiley.com/doi/abs/10.1002/esp.3290080415`.

[21] A. N. Kolmogorov. The Local Structure of Turbulence in Incompressible Viscous Fluid for Very Large Reynolds' Numbers. In *Dokl. Akad. Nauk SSSR*, volume 30, pages 301–305, 1941.

[22] Gaurav Kumar, Saravana Kumar Lakshmanan, Harish Gopalan, and Ashoke De. Comparative study of hybrid rans-les models for separated flows. volume 1738, 09 2015. doi: 10.1063/1.4951770.

[23] S. Kundu. Prediction of velocity-dip-position at the central section of open channels using entropy theory. 2016.

[24] B.E. Launder and D.B. Spalding. The numerical computation of turbulent flows. *Computer Methods in Applied Mechanics and Engineering*, 3(2):269 – 289, 1974. ISSN 0045-7825. doi: https://doi.org/10.1016/0045-7825(74)90029-2. URL `http://www.sciencedirect.com/science/article/pii/0045782574900292`.

[25] O. Link, F. Pfleger, and U. Zanke. Characteristics of developing scour-holes at a sand-embedded cylinder. *International Journal of Sediment Research*, 23(3):258 – 266, 2008. ISSN 1001-6279. doi: https://doi.org/10.1016/S1001-6279(08)60023-2. URL `http://www.sciencedirect.com/science/article/pii/S1001627908600232`.

[26] Edward N. Lorenz. Deterministic nonperiodic flow. *Journal of the Atmospheric Sciences*, 20(2):130–141, 1963. doi: 10.1175/1520-0469(1963)020<0130:DNF>2.0.CO;2.

[27] Stephen Mclean, Jonathan Nelson, and S. Wolfe. Turbulence structure over two-dimensional bed forms: Implications for sediment transport. *Journal of Geophysical Research*, 991:12729–12748, 06 1994. doi: 10.1029/94JC00571.

[28] Florian Menter, M. Kuntz, and RB Langtry. Ten years of industrial experience with the sst turbulence model. *Heat and Mass Transfer*, 4, 01 2003.

[29] Florian R. Menter, Jochen Schütze, and Mikhail Gritskevich. Global vs. zonal approaches in hybrid rans-les turbulence modelling. In Song Fu, Werner Haase, Shia-Hui Peng, and Dieter Schwamborn, editors, *Progress in Hybrid RANS-LES Modelling*, pages 15–28, Berlin, Heidelberg, 2012. Springer Berlin Heidelberg.

[30] Charles Mockett. *A comprehensive study of detached-eddy simulation*. PhD thesis, der Technischen Universität Berlin, 01 2009.

[31] Timofey Mukha, Mattias Erik Johansson, and Mattias Liefvendahl. Effect of wall-stress model and mesh-cell topology on the predictive accuracy of les for wall-bounded flows. 2018.

[32] Robert Nichols. Turbulence models and their application to complex flows, 09 2010.

[33] Nurhan Ozturk, Azize Akcayoglu, and Besir Sahin. Flow details of a circular cylinder mounted on a flat plate. *Journal of Hydraulic Research*, May 2008:344–355, 04 2010. doi: 10.3826/jhr.2008.3126.

[34] Joongcheol Paik, Cristian Escauriaza, and Fotis Sotiropoulos. On the bimodal dynamics of the turbulent horseshoe vortex system in a wing-body junction. *Physics of Fluids - PHYS FLUIDS*, 19, 04 2007. doi: 10.1063/1.2716813.

[35] Ugo Piomelli. Large eddy simulations in 2030 and beyond. *Philosophical transactions. Series A, Mathematical, physical, and engineering sciences*, 372, 08 2014. doi: 10.1098/rsta.2013.0320.

[36] S.B. Pope and S.B. Pope. *Turbulent Flows*. Cambridge University Press, 2000. ISBN 9780521598866. URL https://books.google.nl/books?id=HZsTw9SMx-0C.

[37] Thomas Praisner and Charles Smith. The dynamics of the horseshoe vortex and associated endwall heat transfer—part i: Temporal behavior. *Journal of Turbomachinery-transactions of The Asme - J TURBOMACH-T ASME*, 128, 10 2006. doi: 10.1115/1.2185676.

[38] Tim Raaijmakers and D. Rudolph. Time-dependent scour development under combined current and waves conditions - laboratory experiments with online monitoring technique. *Proceedings of the Fourth International Conference on Scour and Erosion*, 1:152–161, 01 2008.

[39] O. Reynolds. *An Experimental Investigation of the Circumstances which Determine Whether the Motion of Water Shall be Direct Or Sinuous: And of the Law of Resistance in Parallel Channels*. Philosophical transactions. Royal Society of London, 1883. URL https://books.google.nl/books?id=zz_NHAAACAAJ.

[40] O. Reynolds. *On the Dynamical Theory of Incompressible Viscous Fluids and the Determination of the Criterion*. Philosophical transactions of the Royal Society of London. Ser. A. Harrison and Sons, 1894. URL https://books.google.nl/books?id=L5EZPAAACAAJ.

[41] W. Rodi. Comparison of les and rans calculations of the flow around bluff bodies. *Journal of Wind Engineering and Industrial Aerodynamics*, 69-71:55 – 75, 1997. ISSN 0167-6105. doi: https://doi.org/10.1016/S0167-6105(97)00147-5. URL http://www.sciencedirect.com/science/article/pii/S0167610597001475. Proceedings of the 3rd International Colloqium on Bluff Body Aerodynamics and Applications.

[42] Andreas Roulund, B. Sumer, Jorgen Fredsoe, and Jess Michelsen. Numerical and experimental investigation of flow and scour around a circular pile. *Journal of Fluid Mechanics*, 534:351 – 401, 07 2005. doi: 10.1017/S0022112005004507.

[43] P. Sagaut, S. Deck, and M. Terracol. *Multiscale and Multiresolution Approaches in Turbulence*. Imperial College Press, 2006. ISBN 9781860948978. URL https://books.google.nl/books?id=PrNgDQAAQBAJ.

[44] Besir Sahin, Nurhan Ozturk, and Cahit Gurlek. Horseshoe vortex studies in the passage of a model plate-fin-and-tube heat exchanger. *International Journal of Heat and Fluid Flow*, 29:340–351, 02 2008. doi: 10.1016/j.ijheatfluidflow.2007.06.005.

[45] A. Shields. *Anwendung der Ähnlichkeitsmechanik und der Turbulenzforschung auf die Geschiebebewegung*. Mitteilungen der Preußischen Versuchsanstalt für Wasserbau und Schiffbau, Berlin. Eigenverl. der Preußischen Versuchsanst. für Wasserbau und Schiff, 1936.

[46] Mikhail L. Shur, Philippe R. Spalart, Mikhail Kh. Strelets, and Andrey K. Travin. A hybrid rans-les approach with delayed-des and wall-modelled les capabilities. *International Journal of Heat and Fluid Flow*, 29(6):1638 – 1649, 2008. ISSN 0142-727X. doi: https://doi.org/10.1016/j.ijheatfluidflow.2008.07.001. URL http://www.sciencedirect.com/science/article/pii/S0142727X08001203.

[47] Jules Simo Tala, Serge Russeil, Daniel Bougeard, and Jean-Luc Harion. Numerical analysis of the fin spacing effect on the horseshoe vortex system evolution in a two-rows finned-tube heat exchanger. *International Journal of Numerical Methods for Heat & Fluid Flow*, 23:1136 – 1154, 09 2013. doi: 10.1108/HFF-03-2011-0059.

[48] Philippe Spalart and Steven Allmaras. A one-equation turbulence model for aerodynamic flows. *AIAA*, 439, 01 1992. doi: 10.2514/6.1992-439.

[49] Philippe Spalart, W-H Jou, Michael Strelets, and Steven Allmaras. Comments on the feasibility of les for wings, and on a hybrid rans/les approach. 01 1997.

[50] Philippe R. Spalart, Sébastien Deck, Michael L Shur, Kyle D. Squires, Michael Strelets, and Andrey Travin. A new version of detached-eddy simulation, resistant to ambiguous grid densities. 2006.

[51] Remco Steenstra, Bas Hofland, Alfons Smale, Andries Paarlberg, Huthoff Fredrik, and W. Uijttewaal. Stone stability under stationary nonuniform flows. *Journal of Hydraulic Engineering*, 142, 07 2016. doi: 10.1061/(ASCE)HY.1943-7900.0001202.

[52] Michael Strelets. Detached eddy simulation of massively separated flows. 01 2001. doi: 10.2514/6.2001-879.

[53] LEAP CFD Team. How does the reynolds number affect my cfd model? `https://www.computationalfluiddynamics.com.au/reynolds-number-cfd/`, 2013. Accessed: 2019-07-05.

[54] F.M. White. *Fluid Mechanics*. McGraw-Hill series in mechanical engineering. McGraw-Hill, 2011. ISBN 9780071311212. URL `https://books.google.nl/books?id=n43PbwAACAAJ`.

[55] David C. Wilcox. Reassessment of the scale-determining equation for advanced turbulence models. *AIAA Journal*, 26(11):1299–1310, 1988. doi: 10.2514/3.10041.

[56] Lu Zhou. *Numerical modelling of scour in steady flows*. PhD thesis, Université de Lyon, 05 2017.

A

OpenFOAM code

The input files of the most elaborate simulation case, which is the numerical model that includes both a rough bed model and a smooth cylinder, are provided.

A.1. Folder 0: Boundary conditions and initial conditions

A.1.1. U

```
/*--------------------------------*- C++ -*----------------------------------*\
| =========                 |                                                 |
| \\      /  F ield         | OpenFOAM: The Open Source CFD Toolbox           |
|  \\    /   O peration     | Version:  v1812                                 |
|   \\  /    A nd           | Web:      www.OpenFOAM.com                      |
|    \\/     M anipulation  |                                                 |
\*---------------------------------------------------------------------------*/
FoamFile
{
    version     2.0;
    format      ascii;
    class       volVectorField;
    location    "0";
    object      U;
}
// * * * * * * * * * * * * * * * * * * * * * * * * * * * * * * * * * * * * //

dimensions      [0 1 -1 0 0 0 0];


internalField   uniform (0.30 0 0);

boundaryField
{
    top
    {
        type            slip;
    }
    inlet
    {
        type            timeVaryingMappedFixedValue;
        offset          (0 0 0);
        mapMethod       nearest;
        setAverage      off;
```

```
    }
    outlet
    {
        type            inletOutlet;
        inletValue      uniform (0 0 0);
        value           uniform (0 0 0);
    }
    bot
    {
        type            noSlip;
    }
    roughBed
    {
        type            noSlip;
    }
    obstacle
    {
        type            noSlip;
    }
    sides_left
    {
        type            slip;
    }
    sides_right
    {
        type            slip;
    }
}


// ************************************************************************* //
```

A.1.2. p

```
// * * * * * * * * * * * * * * * * * * * * * * * * * * * * * * * * * * * * * * * * * * * * //

dimensions      [0 2 -2 0 0 0 0];


internalField   uniform 0;

boundaryField
{
    top
    {
        type            zeroGradient;
    }
    roughBed
    {
        type            zeroGradient;
    }
    obstacle
    {
        type            zeroGradient;
    }
    inlet
    {
```

```
        type            zeroGradient;
    }
    outlet
    {
        type            fixedValue;
        value           uniform 0;
    }
    bot
    {
        type            zeroGradient;
    }
    sides_left
    {
        type            zeroGradient;
    }
    sides_right
    {
        type            zeroGradient;
    }
}


// ************************************************************************* //
```

A.1.3. nut

```
// * * * * * * * * * * * * * * * * * * * * * * * * * * * * * * * * * * * * * //

dimensions      [0 2 -1 0 0 0 0];

internalField   uniform 0;

boundaryField
{
    bot
{
type  nutURoughWallFunction;
roughnessHeight 0;
roughnessConstant 0;
roughnessFactor 1;
value  uniform 0;
}
    top
    {
        type            zeroGradient;
    }
    sides_left
    {
        type            zeroGradient;
    }
    sides_right
    {
        type            zeroGradient;
    }
    roughBed
    {
type  nutURoughWallFunction;
```

```
roughnessHeight 0.01;
roughnessConstant 0.5;
roughnessFactor 1;
value  uniform 0;
    }
    obstacle
    {
type  nutURoughWallFunction;
roughnessHeight 0;
roughnessConstant 0;
roughnessFactor 1;
value  uniform 0;
    }
    inlet
    {
        type            calculated;
        value           uniform 0;
    }
    outlet
    {
        type            calculated;
        value           uniform 0;
    }
}


// ************************************************************************* //
```

A.1.4. nuTilda

```
// * * * * * * * * * * * * * * * * * * * * * * * * * * * * * * * * * * * * * * * * * * * * //

dimensions      [0 2 -1 0 0 0 0];


internalField   uniform 0;

boundaryField
{
    bot
    {
        type            fixedValue;
        value           uniform 0;
    }
    roughBed
    {
        type            fixedValue;
        value           uniform 0;
    }
    obstacle
    {
        type            fixedValue;
        value           uniform 0;
    }
    top
    {
        type            zeroGradient;
```

```
    }
    sides_right
    {
        type            zeroGradient;
    }
    sides_left
    {
        type            zeroGradient;
    }
    inlet
    {
        type            timeVaryingMappedFixedValue;
        offset          0;
        setAverage      off;
        mapMethod       nearest;
//        type            fixedValue;
        value           $internalField;
    }
    outlet
    {
        type            zeroGradient;
    }
}


// ************************************************************************* //
```

A.2. Folder constant: Flow conditions

A.2.1. transportProperties

```
// * * * * * * * * * * * * * * * * * * * * * * * * * * * * * * * * * * * * * //

Ubar            [0 1 -1 0 0 0 0] (0.3 0 0);

transportModel  Newtonian;

nu              [0 2 -1 0 0 0 0] 1.31e-06;

// ************************************************************************* //
```

A.2.2. turbulenceProperties

```
// * * * * * * * * * * * * * * * * * * * * * * * * * * * * * * * * * * * * * //

simulationType  LES;

LES
{
LESModel       SpalartAllmarasIDDES;

printCoeffs     on;
turbulence          on;

delta IDDESDelta; // maxDeltaxyz;//


maxDeltaxyzCoeffs
```

```
{
    deltaCoeff 2;
}



SpalartAllmarasIDDESCoeffs
{
    fieldMaps
    {
        nuTilda         nuTilda;
        nuSgs           nuSgs;
    }
    alphaNut        1.5;
    Cb1             0.1355;
    Cb2             0.622;
    Cw2             0.3;
    Cw3             2;
    Cv1             7.1;
    Cv2             5;
    CDES            0.65;
    ck              0.07;
    fwStar          0.424;
    cl              3.55;
    ct              1.63;
}

IDDESDeltaCoeffs
{
    cw 0.15;
    deltaCoeff      1;//1; 2 for hexMesh

}

SpalartAllmarasCoeffs
{
    alphaNut         1.5;
    Cb1              0.1355;
    Cb2              0.622;
    Cw2              0.3;
    Cw3              2;
    Cv1              7.1;
    Cv2              5.0;
    CDES             0.65;
    ck               0.07;
}

SpalartAllmarasDDESCoeffs
{
    alphaNut         1.5;
    Cb1              0.1355;
    Cb2              0.622;
    Cw2              0.3;
    Cw3              2.0;
    Cv1              7.1;
    Cv2              5.0;
```

```
    CDES            0.65;
    ck              0.07;
}

SpalartAllmarasIDDESCoeffs
{
    alphaNut        1.5;
    kappa           0.4187;
    Cb1             0.1355;
    Cb2             0.622;
    Cw2             0.3;
    Cw3             2.0;
    Cv1             7.1;
    Cv2             5.0;
    CDES            0.65;
    ck              0.07;
}



PrandtlCoeffs
{
    delta           cubeRootVol;
    cubeRootVolCoeffs
    {
        deltaCoeff      1;
    }

    smoothCoeffs
    {
        delta           cubeRootVol;
        cubeRootVolCoeffs
        {
            deltaCoeff      1;
        }

        maxDeltaRatio   1.1;
    }

    Cdelta          0.158;
}




vanDriestCoeffs
{
    delta           cubeRootVol;
    cubeRootVolCoeffs
    {
        deltaCoeff      1;
    }

    smoothCoeffs
    {
        delta           cubeRootVol;
```

```
        cubeRootVolCoeffs
        {
            deltaCoeff      1;
        }

        maxDeltaRatio   1.1;
    }

    Aplus           26;
    Cdelta          0.158;
}


smoothCoeffs
{
    delta           cubeRootVol;
    cubeRootVolCoeffs
    {
        deltaCoeff      1;
    }

    maxDeltaRatio   1.1;
}
}


// ************************************************************************* //
```

A.3. Folder system: Simulation conditions

A.3.1. controlDict

```
// * * * * * * * * * * * * * * * * * * * * * * * * * * * * * * * * * * * * * * * * * //

application     pimpleFoam;

startFrom       latestTime;

//startTime       0;

stopAt          endTime;

endTime         500;   //!

deltaT          0.0025;

writeControl    timeStep;

writeInterval   10000;  //20000; every 50s blepw to output

purgeWrite      30; //!

writeFormat     ascii;

writePrecision  7;

writeCompression on;
```

```
timeFormat      general;

timePrecision   7;

runTimeModifiable true;



//Adding forces in the computation
libs
(
"libutilityFunctionObjects.so" //Library A
"libsampling.so" //Library B
);

functions
{

#include "forceCoeffs" //Cd and Cf around cylinder
#include "pressureCoeffs"


turbulenceFields1
    {
        type        turbulenceFields;
        libs ("libfieldFunctionObjects.so");
writeControl    writeTime;
        fields
        (
            R
            k
        );

    }

//#includeFunc pressureDifferencePatch




residuals //Name of the file and the folder in case/postProcessing/
{
type  residuals; //Name of the function which you want from the library A
enabled true; //Do you want to write? yes or no
writeControl timeStep; //What should control the write feature?
writeInterval 1000; //100; This is the relative write (time) step
//Lets say you have dt = 0.0005, then writeInterval will be 1*0.0005
fields
(
p
U
nut
nuTilda
);
```

```
}

Q1
    {
        type            Q;
        libs            ("libfieldFunctionObjects.so");
        writeControl    timeStep;
writeInterval 10000; //20000 all
    }
    DESField
    {
        type            DESModelRegions;
        libs            ("libfieldFunctionObjects.so");
        //region "region0";
        writeControl    timeStep;
writeInterval 10000; //500
    }
    vorticity1
    {
        type            vorticity;
        libs            ("libfieldFunctionObjects.so");
        writeControl    timeStep;
writeInterval 10000; //500
    }
    yPlus
    {
        type            yPlus;
        libs            ("libfieldFunctionObjects.so");
        writeControl    timeStep;
writeInterval 10000; //500
    }

 shearStress
    {
        libs ("libfieldFunctionObjects.so");
        type            wallShearStress;
        writeControl    timeStep;
writeInterval 10000; //500
     }

fieldAverage1
    {
        type            fieldAverage;
        libs ("libfieldFunctionObjects.so");
        enabled         true;
        writeControl    writeTime;
timeStart       50;
        fields
        (
            U
            {
                mean        on;
                prime2Mean  on;
                base        time;
            }
```

```
            p
            {
                mean        on;
                prime2Mean  on;
                base        time;
            }
wallShearStress
            {
                mean        on;
                prime2Mean  on;
                base        time;
            }
yPlus
            {
                mean        on;
                prime2Mean  on;
                base        time;
            }
k
            {
                mean        on;
                prime2Mean  on;
                base        time;
            }
epsilon
            {
                mean        on;
                prime2Mean  on;
                base        time;
            }
        );
    }

};

functions
{
//#include "cuttingPlane"
#include "sampleDict_fields"
#include "sampleDict_mean"
#include "sampleBedSurfaceDict" // values surface Bed
#include "sampleChannelSurfaceDict" // values surface Channel
}

// * * * * * * * * * * * * * * * * * * * * * * * * * * * * * * * * * * * * * * * * * * * * //
```

A.3.2. createPatchDict

```
// * * * * * * * * * * * * * * * * * * * * * * * * * * * * * * * * * * * * * * * * * * * * //

// This application/dictionary controls:
// - optional: create new patches from boundary faces (either given as
//   a set of patches or as a faceSet)
// - always: order faces on coupled patches such that they are opposite. This
//   is done for all coupled faces, not just for any patches created.
// - optional: synchronise points on coupled patches.
// - always: remove zero-sized (non-coupled) patches (that were not added)
```

```
// 1. Create cyclic:
// - specify where the faces should come from
// - specify the type of cyclic. If a rotational specify the rotationAxis
//   and centre to make matching easier
// - always create both halves in one invocation with correct 'neighbourPatch'
//   setting.
// - optionally pointSync true to guarantee points to line up.

// 2. Correct incorrect cyclic:
// This will usually fail upon loading:
//  "face 0 area does not match neighbour 2 by 0.0100005%"
//  " -- possible face ordering problem."
// - in polyMesh/boundary file:
//      - loosen matchTolerance of all cyclics to get case to load
//      - or change patch type from 'cyclic' to 'patch'
//        and regenerate cyclic as above

// Do a synchronisation of coupled points after creation of any patches.
// Note: this does not work with points that are on multiple coupled patches
//       with transformations (i.e. cyclics).
pointSync false;

// Patches to create.
patches
(
    {
        // Name of new patch
        name inlet_cyc;

        // Dictionary to construct new patch from
        patchInfo
        {
            type cyclic;
            neighbourPatch outlet_cyc;

            // Optional: explicitly set transformation tensor.
            // Used when matching and synchronising points.
            //transform rotational;
            //rotationAxis (1 0 0);
            //rotationCentre (0 0 0);
            // transform translational;
            // separationVector (1 0 0);

            // Optional non-default tolerance to be able to define cyclics
            // on bad meshes
            //matchTolerance 1E-2;
        }

        // How to construct: either from 'patches' or 'set'
        constructFrom patches;

        // If constructFrom = patches : names of patches. Wildcards allowed.
        patches (inlet);

        // If constructFrom = set : name of faceSet
```

```
        //set f0;
    }
    {
        // Name of new patch
        name outlet_cyc;

        // Dictionary to construct new patch from
        patchInfo
        {
            type cyclic;
            neighbourPatch inlet_cyc;

            // Optional: explicitly set transformation tensor.
            // Used when matching and synchronising points.
            //transform rotational;
            //rotationAxis (1 0 0);
            //rotationCentre (0 0 0);
            // transform translational;
            // separationVector (1 0 0);
        }

        // How to construct: either from 'patches' or 'set'
        constructFrom patches;

        // If constructFrom = patches : names of patches. Wildcards allowed.
        patches (outlet);

        // If constructFrom = set : name of faceSet
        //set f0;
    }

);

// ************************************************************************* //
```

A.3.3. decomposeParDict

```
// * * * * * * * * * * * * * * * * * * * * * * * * * * * * * * * * * * * * * * * * //

numberOfSubdomains  8;

method          manual; //scotch/manual

scotchCoeffs
{
}

manualCoeffs
{
    dataFile    "cellDist";
}

// ************************************************************************* //
```

A.3.4. forceCoeffs

```
forceCoeffs
{
```

```
    type            forceCoeffs;
    libs            ("libforces.so");
    writeControl    timeStep;
    writeInterval   40; //dt=0.0025 X/dt //40000

    patches         (obstacle);
    rho             rhoInf;      // Indicates incompressible
    log             true;
    rhoInf          1.225;       // Redundant for incompressible
pName p;
uName U;
    liftDir         (0 0 1);
    dragDir         (1 0 0);
    CofR            (1.580 0 .5);  // Axle midpoint on ground
    pitchAxis       (0 1 0);
    magUInf         0.325; // maximum velocity obtained from precursor
    lRef            0.158;        // Wheelbase (of reference) length (https://www.cfd-online.com/
    Aref            0.0948;        // Frontal area estimated as 0.158 (D) * 0.6 (height)
}


// ************************************************************************* //
```

A.3.5. fvSchemes

```
// * * * * * * * * * * * * * * * * * * * * * * * * * * * * * * * * * * * * * * * * * * * * //

ddtSchemes
{
    default         backward;
}

gradSchemes
{
    default         Gauss linear;
}

divSchemes
{
    default         none;
    div(phi,U)      Gauss LUST grad(U);
    div(phi,k)      Gauss limitedLinear 1;
    div(phi,B)      Gauss limitedLinear 1;
    div(phi,nuTilda) Gauss limitedLinear 1;
    div(B)          Gauss linear;
    div((nuEff*dev2(T(grad(U))))) Gauss linear;
}

laplacianSchemes
{
    default         Gauss linear corrected;
}

interpolationSchemes
{
    default         linear;
}
```

```
snGradSchemes
{
    default         corrected;
}

wallDist
{
    method meshWave;
}

fluxRequired
{
    default         no;
    p               ;
}

// ************************************************************************* //
```

A.3.6. fvSolution

```
// * * * * * * * * * * * * * * * * * * * * * * * * * * * * * * * * * * * * * * * * * * * * //


solvers
{
    p
    {
        solver          GAMG; //generalised geometric-algebraic multi-grid
        tolerance       1e-6; //f the case is specified to solve pressure 4 times within one time step,
        relTol          0; // limits the relative improvement from initial to final solution. In transi
        smoother   DIC;
        nPreSweeps      0; //number of sweeps as the algorithm is coarsening (default 0).
        nPostSweeps     2; //number of sweeps as the algorithm is refining (default 2).
        cacheAgglomeration true; // switch specifying caching of the agglomeration strategy (default tr
        nCellsInCoarsestLevel 10; //approximate mesh size at the most coarse level in terms of the numb
        agglomerator    faceAreaPair;
        mergeLevels     1; // keyword controls the speed at which coarsening or refinement is performed
    }

pFinal
    {
        $p;
        smoother        DIC;
        tolerance       1e-8;
        relTol          0;
    }

    "(U|k)"
    {
        solver          PBiCG;
        preconditioner  DILU;
        tolerance       1e-06;
        relTol          0;
    }

"(U|k|nuTilda)Final"
```

```
    {
        $U;
        tolerance       1e-08;
        relTol          0;
    }
}



PIMPLE
{
    nOuterCorrectors 1; //nOuterCorrectors determines no. of iterations over the non-linear coupl
   // >1, then pimple
nCorrectors     3; //nCorrectors is the number of times a solution for pressure is attempted with
    nNonOrthogonalCorrectors 1;
momentumPredictor yes;
    //pRefCell        1001;
pRefPoint (0 0.375 0.25);
    pRefValue       0;
//turbOnFinalIterOnly  false;
}


// ************************************************************************* //
```

A.3.7. mapFieldsDict

```
// * * * * * * * * * * * * * * * * * * * * * * * * * * * * * * * * * * * * * * * * * * * * //

// List of pairs of source/target patches for mapping
patchMap
(
);

// List of target patches cutting the source domain (these need to be
// handled specially e.g. interpolated from internal values)
cuttingPatches
(
obstacle
roughBed
);

// ************************************************************************* //
```

A.3.8. pressureCoeffs

```
pressureCoeff
{
         type  pressure;
         functionObjectLibs ("libfieldFunctionObjects.so");
         source wall;
         sourceName obstacle;
//         patch      ("obstacle")
         log yes;

    writeControl    timeStep;
    writeInterval   10000; //dt=0.0025 X/dt //40000
```

```
        enabled yes;
        calcTotal no;
        calcCoeff yes;
        pRef 0;
        rhoInf 999.6; //https://www.engineeringtoolbox.com/water-density-specific-weight-d_595.html
        pInf 0;
        UInf (0.325 0 0); //maximum value of precursor
}

// ************************************************************************* //
```

A.3.9. sampleBedSurfaceDict

```
obstacle_surface {

type surfaces;
libs            ("libsampling.so");

interpolationScheme cellPoint; //cellPoint
    writeControl    timeStep;
    writeInterval   40; //40;10 Hz with 0.0025 dt

surfaceFormat       raw;

    fields ( p U wallShearStress static(p)_coeff ); //turbulenceProperties:R

surfaces
(
    Bed_data
    {
        type            patch;
        patches         (roughBed);
interpolate  true;
triangulate false;
    }
);

}



// ************************************************************************* //
```

A.3.10. sampleChannelSurfaceDict

```
// * * * * * * * * * * * * * * * * * * * * * * * * * * * * * * * * * * * * * * * * * //

channel_surface {

type surfaces;
libs            ("libsampling.so");

interpolationScheme cellPoint; //cellPoint
    writeControl    timeStep;
    writeInterval   40; //40;10 Hz with 0.0025 dt

surfaceFormat       raw;
```

```
    fields ( p U wallShearStress ); //turbulenceProperties:R

surfaces
(
    ChannelBed_data
    {
        type            patch;
        patches         (bot);
interpolate  true;
triangulate false;
    }
);

}



// ************************************************************************* //
```

A.3.11. sampleDictFields

```
cuttingplane {

type surfaces;
libs            ("libsampling.so");

interpolationScheme cellPoint; //cellPoint
    writeControl    timeStep;
    writeInterval   40; //10 Hz with 0.0025 dt

surfaceFormat       raw;

    fields ( U turbulenceProperties:R ); //turbulenceProperties:R

    surfaces
   (
plane30x30
    {
        type    plane;
        source  cells;
triangulate false;
        planeType   pointAndNormal;

        pointAndNormalDict
       {
            normal (0 0 1);
            point  (1.3 .1 .5);
       }
           bounds (1.201 0 .49) (1.501 0.3 .51);
    }
    );

}
```

A.3.12. sampleDictMean

```
cuttingplane_mean {
```

```
type surfaces;
libs            ("libsampling.so");

interpolationScheme cellPoint; //cellPoint
    writeControl    timeStep;
    writeInterval   40000; //X = wanted timestep (100) dt = 0.0025, X/dt = interval

surfaceFormat       raw;

    fields ( UMean );

    surfaces
   (
plane30x30
    {
        type    plane;
        source  cells;
triangulate false;
        planeType   pointAndNormal;

        pointAndNormalDict
       {
            normal (0 0 1);
            point  (1.3 .1 .5);
       }
           bounds (1.201 0 .49) (1.501 0.3 .51);
    }
    );

}
```

A.3.13. setFieldsDict

```
// * * * * * * * * * * * * * * * * * * * * * * * * * * * * * * * * * * * * * * * * * * * * //

x1  0.75;
y1  0.33;
z1  0.35;
z2  0.65;

x2  #calc "6 - $x1";

defaultFieldValues ( volScalarFieldValue cellDist 0 ); //field 1

regions
(
      boxToCell
      {
           box ( $x1 0 0 ) ( $x2  $y1  $z1  ) ;
           fieldValues ( volScalarFieldValue cellDist 1); //field 3
      }
      boxToCell
      {
           box ( $x1 0 $z1   ) (  $x2  $y1  $z2  ) ;
           fieldValues ( volScalarFieldValue cellDist 2); //field 4
```

```
      }
      boxToCell
      {
           box (  $x1 0 $z2  ) (  $x2  $y1  1   ) ;
           fieldValues ( volScalarFieldValue cellDist 3); //field 5
      }
      boxToCell
      {
           box ( $x1 $y1 0) (  $x2  0.6  $z1 ) ;
           fieldValues ( volScalarFieldValue cellDist 4); //field 6
      }
      boxToCell
      {
           box ( $x1 $y1 $z1 ) ( $x2  0.6  $z2  ) ;
           fieldValues ( volScalarFieldValue cellDist 5); //field 7
      }
      boxToCell
      {
           box (  $x1 $y1 $z2 ) ( $x2 0.6 1) ;
           fieldValues ( volScalarFieldValue cellDist 6); //field 8
      }
      boxToCell
      {
           box (  $x2 0 0 ) ( 6 0.6 1 ) ;
           fieldValues ( volScalarFieldValue cellDist 7); //field 2
      }
);


// ************************************************************************* //
```

A.3.14. snappyHexMeshDict

```
// * * * * * * * * * * * * * * * * * * * * * * * * * * * * * * * * * * * * * * * * * * * * //

// Which of the steps to run
castellatedMesh true;    // make basic mesh ?
snap            true;    // decide to snap back to surface ?
addLayers       false;   // decide to add viscous layers ?


geometry // Load in STL files here
{
roughBed.stl {type triSurfaceMesh; name roughBed;}
// refinementBox {type searchableBox; min (1 0 0 ); max ( 2 0.6 1);}
};

castellatedMeshControls
{
    maxLocalCells 1000000;  //max cells per CPU core
    maxGlobalCells 2000000; //max cells to use before mesh deletion step
    minRefinementCells 4;  //was 0 - zero means no bad cells are allowed during refinement stages
    maxLoadUnbalance 0.10;
    nCellsBetweenLevels 20;  // expansion factor between each high & low refinement zone, INCREAS

    // Explicit feature edge refinement
    // ~~~~~~~~~~~~~~~~~~~~~~~~~~~~~~~
```

```
    features // taken from STL from each .eMesh file created by "SurfaceFeatureExtract" command
    (
        {file "roughBed.eMesh"; level 0;}
    );

    // Surface based refinement
    // ~~~~~~~~~~~~~~~~~~~~~~~~

    refinementSurfaces // Surface-wise min and max refinement level
    {
roughBed{level (0 0);} // was 4 4
    }


    resolveFeatureAngle 80;  // Resolve sharp angles // Default 30
    refinementRegions        // In descending levels of fine-ness
    {volume {mode distance; levels ((0 0));}} // was ((1 1) (2 0)))
    locationInMesh (0.05 0.05 0.05);  //to decide which side of mesh to keep **
    allowFreeStandingZoneFaces true;
}


// Settings for the snapping.
snapControls
{
    nSmoothPatch 3;
    tolerance 4.0;
    nSolveIter 30;
    nRelaxIter 5;
    nFeatureSnapIter 15; // default is 10

// New settings from openfoam 2.2 onwards for SHMesh

implicitFeatureSnap false; // default is false - detects without doing surfaceFeatureExtract
explicitFeatureSnap true; // default is true
multiRegionFeatureSnap false; // deafault is false - detects features between multiple surfaces

}



// Settings for the layer addition.
addLayersControls //add the PATCH names from inside the STL file so STLpatchName_insideSTLName
{
    relativeSizes false; // was true
    layers
    {
roughBed
          {nSurfaceLayers 5;} // was 3
    }

    expansionRatio 1.3;
    finalLayerThickness 0.05; //was 0.00016
    minThickness 0.01; //was 0.00008
    nGrow 0; // was 1
```

```
    // Advanced settings

    featureAngle 80; // was 70 //- When not to extrude surface. 0 is flat, 90 is right angle.
    nRelaxIter 3;  //- Max# of snapping relaxation iter. Should stop before upon reaching a corre
    nSmoothSurfaceNormals 1;  // Number of smoothing iterations of surface normals
    nSmoothNormals 3; // Number of smoothing iterations of interior mesh movement direction
    nSmoothThickness 10;  // Smooth layer thickness over surface patches
    maxFaceThicknessRatio 0.5; // Stop layer growth on highly warped cells
    maxThicknessToMedialRatio 0.3; // Reduce layer growth where ratio thickness to medial distanc
    minMedianAxisAngle 130;  // Angle used to pick up medial axis points
    nBufferCellsNoExtrude 0;   // Create buffer region for new layer terminations
    nLayerIter 50; // Overall max number of layer addition iterations
}



// Generic mesh quality settings. At any undoable phase these determine
// where to undo.
meshQualityControls
{
    maxNonOrtho 65;
    maxBoundarySkewness 20;
    maxInternalSkewness 4;
    maxConcave 80;
    minFlatness 0.5;
    minVol 1e-13;
    minTetQuality 1e-9;
    minArea -1;
    minTwist 0.02;
    minDeterminant 0.001;
    minFaceWeight 0.02;
    minVolRatio 0.01;
    minTriangleTwist -1;

    // Advanced

    nSmoothScale 4;
    errorReduction 0.75;
}

// Advanced

debug 0;


// Merge tolerance. Is fraction of overall bounding box of initial mesh.
// Note: the write tolerance needs to be higher than this.
mergeTolerance 1E-6;


// ************************************************************************* //
```

A.3.15. surfaceFeatureExtractDict

```
// * * * * * * * * * * * * * * * * * * * * * * * * * * * * * * * * * * * * * * * * * //
```

```
roughBed.stl
{
    extractionMethod    extractFromSurface; // extractFromFile or extractFromSurface
    extractFromSurfaceCoeffs
    {includedAngle   150;}
    writeObj                yes;    // Write options
}

// ************************************************************************* //
```